CArbon-14 Source Term

CAST

WP5 Report – Year 4 (D5.18)

D5.18 Report on ^{13}C behaviour under ion irradiation in HOPG (model graphite)

Authors:

Nelly Toulhoat and N. Moncoffre

Editor: Simon Norris

Date of issue of this report: July 12th 2017

CAST
Report on ^{13}C behaviour under ion irradiation in HOPG
(model graphite) (D5.18)

Abstract

The aim of work undertaken by IPNL is to simulate the behaviour of ^{14}C during reactor operation and evaluate the independent or synergistic effects of temperature and irradiation on ^{14}C behaviour. Indeed, the knowledge of the location and speciation of ^{14}C in irradiated graphite at reactor shutdown is mandatory to understand and foresee its behaviour during dismantling, to optimize an eventual decontamination process and to evaluate its migration behaviour during disposal. ^{14}C is mainly formed through the activation of ^{13}C but a certain amount may also be generated through the activation of ^{14}N. In this study, ^{13}C implanted into model HOPG graphite is mainly used to simulate the behaviour of ^{14}C, displaced from its original structural site through recoil, in coke grains which build around 80% of nuclear graphite. ^{13}C was implanted at different fluences. This allows inducing a high or a low disorder into the graphite matrix which is representative of the multiplicity of the structure states already present in nuclear graphite. It also allows simulating structural differences resulting from early neutron irradiation in high or low flux regions of the reactor. Then, the samples were ion irradiated to simulate neutron irradiation.

The collision of the impinging neutrons with the graphite matrix carbon atoms induces mainly ballistic damage. However, a part of the recoil carbon atom energy is also transferred to the graphite lattice through electronic excitation. Therefore we simulated the effects of the different irradiation regimes coupled with temperature using ion irradiation by varying the Sn(nuclear)/Se(electronic) stopping power ratio. Thus, the samples were irradiated with different ions of different energies at various facilities using dedicated irradiation cells. The structural modifications were followed by Raman microspectrometry and High Resolution Transmission Electron Microscopy (HRTEM).

The results show that temperature generally counteracts the disordering effects of irradiation but the achieved reordering level strongly depends on the initial structural state of the graphite matrix. Ion irradiation in both ballistic and electronic regimes disorders the graphite structure and promotes the formation of sp^3 bonds. On the contrary, temperature has reordering effects in both regimes, resulting into the formation of new sp^2 structures. The results also show that graphite structure modifications are mainly due to the ballistic impact. When the structure is already strongly disordered, ballistic irradiation and temperature have a synergistic reordering action due to temperature enhanced mobility of the pre-existing and irradiation induced vacancies and interstitials. When the electronic excitation values are "low", as in the case of UNGG or Magnox reactors, they have low impact on graphite structure evolution.

Thus, extrapolating to reactor conditions, for an initially highly disordered structure, irradiation at reactor temperatures (200 – 500°C) should induce almost no change of the initial structure. On the contrary, when the structure is initially less disordered, there should be a "zoning" of the reordering: Depending on the graphite temperatures, i) in "cold" high flux irradiated zones where the ballistic damage is important, the structure should be poorly reordered; ii) in "hot" low flux irradiated zones where the ballistic impact is lower and can therefore be counteracted by temperature, a better reordering of the structure should be achieved. Whatever the irradiation regime and even for temperatures as high as 1000°C, we have shown that the implanted ^{13}C is not released from the graphite matrix. It stabilizes into sp^3 or sp^2 structures, whose relative proportions depend on the irradiation regime and temperature. Thus, extrapolating to ^{14}C, except when located close to open pores where it can be removed through radiolytic corrosion, it should stabilize in the graphite matrix into sp^2 or sp^3 structures with variable proportions depending on the irradiation conditions.

Introduction

The parameters governing the behaviour of radionuclides in an UNGG (Natural Uranium Graphite *Gas*-cooled) reactor are the temperature, which can reach 500 °C, neutron irradiation and radiolytic corrosion. The objective of this work is to study the irradiation effects on graphite, with and without the effect of temperature, on the mobility of implanted ^{13}C (used to simulate ^{14}C) as well as the evolution of the graphite structure. It is mainly based on the results of the PhD thesis of N. Galy [Galy 2016] and Galy et al. [Galy 2017]. The effect of temperature alone and that of radiolytic corrosion concerning the behaviour of ^{13}C and ^{37}Cl implanted in the nuclear graphite were investigated during previous studies carried out at IPNL [Vaudey 2009], [Vaudey 2010 a and b], [Vaudey 2011], [Silbermann 2013], [Blondel 2013], [Silbermann 2014], [Blondel 2014], [Toulhoat 2015], [Moncoffre 2016]. In our study, we have chosen to study an HOPG (highly-ordered pyrolytic graphite) model enabling the simulation of coke grains which are the major part of nuclear graphite.

Samples used during this work were HOPG platelets Grade SPI-1 with a density close to 2.26 g.cm^{-3}, obtained from SPI Supplies (West Chester, US) through Neyco SA (Paris, France). HOPG is synthetic graphite obtained through the pyrolysis of pyrocarbon with a final step at 3400–3600 °C under 1 MPa pressure. This technique aims at reducing the mosaic spread, i.e. the mean angle between superimposed crystallites, below 0.4°. It results in an almost parallel orientation of the c axis of the crystallites (normal to the graphene layers) and a very large crystallite diameter (up to about 1 µm). However, from a crystallographic point of view, since a and b axes of the superimposed crystallites can be randomly rotated around the common c axis (turbostratic stacking), HOPG is not strictly speaking a single crystal. Nevertheless, its highly crystalline order combined with the absence of porosity leads to a density similar to the theoretical graphite one (2.26 g cm.$^{-3}$). We received the HOPG samples as 10 x10 mm^2 plates, 1 mm thick and coated with a protective film on one side. Once their protective was film removed, they were annealed at in vacuum (~10^{-7} mbar) at 1000° for 10 h in order to desorb most of the gaseous impurities present in the material and also to anneal (at least partially) the defects possibly induced by removing the protection film.

We have studied the irradiation and temperature effects on the migration of ^{13}C and the evolution of the HOPG structure. In certain cases, we did experiments which were similar to conditions in UNGG reactors in a configuration enabling the evolution of the structure to be followed by *in situ* Raman microspectrometry.

With the above objectives in mind, we wanted to simulate the different structural states of irradiated graphite. Therefore, in order to reproduce a very disordered state, we implanted ^{13}C at a fluence of 6 x 10^{16} at.cm^{-2} leading to 7.4 dpa (displacements per atom or atoms displaced) at the maximum projected range of defects R_d in the implanted zone. On the other hand, to simulate only slightly disordered states, we implanted ^{13}C at 4 x 10^{14} at.cm^{-2} or ^{37}Cl at 5 x 10^{13} at.cm^{-2} leading to less than 0.1 dpa at the maximum projected range R_d.

The mobility of the species in the implanted graphite and the evolution of the structural state of the graphite under different irradiation regimes (ballistic and electronic) will be studied. After describing the experimental conditions and the irradiation used in order to study the effects of irradiation, we will give the results 13C detail and interpret them.

1 | Description of the irradiation experimental protocol

1.1 | Choice of irradiation conditions

During neutron irradiation, the neutrons interact with the matter both by collision with the atom nuclei (i.e. ballistic damage) and by nuclear reactions. The first atoms hit by neutrons are caused to move, thus starting a cascade of atomic collisions leading to electronic excitation as they go through the matter and on the path of the atoms they displace (recoil atoms). The ballistic damage can be evaluated using the nuclear stopping power and can be denoted by the number of displacements per atom (dpa). The effect of electronic excitation can be quantified using the electronic stopping power.

The experimental simulation of neutron irradiation in a reactor is done by irradiation of the graphite samples with different ions of different energy. The choice of the latter enables the study of the effects with or without electron excitation or ballistic damage.

It is possible to cover a wide range of the electronic and nuclear stopping powers by working with different particle accelerators. For example, we used the 4 MV Van de Graaff accelerator belonging to the IPNL, the 15 MV Tandem in the IPN in Orsay, and the Cyclotron of the CEMHTI in Orléans. From the beams available on the Van de Graaff (proton, deuteron, helium, carbon and argon), we chose to use the carbon and argon ones because, within the energy range of the accelerator, these ions would allow us to preferentially simulate ballistic damage. In the Tandem in Orsay, we used high energy sulphur and iodine beams with the objective of preferentially simulating the electronic excitation effects. Finally, we worked on the cyclotron in Orléans with helium ions (with a higher energy than that produced at the IPNL) in order to realise irradiation in the conditions closest to those in a reactor.

By simulation using the SRIM-2013 software [Ziegler 1985, Ziegler 2010], the nature and energy of the ions were selected. These calculations were done for graphite with a density of 2.2 g/cm^3, very close to that of the HOPG which is highly-crystalline and non-porous. For each ion chosen for irradiation, we drew the curve of the evolution of the electronic stopping power (S$_e$ or $(\frac{dE}{dx})_{elec}$), nuclear stopping power (S$_n$ or $(\frac{dE}{dx})_{nuc}$) and the number of dpa as a function of depth into the material.

In the next section, we will discuss irradiation in an electronic regime which enables the effect of electronic excitation to be favoured, and in the ballistic regime which allows the effect of ballistic damage to be favoured. Furthermore, in the literature, certain authors consider that matter is irradiated in a ballistic regime when the energy per atomic mass unit of the incident ion is in the order of a few tens of keV/u and in an electronic regime when it is greater than 1 MeV/u [Thomé 2010]. The energy per atomic mass unit is given in Table 1 for the ions we have chosen.

Table 1: *Table summarising the choice of ion and energy for the two irradiation regimes*

Atom used	Atomic mass unit (u)	Irradiation energy (keV)	Energy per atomic mass unit (keV/u)	Irradiation regime
C	12	400	33	Ballistic
		600	50	
Ar	**40**	**800**	**20**	
He	**4**	**15 700**	**3 925**	Electronic
S	32	100 000	3 125	
I	127	200 000	1 575	

In table 1 in red, we indicate the most favourable irradiation for the ballistic regime, and in green the most favourable for the electronic regime according to the energy per atomic mass unit. Note that initially, carbon ion irradiation was done at an energy of 600 keV with the 4 MV Van de Graaff accelerator of the IPNL; however, sometimes we irradiated using the IMIO 400 implanter in the IPNL. The latter cannot reach 600 keV which explains why an energy of 400 keV is also given.

Figure 1 shows the parameters previously discussed (S_e, S_n and the number of dpa) as a function of depth, calculated in a graphite with a density of 2.2 g/cm^3 using the SRIM 2013 software [Ziegler 1985, Ziegler 2010] for each irradiation condition chosen. The calculation of the number of dpa takes into consideration the fluence used for each irradiation.
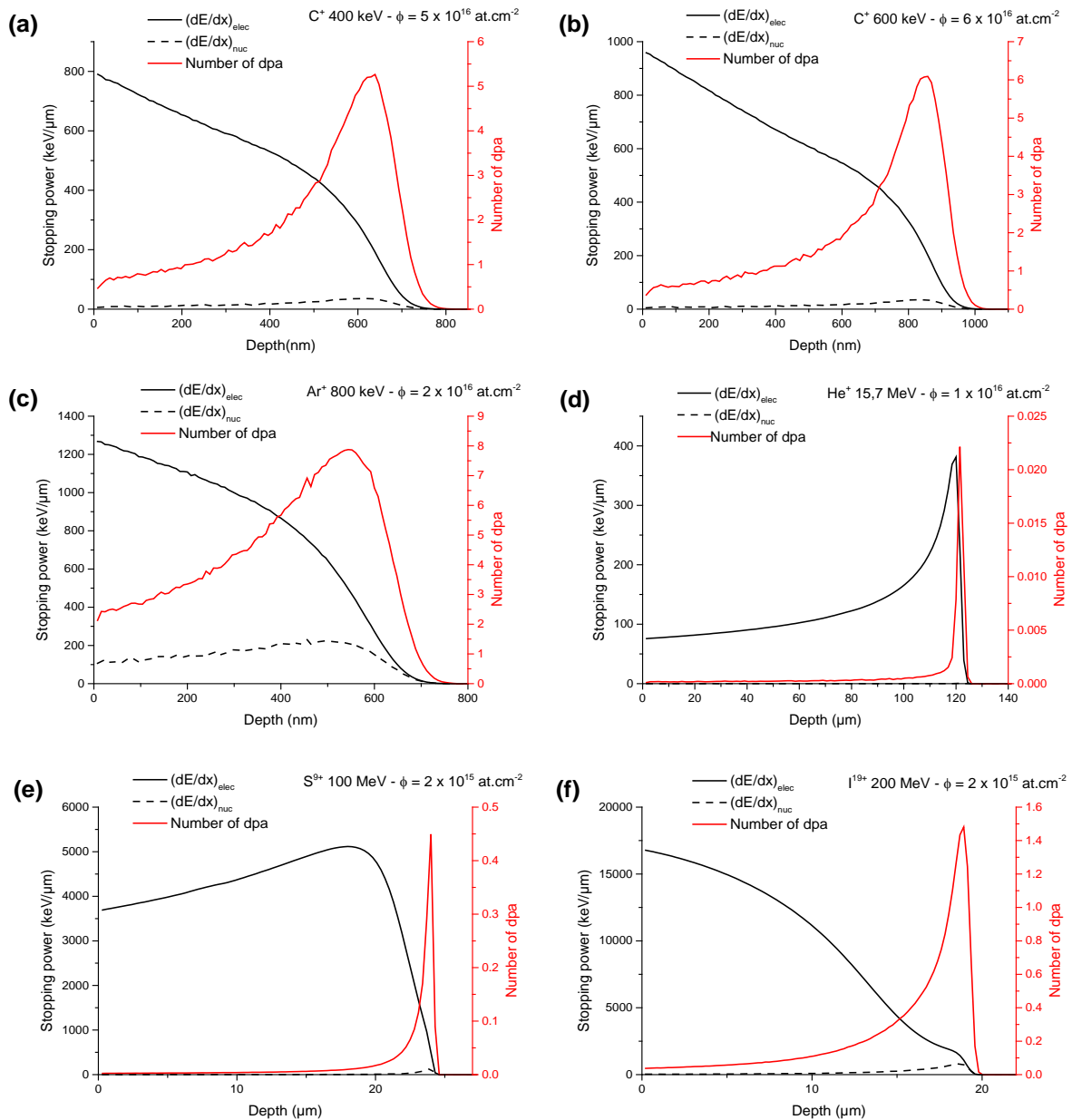
Figure 1: *Results of the calculations of S_e, S_n and the number of dpa realised using the SRIM-2013 software presented as a function of depth for each irradiation condition (a) C$^+$ at 400 keV and 5 x 10^{16} ions.cm^{-2} (b) C$^+$ at 600 keV and 6 x 10^{16} ions.cm^{-2} (c) Ar$^+$ at 800 keV and 2 x 10^{16} ions.cm^{-2} (d) He$^+$ at 15.7 MeV and 1 x 10^{16} ions.cm^{-2} (e) S^{9+} at 100 MeV and 2 x 10^{15} ions.cm^{-2} and (f) I^{19+} at 200 MeV and 2 x 10^{15} ions.cm^{-2}*

It is important to point out that none of these graphs are on the same scale. In addition, the depth is in nanometres for irradiation at low energy (ballistic regime) and in microns for irradiation at high energy (electronic regime). Therefore, to make the comparisons easier, all the parameters obtained by calculation for the different irradiation conditions are given in Table 2 (R_p is the maximum of the implantation concentration depth and R_d the maximum of the defect concentration depth). In addition, we point out that the irradiation flux used was about 1 to 2 x 10^{12} ions.cm^{-2}.s^{-1} when using carbon,

argon or helium ions and about 6 x 10^{10} to 1 x 10^{11} ions.cm^{-2}.s^{-1} when the irradiation was with sulphur or iodine ions.

Table 2: Table summarising the chosen irradiation parameters and their associated characteristics notably in the implanted zone, determined by SRIM calculations for a graphite with a density of 2.2

Ion used	Energy (MeV)	Irradiation fluence (ion.cm^{-2})	Rp (nm)	Rd (nm)	S_e (keV/µm)	S_n (keV/µm)	Number of dpa
					In the implanted zone ($\approx$ 315 nm)		
C$^+$	0.4	5 x 10^{16}	675	640	585	15	1.3
C$^+$	0.6	6 x 10^{16}	890	850	730	10	0.9
Ar$^+$	0.8	2 x 10^{16}	630	545	980	175	4.4
He$^+$	15.7	1 to 2 x 10^{16}	121 500	121 500	75	0.003	0.0001 to 0.0002
S^{9+}	100	2 x 10^{15}	24 000	24 000	3 700	1	0.002
I^{19+}	200	2 x 10^{15}	19 100	18 900	16 700	30	0.038

We remind the reader that the irradiation fluence can be calculated from equation [1]:

$$\phi = \frac{I \times \Delta t}{S \times n \times e} \qquad [1]$$

where *I* is the intensity of the ion beam in A, *Δt* is the time of irradiation in s, *S* is the surface irradiated in cm^2, *n* is the charge of the ion and *e* is the elementary charge (e $\approx$ 1.602 x 10^{-19} C).

The fluence depends on the surface of the sample irradiated by the ion beam, the flux and the time. Due to the large number of irradiation experiments done and the different equipment used, the experiments were not always carried out at the same fluence and flux conditions. Thus, the irradiation with carbon, argon and helium ions were done in fluence conditions enabling us to approach the values of 2 to 3 dpa measured in the irradiation conditions in an UNGG reactor [Bonal 2006]. However, irradiation with sulphur and iodine ions was restricted by the constraint of the beam intensity and the length of time the equipment was available, thus explaining the lower fluences obtained. On average, irradiation with carbon and argon ions took between 4 and 6 h, those with helium ions 3 h and finally, those with sulphur and iodine ions between 6 and 10 h.

In an UNGG reactor, the energy input by electronic excitation is between 0 and 700 keV/µm and may even go up to 1600 keV/µm. However, we also investigated the domains above the track creation threshold estimated in HOPG by certain authors [Liu 2006, Lehtinen 2011] as about 7300 ± 1500

keV/µm. The track creation is a process which occurs in about 10^{-11} s. It can be interpreted with the help of the thermal spike model which can explain certain structural modifications caused by irradiation with high energy ions. Since its application to metals in 1956 [Seitz 1956], this model has been revised by Toulemonde [Toulemonde 1993, Toulemonde 2012]. The model is based on the theory that the energy of the incident particle, passed on to the atoms in the matter network *via* an electron-phonon interaction, is converted into thermal energy i.e. heat. In the cylindrical region that the ion passes through, if the energy passed on is sufficiently high for the temperature of the ion network to reach the matter fusion temperature, then melting of this region is observed. The melted zone cools rapidly, there is a tempering phenomenon which could lead to recrystallization. The track corresponds to this cylindrical zone which recrystallizes. The radius of these tracks depends on the volume which reaches the melting point.

Figure 2 summarises the simulation results for the ions in our study (using the software SRIM-2013 [Ziegler 1985, Ziegler 2010]) at a depth of about 300 nm in a graphite with a density of 2.2 g/cm^3 and for the irradiation fluences chosen for these the experiments (summarised in Table 2).
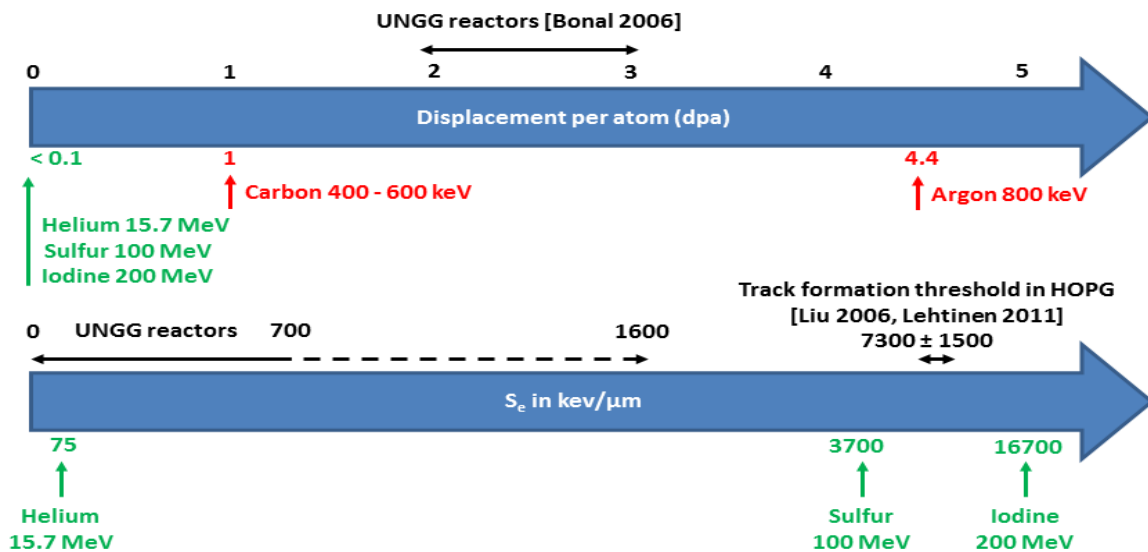
Figure 2: *Number of dpa and electronic stopping power S_e calculated in the implanted zone ($\approx$ 315 nm) in graphite with a density of 2.2 using the SRIM-2013 software for irradiation with the chosen ions, energy and fluence. The number of dpa were calculated for a fluence of 5x10^{16} at.cm^{-2}*

As can be seen on the above Figure, the ions used to predominantly cause ballistic effects are given in red and those used for electronic excitation are in green. We can therefore conclude that, in order to work in a ballistic regime, it is better to use carbon ions with an energy of between 400 and 600 keV. It is also possible to induce a greater number of dpa in the graphite by irradiating with low energy argon ions. For the electronic regime, we chose to work with 15.7 MeV helium ions. However, it is still interesting to use 100 MeV sulphur ions in order to work outside the range of electronic stopping power of UNGG reactors or above that with 200 MeV iodine ions in order to obtain an extremely large electronic stopping power which is well above the track creation threshold in HOPG.

1.2 | Description of the irradiation equipment

Two set-ups have been used for irradiation experiments in different configurations.

1.2.1 | For irradiation under vacuum

Figure 3 includes a schematic and photograph of the cell used in the first set-up, i.e. in the configuration for irradiation under vacuum. The advantage of this cell, which was designed and made in the laboratory, is that it is transportable and has been installed in the different accelerators for the various irradiation experiments.
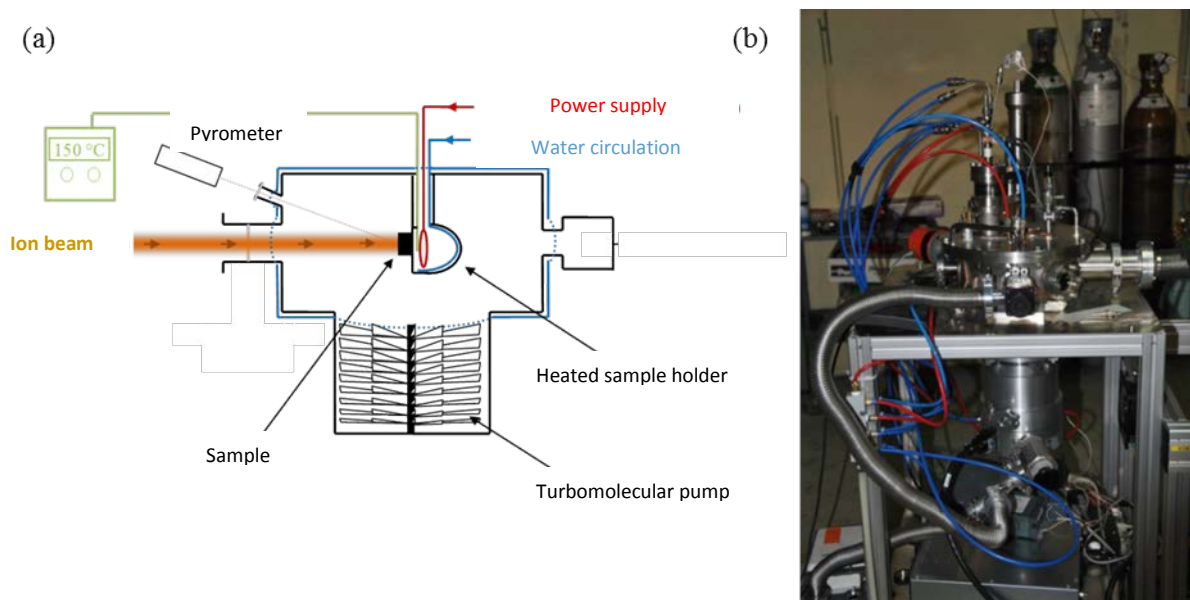
Figure 3: *(a) schematic of the experimental set-up and (b) photograph of the cell used for the irradiation experiments*

During irradiation, the sample is put in the irradiation cell, where the top side is perpendicular to the incident beam axis. The cell is put under vacuum (in the order of 10^{-6} mbar). A heating element fixed to the sample holder enables the sample to be heated to up to 1000 °C. The temperature is measured at the back of the sample via a thermocouple, and on the irradiated side of the sample *via* a pyrometer. These temperature measurements enable the power of the heating element to be regulated. Cold water circulation enables the cell walls to be cooled as well as the turbomolecular pump.

1.2.2 | For irradiation under « UNGG gas » with *in situ* Raman analysis

In order to reach irradiation conditions similar to those in an UNGG reactor, we chose to irradiate the graphite at the interface with a gas. At the same time, we wanted to simulate the S_e values

in the range of those reached in these reactors, so we irradiated with helium ions, where their energy at the sample surface is 15.7 MeV and where the electronic stopping power in the implanted zone is 75keV/µm. These experiments were done on a cyclotron beam line in the CEMHTI in Orléans.

The above experiments were special because, during the experiment, the structural modifications in the graphite were followed by *in situ* Raman analysis. This new method required the development, in collaboration with the CEMHTI, of a new irradiation cell (under gas) with a heated sample holder. This unique cell is shown in Figure 4.
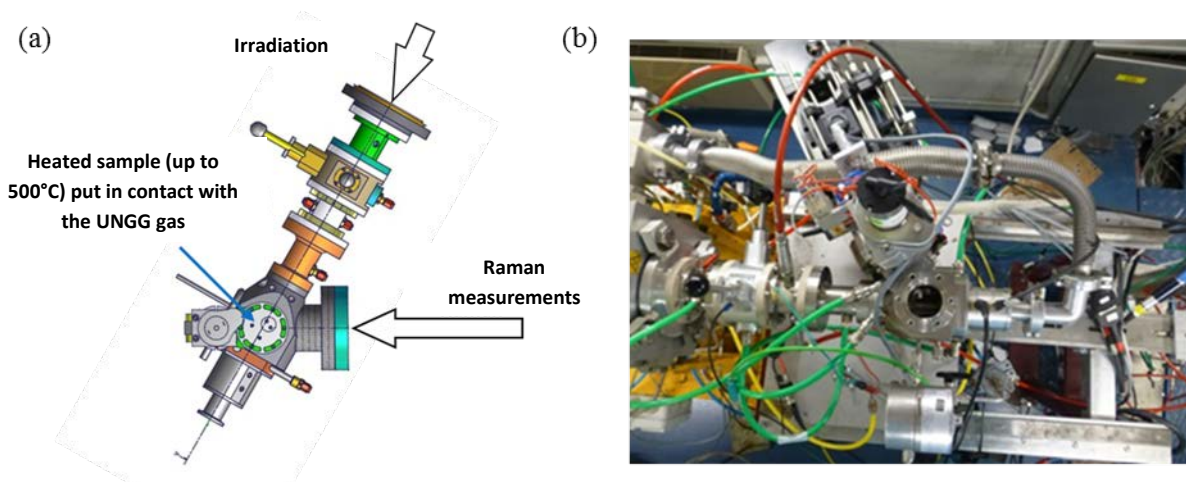
Figure 4: *(a) Schematic of the irradiation cell used for the in situ Raman analysis and (b) photograph of this cell on the cyclotron*

To reach the temperatures of those attained by the graphite in a reactor, the samples were heated from ambient temperature to 500 °C. A gas which is representative of the coolant gas of the UNGG reactors in Saint-Laurent-des-Eaux was chosen. The composition of this gas, henceforth known as « UNGG gas », was determined from the data in the literature. The details are given in Table 3.

Table 3: *Chemical composition of the representative mixture of the coolant gas of the SLA2 reactor*

Chemical compound	Concentration
CO_2	Balance (see the paragraph below)
CO	2.5 % vol.
CH_4	500 ppm (by volume)
O_2	100 ppm (by volume)
H_2	100 ppm (by volume)

The above mixture is "made-to-measure" by the company Praxair. The main gas called the "balance" gas is CO_2. The relatively high methane content is not representative of all UNGG reactors. When brought into contact with the sample, this UNGG gas could be radiolyzed and so result in the phenomenon of radiolytic corrosion of the graphite.

For our experiments, we chose to irradiate samples of nuclear graphite and HOPG. The nominal energy of the He$^+$ ions is 28 MeV, i.e. 22.4 MeV when the gas enters the irradiation cell and 15.7 MeV at the surface of the graphite sample. The simulations of energy loss of the helium ions in this gas/graphite system were made using the SRIM-2013 software [Ziegler 1985, Ziegler 2010] and the results are presented in Figure 5, where *a* represents the whole system, *b* the stopping power of the gas and *c* the stopping power of the graphite.
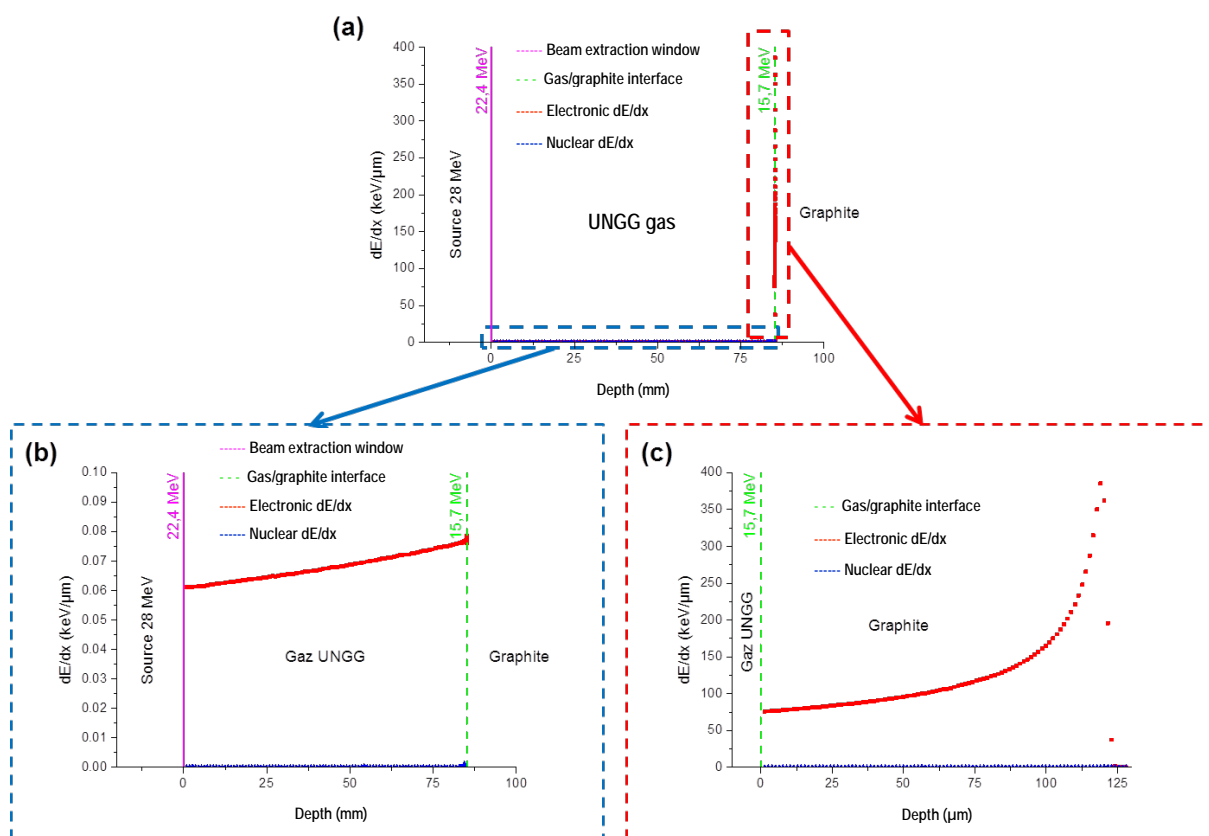
Figure 5 : *Results of the irradiation simulations with He$^+$ ions of 22.4 MeV at the entrance of the irradiation cell (in the gas) and 15.7 MeV when they arrive at the graphite surface, realised using the SRIM-2013 software: (a) whole simulation, (b) only in the gas and (c) only in the graphite*

Figure 5 *b* shows that the amount of energy transferred to the gas is very low. Figure 5 *c* shows that, in the implanted zone (from 250 to 300 nm) and probed by Raman microspectrometry, the S$_e$ value is about 75 keV/μm. On the other hand, the Sn value is almost zero which means that the graphite undergoes practically no ballistic damage other than that caused by the implanting of ^{13}C or ^{37}Cl.

The principal characteristics of irradiation in the above configuration are given in Table 4.

Table 4: *Principal characteristics of irradiation in conditions similar to those encountered in an UNGG reactor*

Ion	He
Energy at the sample surface	15.7 MeV
S_e in the implanted zone (315 nm)	$\approx$ 75 keV/µm
Temperature	From T_{amb} to 500 °C
Atmosphere	Gas similar to the coolant gas in UNGG reactors
Speciality	Analyses by *in situ* Raman microspectrometry

Now that we have described the experimental conditions chosen for the study of the effects of irradiation on the mobility of implanted ^{13}C and on the structure of graphite, we present the results obtained.

2 | Effect of temperature alone

Before looking closely at the irradiation effects, we wanted to verify the effects of temperature alone. In order to do that, we heated the samples in the same conditions as the irradiation i.e. each was put in the heated sample holder in the irradiation cell under a secondary vacuum during periods of 5h (average irradiation period) at different temperatures. In this section, we present the results obtained.

2.1 | For graphite samples initially very disordered

2.1.1 | Structural behaviour of graphite

Figure 6 shows the Raman spectra for the as-implanted samples (TQI) ([13]C - ϕ = 6 x 10^{16} at.cm^{-2} – 7.4 dpa) and heated for 5h at 400, 600 and 1000 °C.
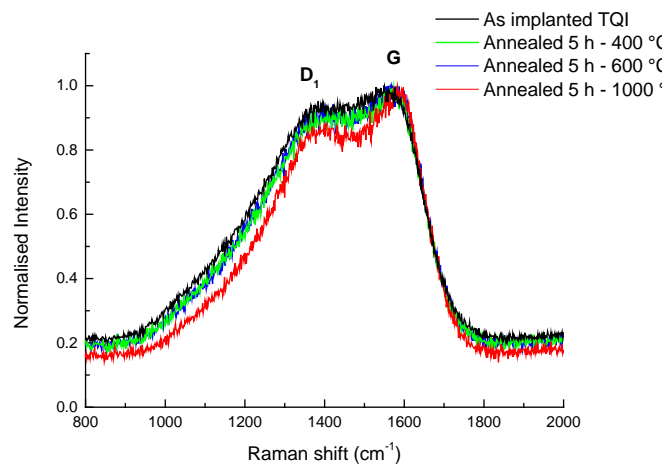
Figure 6 : *Raman spectra obtained from the samples implanted with ^{13}C and heated for 5 h at 400, 600 and 1000 °C compared to the Raman spectra of an as-implanted sample (TQI)*

On Figure 6, we observe that the spectrum for the TQI sample that both band G and band D_1 are high intensity and broad which is synonymous with very disordered graphite. This therefore shows that the graphite does not seem to reorder even at a temperature of 1000 °C. In fact, the spectra of the heated samples are very similar to those of the TQI sample even though we observe a slight decrease in the intensity and the width of band D_1 for the sample heated at 1000 °C.

We can thus conclude that temperature has a negligible effect on the reordering of graphite during 5h periods of heating.

2.1.2 | Migration behaviour of ^{13}C in graphite

We also studied the effect of temperature on the mobility of the implanted ^{13}C. Figure 7 shows the ^{13}C concentration curves obtained by SIMS analysis on a TQI sample, as well as on samples heated for 5h at 400, 600 and 1000 °C. Table 5 gathers the values for the area under the curve, full width at half maximum height (FWHM) and the Rp value for each curve given in Figure 7.
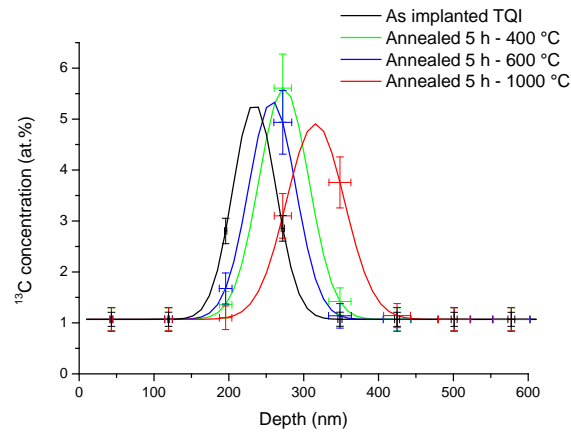
Figure 7: *¹³C concentration curves obtained by SIMS analysis on a TQI sample as well as on samples heated for 5h at 400, 600 and 1000 °C*
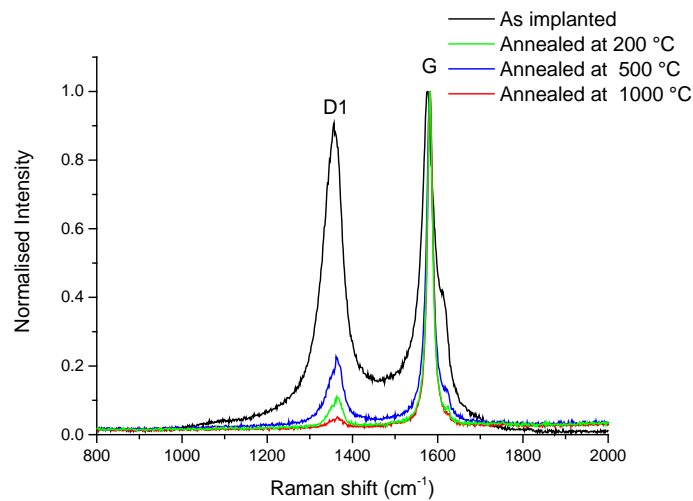
Table 5: *Values for the area, total width half-height and the Rp value for the ¹³C concentration curves from the samples heated at different temperatures*

	Area (% at.nm)	FWHM (nm)	Rp (nm)
TQI	306 ± 17	68 ± 7	234 ± 2
400 °C	378 ± 19	78 ± 8	274 ± 12
600 °C	338 ± 18	74 ± 7	258 ± 11
1000 °C	372 ± 19	91 ± 9	316 ± 13

The above Figure and values in the table show that the curves for the heated samples are very similar to those of the TQI sample except for the sample heated at 1000 °C which has slightly shifted. During heating, the areas under the curves and the FWHM values are similar, taking into account the uncertainties. There is therefore no release of ¹³C. We can thus conclude that temperature has a negligible effect on the mobility of implanted ¹³C in graphite.

2.2 | For initially slightly disordered graphite samples

We have also studied the behaviour of samples which were initially slightly disordered by the implanting of ³⁷Cl. Figure 8 shows the state of the structure of the implanted graphite (³⁷Cl - ϕ = 5 x 10^{13} at.cm^{-2} – 0.02 dpa) studied by Raman microspectrometry at different temperatures.

CAST
**Report on ^{13}C behaviour under ion irradiation in HOPG
(model graphite) (D5.18)**

EURATOM

Figure 8 : *Raman spectra obtained for the TQI ^{37}Cl sample as well as samples implant and heated at 200, 500 and 1000 °C*

The above Figure shows that the Raman spectra for the TQI sample consist of two very distinct bands, G and D_1 and both are high intensity, sharp peaks. When the implanted sample is heated, the intensity of the band indicating the structural defects (band D_1) greatly decreases. We can therefore say that the structure of the graphite is progressively reordered from 200 °C. Please note that this behaviour is observed whatever the nature of the implanted ion (^{37}Cl or ^{13}C).

# 3 | Effect of irradiation in a mainly ballistic regime

In this section, we present the results obtained from irradiation in a mainly ballistic regime. We study the structural state by Raman microspectrometry as well as the evolution of the ^{13}C concentration profiles obtained by SIMS after each irradiation and we compare these with those of the TQI samples in order to observe any possible migration phenomena of the ^{13}C in the graphite due to the effect of irradiation.

3.1 | For initially very disordered graphite samples

As stated previously, we started by studying the effect of irradiation on the surface and structure of the graphite as well as the evolution of the concentration profiles of the implanted ^{13}C. First, we show the surface state using images obtained by SEM, then we give the results obtained by Raman microspectrometry concerning the structural state of the graphite. Finally, we present the ^{13}C concentration profiles obtained by SIMS.

3.1.1 | Study of the graphite surface by SEM

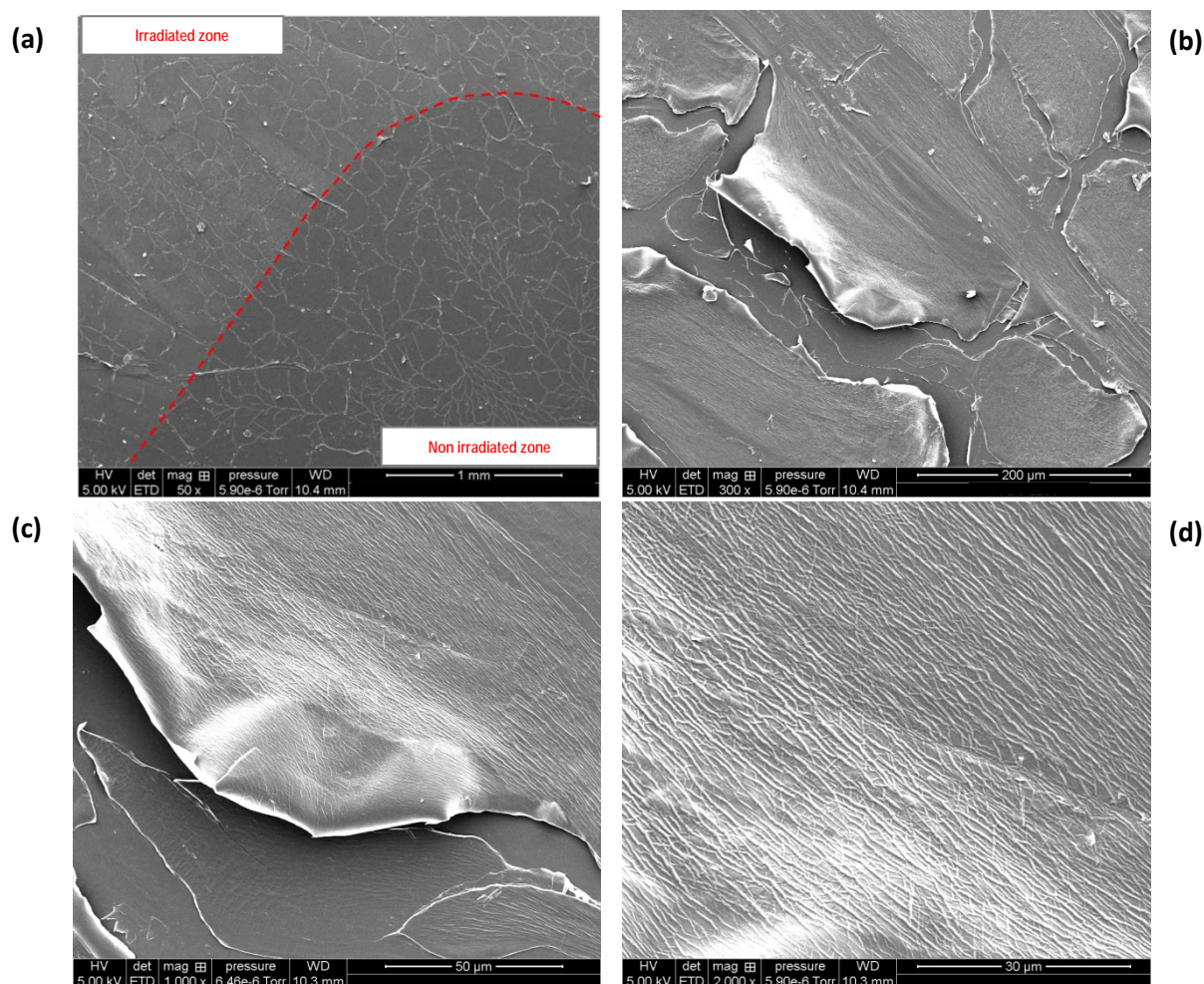SEM observation of the samples after irradiation shows much surface damage. Figure 9 shows the state of the surface after irradiation with argon ions at ambient temperature.
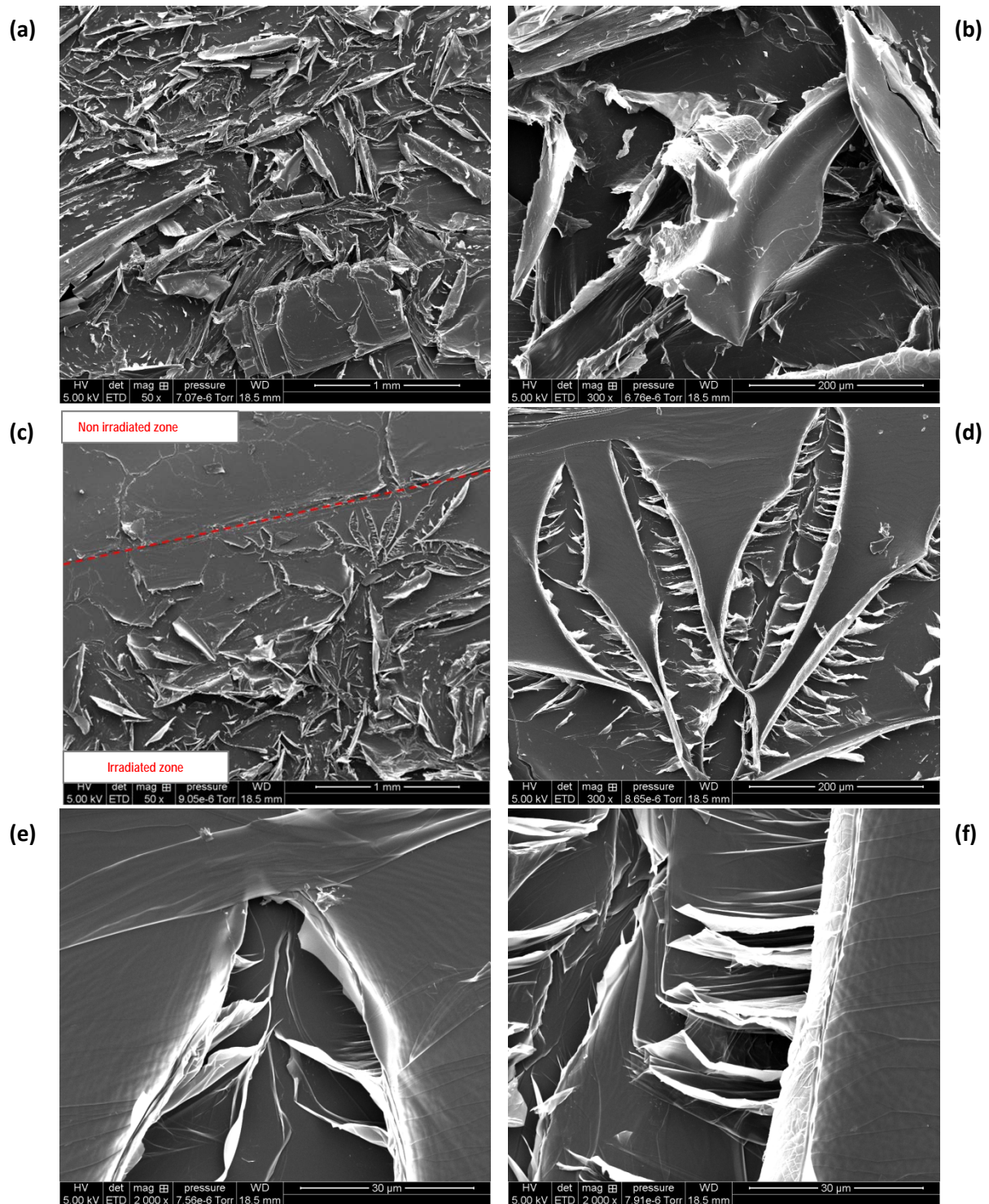
Figure 9: *SEM observation of the surface state at different magnifications for samples irradiated with 800 keV Ar^{+} ions at ambient temperature (a, b) in the centre of the irradiated zone and (c, d, e, and f) on the edge of the irradiated zone*

Figures 9*a* and *b* are from the centre of the irradiated zone. They show that the surface is very disordered. However, on the edge of the irradiated zone (image *c*), the damage is less. This observation reveals the way in which the disordering process is initiated. We observe a wider opening of the fissures and the separation of layers from the surface which also curl up and separate from the surface (images *d*, *e* and *f*).

Figure 10 shows the state of the surface after irradiation with argon ions at 600 °C. On image *a*, we can identify two zones. First, a darker zone which corresponds to the non-irradiated area (the area under the part holding the sample in place during irradiation) and, second, a lighter irradiated zone. The three other images were taken of the irradiated zone and show surface layers which are in the process of detaching from the rest of the sample. The surface of the sample is also covered with wrinkles oriented in the same direction as in image *d*.

Figure 10 : *SEM observation of the state of the surface of the samples irradiated by 800keV Ar$^+$ ions at 600 °C at different magnifications*

Finally, Figure 11 shows the state of the surface after irradiation with argon ions at 1000 °C. Image *a* shows the edge of the irradiated zone. We can therefore compare the state of the surface of the irradiated zone on the left side of the image with the non-irradiated zone, i.e. the TQI sample on

the right-hand side. The images b, c, d, e on the one hand, and f, g, h on the other, show two different zones with layers curled up at the edges covered with wrinkles in the irradiated part. Image i shows the wrinkled surface layers in which a hole has formed. This allows the lower layers to be seen; they are covered with larger wrinkles. Finally, in image j we see layers of different thicknesses which fissure and curl up during irradiation.
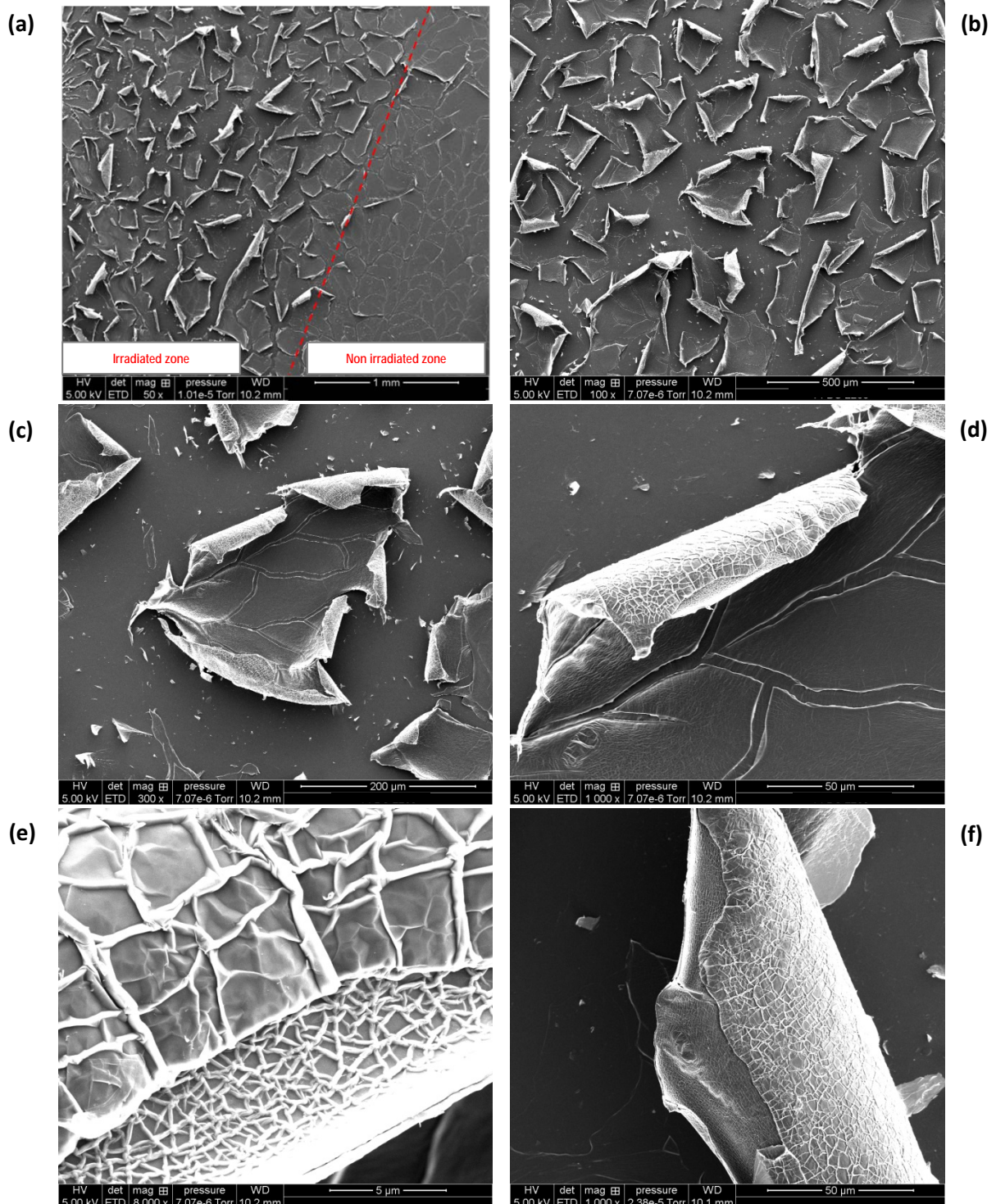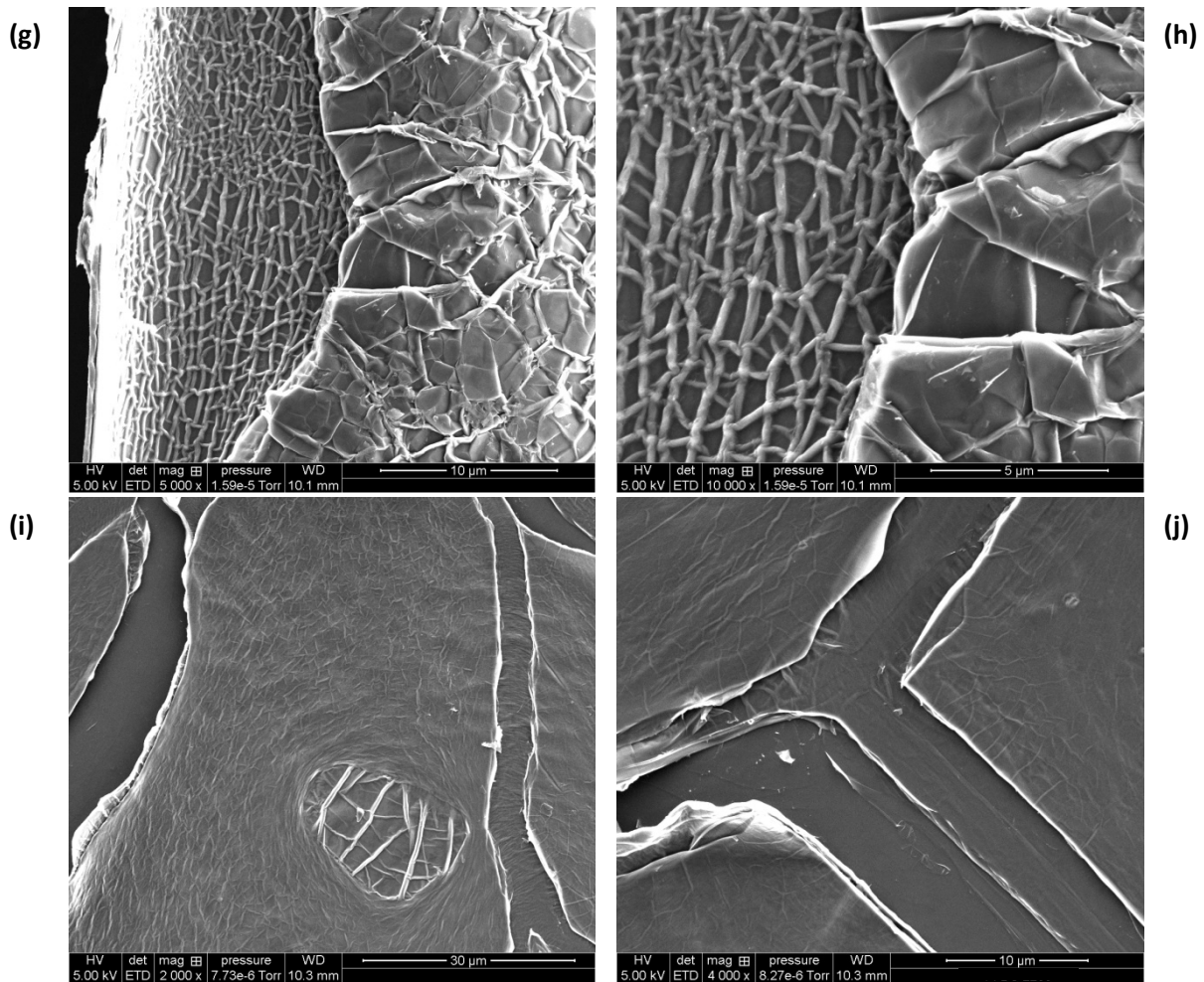
Figure 11 : *SEM observation of the state of the surface of the samples irradiated with 800 keV Ar$^+$ ions at 1000 °C and at different magnifications*

In general, we observe that irradiation at ambient temperature causes more damage of the sample surface than irradiation at higher temperatures. Furthermore, on the images with the highest magnification, we can see the phenomena at the origin of the significant surface damage from irradiation of the sample as seen in images *d*, *e* and *f* of Figure 9, *c* and *d* of Figure 10 and *d*, *e*, *f*, *g*, *h*, *i* and *j* of Figure 11. On these different images, we observe zones where the surface layers begin to rip open as shown on image *e* of Figure 9. The stack of layers then curl up on themselves following the fissure as can be seen on image *c*, *d* and *f* of Figure 11. Certain layers are wrinkled with ridges appearing on the surface such as those shown in image *d* of Figure 10 or image *i* of Figure 11. When we see the curling of the stack of layers at a higher magnification, we observe that the layers have more or less fine ridge formation depending on the depth at which they are found, as on images *e*, *g* and *h* of Figure 11. This phenomenon is illustrated in Figure 12.
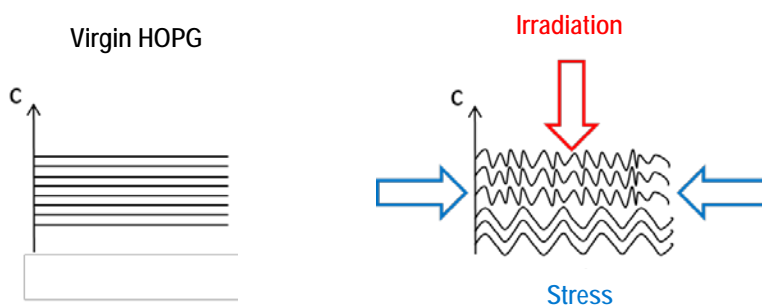
Figure 12 : *Representation of the hypothesis for ridge formation on the surface layers*

We made topographic measurements by optical interferometry of the irradiated surfaces in the zones similar to those observed on the SEM images presented previously (Figure 11). Figure 13 illustrates the results obtained schematically. In order to have a better idea of the distance separating the layers (c.f. the blue square insert in Figure 13), we measured and evaluated the zone corresponding to image *e* in Figure 11 at 2 µm. Besides this, on these same graphite samples, other zones with stacks of curled layers such as those given in Figure 14 show that these stacks are clearly separate.
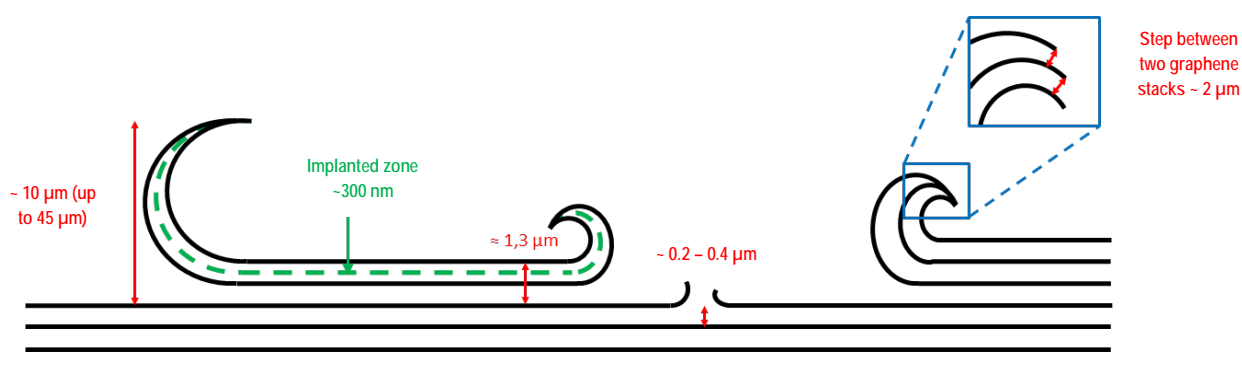
Figure 13 : *Representation of the optical interferometry measurements realised on the disordered surface of the sample irradiated with 800 keV Ar $^+$ ions at 1000 °C*
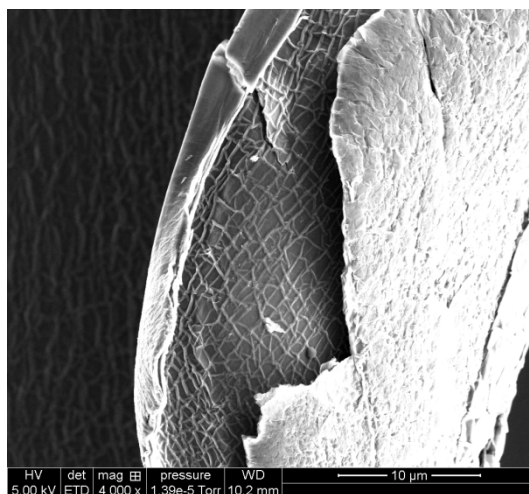
Figure 14: *An SEM image showing the spacing between two stacks of graphene planes on the curve of a petal on the surface of a sample implanted in ^{13}C then irradiated with 800 keV argons ions at 1000 °C*

It is important to point out that the state of the surface of samples irradiated with carbon ions is not comparable with that of samples irradiated with argon ions. In fact, it is much less disordered because irradiation with carbon ions leads to less than 1 dpa on the surface whereas with argon ions irradiation leads to 4.4. Therefore, the corresponding images with carbon ions are not shown here.

We did Raman analyses on the different layers and the results are presented in the next section.

3.1.2 | Study of the effects of the constraints of irradiating with argon ions

Due to the highly damaged surface on the samples irradiated in a ballistic regime, which is even observable with the naked eye, it is interesting to analyse the different zones identified previously by Raman microspectrometry i.e. the cracked outer layers which are wrinkled/ridged and folded back on themselves (n°1 in Figure 15 *a*) and the layers at lower depths which are visible through the fissured layers on the surface (n° 2 and 3 in Figure 15 *a*). We therefore did several mappings by Raman microspectrometry on a particularly damaged sample but on which the layers close to the surface are still intact. This sample had been irradiated with 800 keV Ar$^+$ ions at 1000°C (a fluence of 2×10^{16} ions.cm^{-2} and a flux of 1.3×10^{12} ions.cm^{-2}.s^{-1}). We chose several zones with cracked surface layers as well as the deeper layers which are visible in these cracks. It was important to avoid the layers which are curled up on the surface because the higher altitude of the latter would mean modifying the optimisation of the laser used for the Raman analysis. In the next paragraph, we present the results of one of these mappings. The chosen zone is in the centre of the irradiated zone and it is shown on the SEM images at different magnifications in Figure 15.
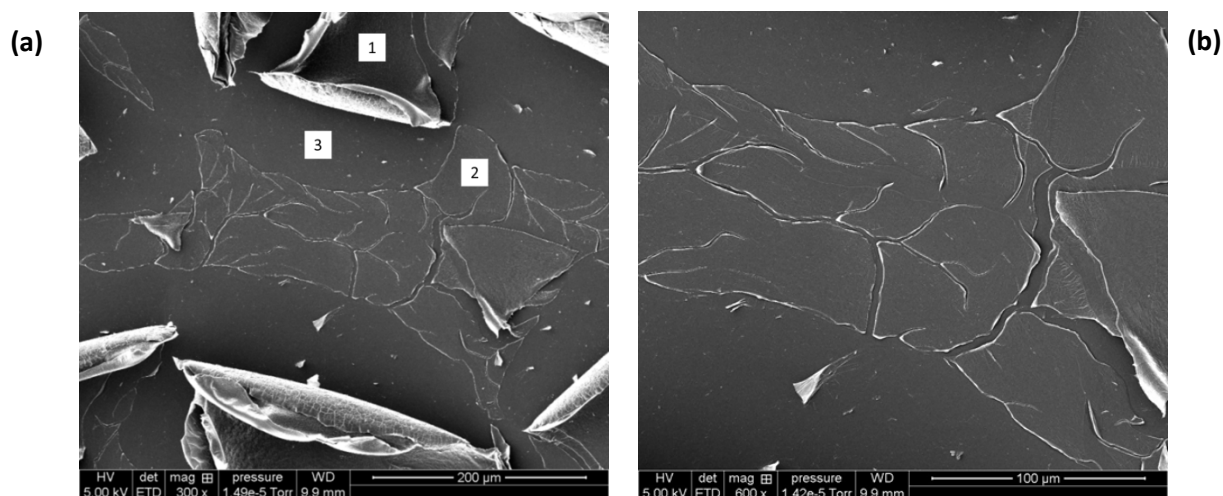
Figure 15: *SEM observation of the zone mapped using Raman microspectrometry at different magnifications*

Using Raman microspectrometry, we first analysed certain zones identified on the SEM image in Figure 15 ***a***. These correspond to the initial surface of the sample (n° 1) and the lower planes at different levels revealed by the lifting/separating of the surface layers during irradiation (n° 2 and 3). The Raman spectra corresponding to these zones are given in Figure 16.
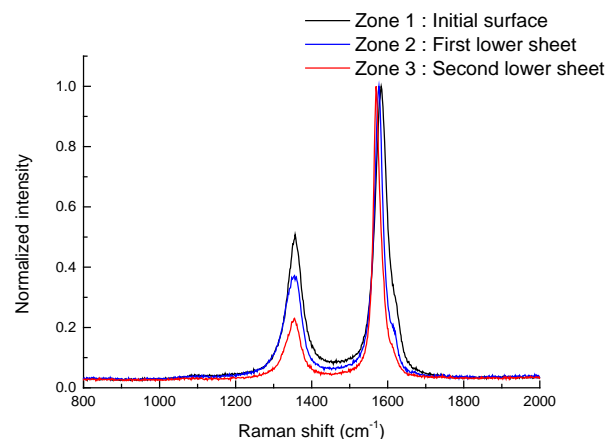
Figure 16 : *Raman spectra realised in different zones of the sample irradiated with 800 keV Ar$^+$ ions at 1000 °C. These zones are indicated on the SEM image in Figure 15 at a magnification of 300*

The spectra in Figure 16 show that the closer to the surface of the sample, the more intense is the defect band D_1, i.e. the more the sample is damaged/disordered. This can be explained by the fact that the planes closest to the surface had been damaged by the implanting of ^{13}C and the irradiation, whereas the deeper planes are probably situated at a distance greater than Rp for the implanting and are therefore only disordered by the irradiation.

The zone shown in Figure 15 ***b*** was also analysed by optical interferometry with the view to measuring the difference in altitude between the surface layers and those deeper, on the edges and in

the cracks, and thus being able to estimate the thickness of the fissured layer. The interferometry analysis result is given in Figure 17. We can clearly see the chosen zone: in dark blue the lower plane and in green and turquoise the upper plane. The height difference between these two planes is virtually the same on the edges of the planes as in the cracks and corresponds to about 600 nm. Just for the record, the height of the planes folded in on themselves is greater than 1.5 µm but may even reach 6 µm at the maximum height of the fold.
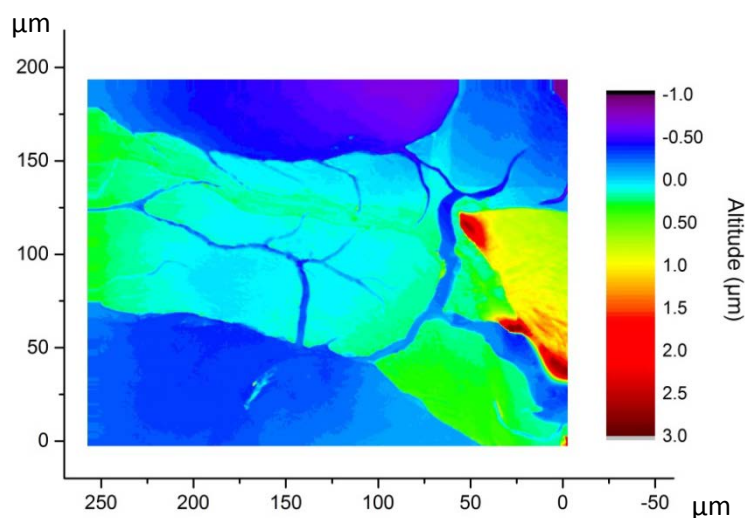
*Figure 17: The topography measured by optical interferometry for the chosen zone and analysis by Raman microspectrometry*

In the centre of the zone given in Figure 17, we mapped a surface of 60 x 80 µm^2 by Raman microspectrometry. Different parameters characteristic of these spectra were studied such as the I_D/I_G ratio, the intensity and area of the bands and also the full width half maximum. The I_D/I_G ratio seems to indicate that the graphite is more **disordered** at the bottom of the cracks and therefore in the lower layers, as it is about 0.50 compared to 0.35 on the upper plane. However, the parameter which changes the most significantly on the Raman spectra is the position of band G. The mapping in Figure 18 *b* represents the value of the position of this band in cm^{-1}. On the same Figure, the SEM image (Figure 18 *a*) shows the zone on which the mapping was done.
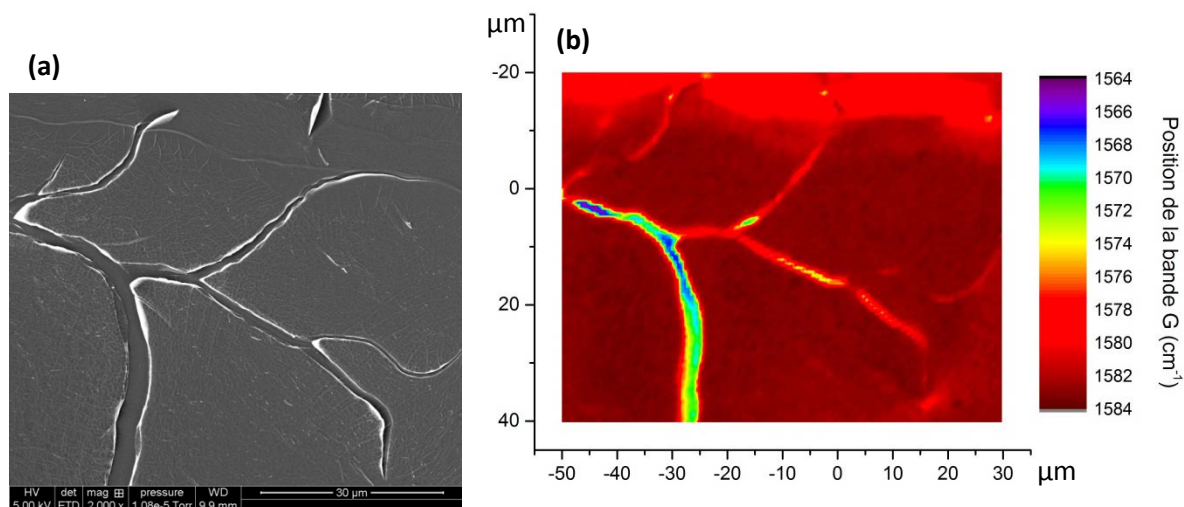
Figure 18 : *(a) SEM image of the mapped zone and (b) the evolution of the position of band G in the Raman spectra of this zone*

The Raman mapping in Figure 18 ***b*** shows that the Raman signal is strongly linked to the position at which the sample is analysed. On the other hand, this mapping indicates a great disparity in the position of band G as a function of the zone analysed. In fact, on the surface layers, band G is at about 1583 cm^{-1} whereas at the bottom of the fissures, i.e. on the lower layers, we can find it up to about 1563 cm^{-1}. However, we know that for virgin HOPG or the TQI HOPG, this band is normally situated at 1582 cm^{-1} [Ferrari 2000], which means that the G band is shifted towards the lower values, a shift of about 20 cm^{-1}. Consequently, we can suppose that the lower layers have been disordered more significantly during the irradiation of the top surface layers.

Work done in 2011 consolidates the above hypothesis [Frank 2011 a]. In fact, in this study, an analysis by Raman microspectrometry was made on a monolayer of graphene submitted to uniaxial deformation due to strain i.e. tension or compression. The evolution of the G band for the graphite shows a splitting of this band into two sub-bands, G[-] and G[+], observed in both directions of the physical strain. There was also a decrease in the band symmetry. Figure 19 shows the results obtained concerning the evolution of band G.
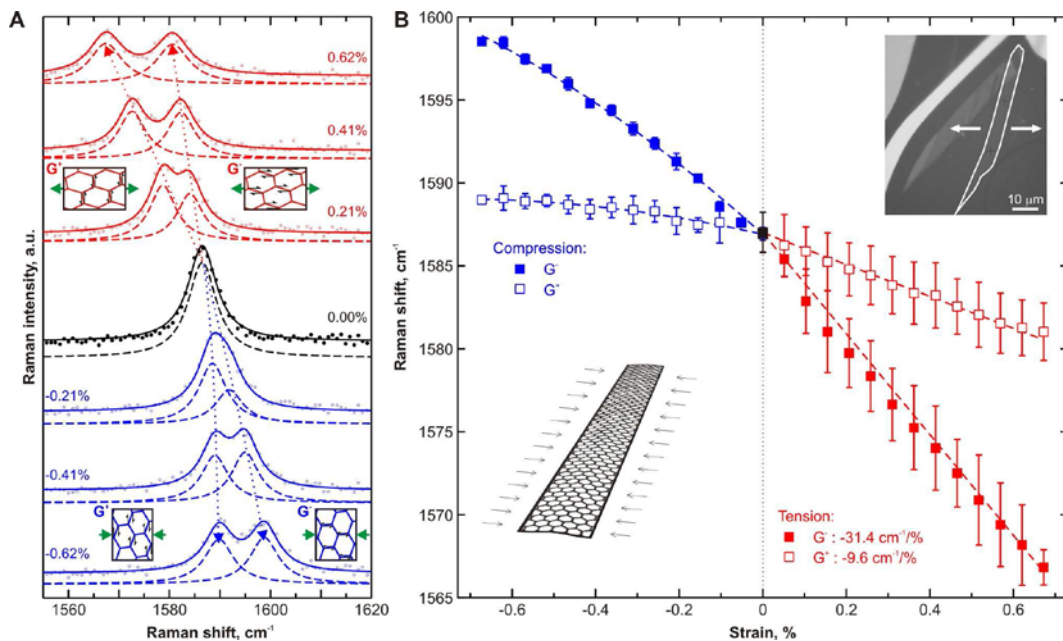
Figure 19: *Evolution of band G in a monolayer of graphene (image inserted in B) under uniaxial constraint observed by Raman microspectrometry ($\lambda_{excitation}$ = 785 nm) [Frank 2011 a]*

On Figure 19, the spectra (in ***A***) and the positions of the sub-bands G (in ***B***) are in red for the tension, in blue for the compression and in black when no strain was applied. The amount of strain is indicated (in %) for each series of curves. The dotted curves (in ***A***) are the individual Lorentzian components from the experimental spectrum (points) and the dashed curves represent their convolutions. The dotted lines (in ***B***) represent the adjustment of the linear experimental points for the tension (the rates of displacement are given in the legend) and a second-order polynomial for the compression.

As can be seen on Figure 19, in general, tension leads to a shift in band G towards lower *Raman shift* values (*phonon softening* – in red on the Figure), whereas compression leads to a shift in band G towards the higher *Raman shift* values (*phonon hardening* – in blue on the Figure). In addition, the splitting of band G into two components is due to a decrease in the symmetry of the crystalline matrix [Frank 2010, Frank 2011 b, Sgouros 2016]. The diagrams for the vibration modes specific to bands G[+] and G[-] as a function of the strain axis are shown in Figure 19 ***A*** [Frank 2011 a] as well as on Figure 20 [Mohiuddin 2008].
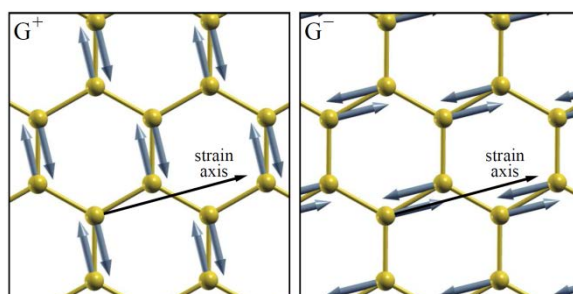
Figure 20 : *Schematic of the vibration modes for bands G[+] and G[-], resulting from the splitting of band G, as a function of the strain axis [Mohiuddin 2008]*

In our case, band G shifted to 1563 cm^{-1}, which means that from this study the lower layers are strained, notably tension. We can therefore draw the hypothesis that irradiation at 1000 °C leads to tension in the graphene planes and therefore the layers (superposition of several graphene planes). The layers on the surface are torn off by the combined effect of tension and irradiation (which tears the atoms from the graphene planes) thus releasing the strain for the surface layers but not for those deeper down, which are thus less impacted by the slight disordering associated with irradiation (lower dpa).

However, our case was different from the study presented previously [Frank 2011 a] in that band G did not clearly split because the strain was not uniaxial.

Mapping could not be done on the samples irradiated at ambient temperature due to the fact they were greatly damaged on the surface, as can be seen on the SEM images in section 3.1.1. Thus, this highly contrasted topography prevented us from realising Raman mapping in the irradiated zone.

3.1.3 | Study of the structure of graphite by Raman microspectrometry

We will now compare the Raman spectra obtained from the samples irradiated with either a carbon or argon ion beam at different temperatures. Irradiation with C[+] ions with energies of 400 or 600 keV are done at fluences allowing us to reach about 1 dpa in the implanted zone, whereas irradiation with 800 keV Ar^{+} ions allow us to reach 4.4 dpa. The Raman microspectrometry spectra of the irradiated samples in these conditions are presented in Figures 21 *a* and 21 *b*, respectively, and compared with the spectrum from the TQI sample. In addition, table 6 gives the values of the I_{D1}/I_G ratio for the samples only heated as well as for those irradiated with carbon or argon ions at different temperatures.

(a)

(b)
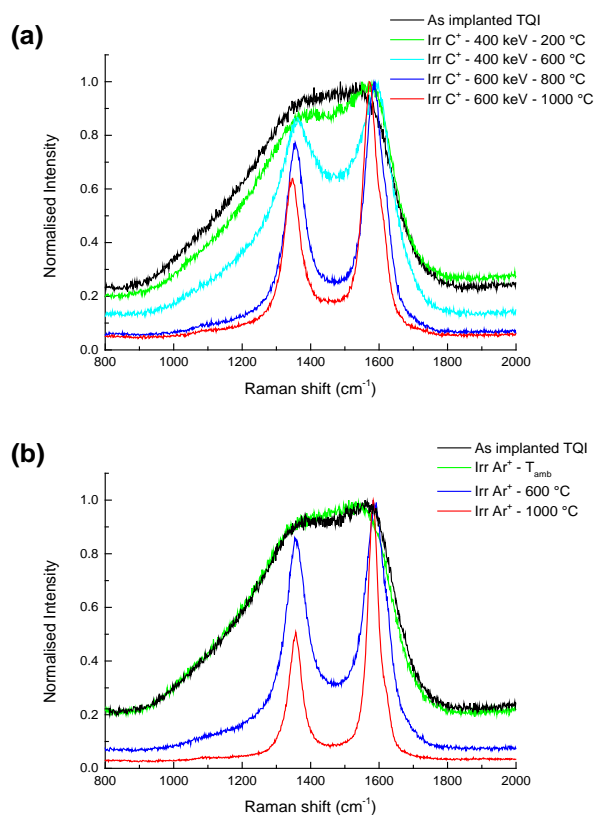
Figure 21: Comparison of the Raman spectra for a As implanted TQI sample with those of samples irradiated with (a) carbon or (b) argon ions at different temperatures

Table 6: Values with respect to the I_{D1}/I_G intensity ratio for the samples only heated or irradiated with carbon or argon ions at different temperatures

	I_{D1}/I_G		
	Heated only	Irr. C$^+$	Irr. Ar$^+$
TQI	**0.94**	**0.95**	**0.94**
T_{amb}	-	-	0.95
200 °C	-	0.89	-
400 °C	0.92	-	-
600 °C	0.93	0.87	0.86
800 °C	-	0.77	-
1000 °C	0.88	0.64	0.51

CAST
Report on ^{13}C behaviour under ion irradiation in HOPG
(model graphite) (D5.18)

Figure 21 (a) shows that for irradiation with carbon ions, the G and D_1 bands are clearly separated and become narrower with the increase in temperature, which signifies a dynamic heating of the defects resulting from the implantation process. On the other hand, the values given in table 6 show that the I_{D1}/I_G ratio decreases with temperature, indicating a progressive reordering of the graphite. In fact, in well-structured graphite, the majority of C-C bonds are aromatic sp^2. However, during the implanting process, the disordering leads to the presence of isolated defects (vacancies, interstitials) but also more significant defects such as fractured graphene planes. Thus, the Raman signal defect band i.e. D_1 broadens and its intensity increases [Ammar 2015]. During irradiation at a higher temperature, the isolated defects combine and so may form new well-ordered graphene planes. The increase in the number of C-C sp^2 bonds leads to a structural rearrangement which is revealed in the spectra as a narrowing of band D_1 and a decrease in its intensity.

Comparison of the results in Table 6 with those obtained in the study of the effect of heating alone (section 2.1.1), show that temperature and irradiation in a ballistic regime seem to have a synergistic effect with respect to the restructuring of graphite. In fact, when the sample is only heated at 1000°C, the structure reorganises significantly less than under irradiation at 1000 °C. Figure 21 *b* shows the synergy effect between ballistic irradiation and temperature on reordering which is even clearer when irradiating with argon ions. For example, the spectrum obtained with the sample irradiated at 600°C is in a better structural state than that corresponding to the sample irradiated with carbon ions at 600°C. In fact, the D_1 and G bands are broader for irradiation with carbon ions compared to those observed for irradiation with argon ions and the intensity between these two bands, attributed to band D_3 by certain authors [Couzi 2016], increases.

In conclusion, the combined effects of temperature and irradiation in a mainly ballistic regime favour a reordering of the graphite structure which was initially highly disordered. We remind the reader that the interstitials are mobile from ambient temperature whereas the mobility of the vacancies increases progressively above 250 °C. The local defect structure stores Wigner energy that can be released by defect rearrangement to configurations with lower energy. The process of recombination of interstitials and vacancies is expected to be the primary step in Wigner energy release observed at 200-250°C [Ewels 2003, Telling 2003]. It would therefore seem that this disordering regime at higher temperature favours the mobilisation and recombination of the defects initially present as well as those caused by irradiation and so enables a progressive reordering of the graphite structure.

3.1.4 | Microstructural study of graphite by HRTEM

We then studied the disordering of graphite during irradiation in a mainly ballistic regime and the results obtained by TEM. We observed the evolution of the inter-layer distances and the angular distributions. The inter-layer distance for virgin graphite is 3.35 Å. However, the larger this value becomes, the more the structure is disordered. The graphs in Figure 22 show the results obtained for graphite samples initially implanted with ^{13}C at 6 x 10^{16} at.cm^{-2} then irradiated with 600 keV C$^+$ ions at 1000°C. The points corresponding to the virgin graphite and the TQI sample also appear on these graphs. The shaded zone covers the Rp value for the implanted ^{13}C and the dashed lines have been

added to guide the eye. These lines allow the trends in the evolution of the values as a function of depth to be more clearly seen.
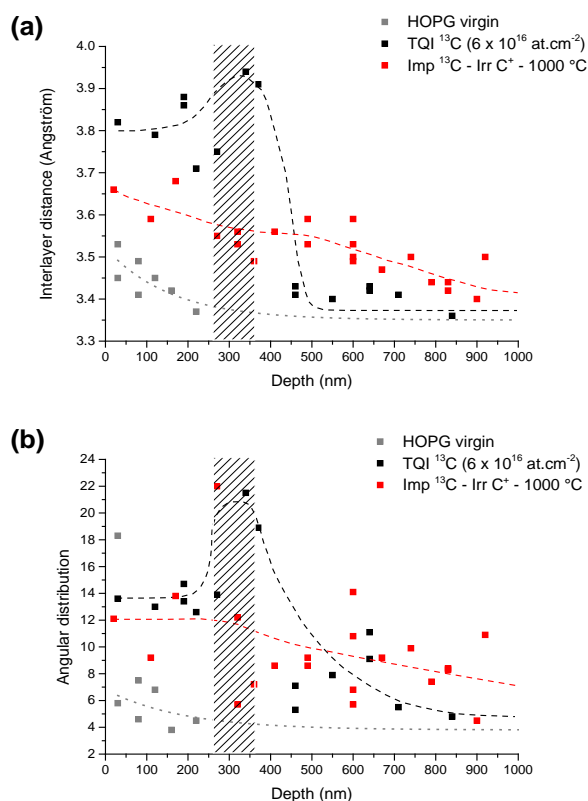
Figure 22 : *Inter-layer distance and angular distribution measured on the TEM images at different depths for the samples implanted with ^{13}C at high fluence then irradiated. The shaded zone covers the Rp value for implanted ^{13}C and the dashed lines enable the trend in the evolution of these values as a function of depth to be more clearly seen*

From the graphs in Figure 22, we observe that the values of the inter-layer distance and the angular distribution are greater in the implanted zone of the TQI sample and decrease notably with depth outside this zone down to values close to those for a virgin sample. However, the values of the sample irradiated at 1000 °C are a little higher on the surface than below but globally more homogeneous and lower than those of the TQI sample. These results indicate a better-ordered structure in the irradiated sample compared to the TQI sample, which is in agreement with the results obtained previously by Raman microspectrometry.

3.1.5 | Migratory behaviour of ^{13}C in graphite

Irradiation with argon ions

We saw previously (in section 3.1.1) that irradiation with argon ions slightly disordered the sample surface so that the topographic measurements could not be exploited. We have therefore

chosen to represent the ^{13}C concentration profiles measured by SIMS as a function of abrasion time and not as a function of depth. The ^{13}C concentration profiles in the samples irradiated with argon ions at different temperatures are compared in Figure 23 with those of the TQI sample. Table 7 gives the values for the areas, full width half height and maxima of the concentration profiles.
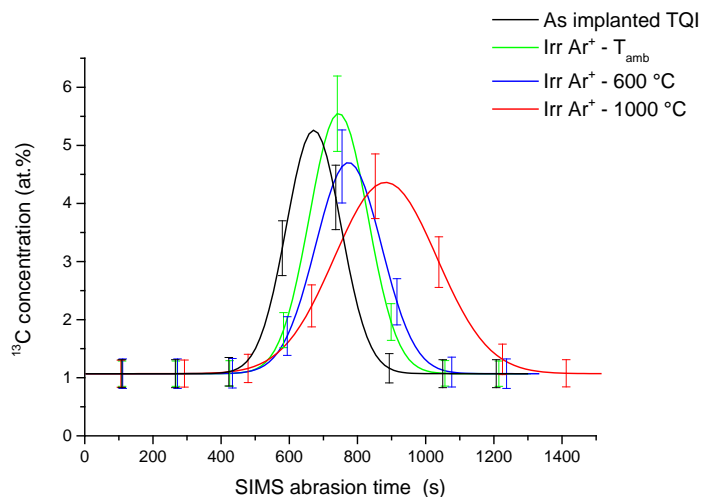
Figure 23: *Comparison of the ^{13}C concentration profiles of the TQI sample and the samples irradiated with 800 keV Ar ions $^{+}$ at ambient temperature (Tamb), 600 °C and 1000 °C as a function of abrasion time during SIMS analysis*

Table 7: *Values for area, full width half maximum (FWHM) and the maxima for the ^{13}C concentration profiles of the samples irradiated with argon ions at different temperatures*

	Area (% at.s)	FWHM (s)	Concentration maximum (s)
TQI	843 ± 29	189 ± 19	672 ± 67
Irr. Ar^{+} - T$_{amb}$	961 ± 31	202 ± 20	745 ± 75
Irr. Ar^{+} - 600 °C	882 ± 30	228 ± 23	774 ± 77
Irr. Ar^{+} - 1000 °C	1243 ± 35	355 ± 36	883 ± 88

Figure 23 and Table 7 show that, within the uncertainties, **^{13}C does not migrate**, with the exception of the profile for the sample irradiated at 1000 °C which broadens, suggesting a possible diffusion of ^{13}C but which we could not quantify.

Irradiation with carbon ions

In Figure 24, the ^{13}C concentration profiles of the samples irradiated with carbon ions at different temperatures are compared with those of the TQI sample. In order to directly compare these

results with those of irradiation with argon ions, we have presented, as previously, the ^{13}C concentration profiles measured by SIMS as a function of abrasion time. Table 8 gives the values for the areas, FWHM and maxima of the concentration profiles.

Figure 24: *Comparison of the ^{13}C concentration profiles for the TQI sample and the samples irradiated with C $^+$ ions of 400 or 600 keV at 200 °C, 600 °C and 1000 °C*

Table 8: *Values for area, full width half maximum (FWHM) and the maxima for the ^{13}C concentration profiles of the samples irradiated with carbon ions at different temperatures*
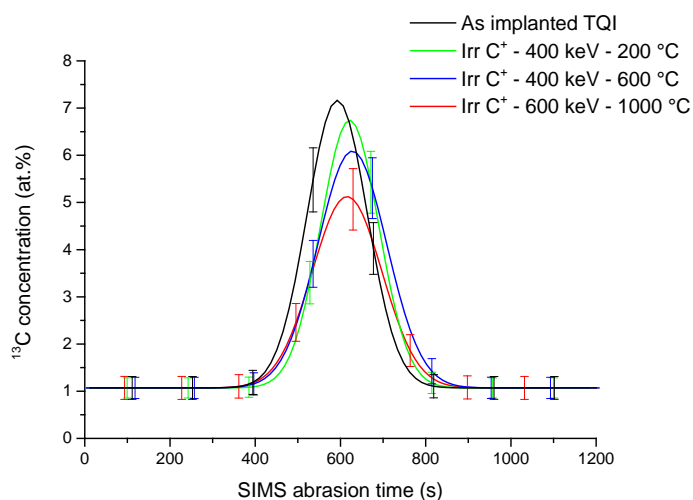
	Area (% at.s)	FWHM (s)	Concentration maximum (s)
TQI	1076 ± 33	166 ± 17	593 ± 59
Irr. C$^+$ - 200 °C	972 ± 31	161 ± 16	622 ± 62
Irr. C$^+$ - 600 °C	1018 ± 32	191 ± 19	628 ± 63
Irr. C$^+$ - 1000 °C	833 ± 29	193 ± 19	616 ± 62

Figure 24 and the values in the table above indicate that within the uncertainties ^{13}C does not migrate.

In conclusion, the results of irradiation with argon or carbon ions show that the ballistic damage does not favour release of ^{13}C for the initially highly disordered samples. Therefore, from the Raman microspectrometry results obtained previously, it seems that ^{13}C is stabilised in sp^2- and sp^3-type structures where the proportion varies according to the irradiation temperature of the graphite.

3.2 | For initially slightly disordered graphite samples

In this section, initial disordering of graphite was realised by implanting [37]Cl at a fluence of 5×10^{13} at.cm^{-2}. This fluence led to about 0.024 dpa of the Rp, i.e. damage of about two orders of magnitude smaller than that generated by implanting with ^{13}C in the previous section.

3.2.1 | Study of the surface by optical microscopy

Figure 25 shows the microscopy images obtained for the samples irradiated with argon ions (image *b*, *c*, and *d*) and carbon ions (*e*) compared to the TQI sample (*a*).
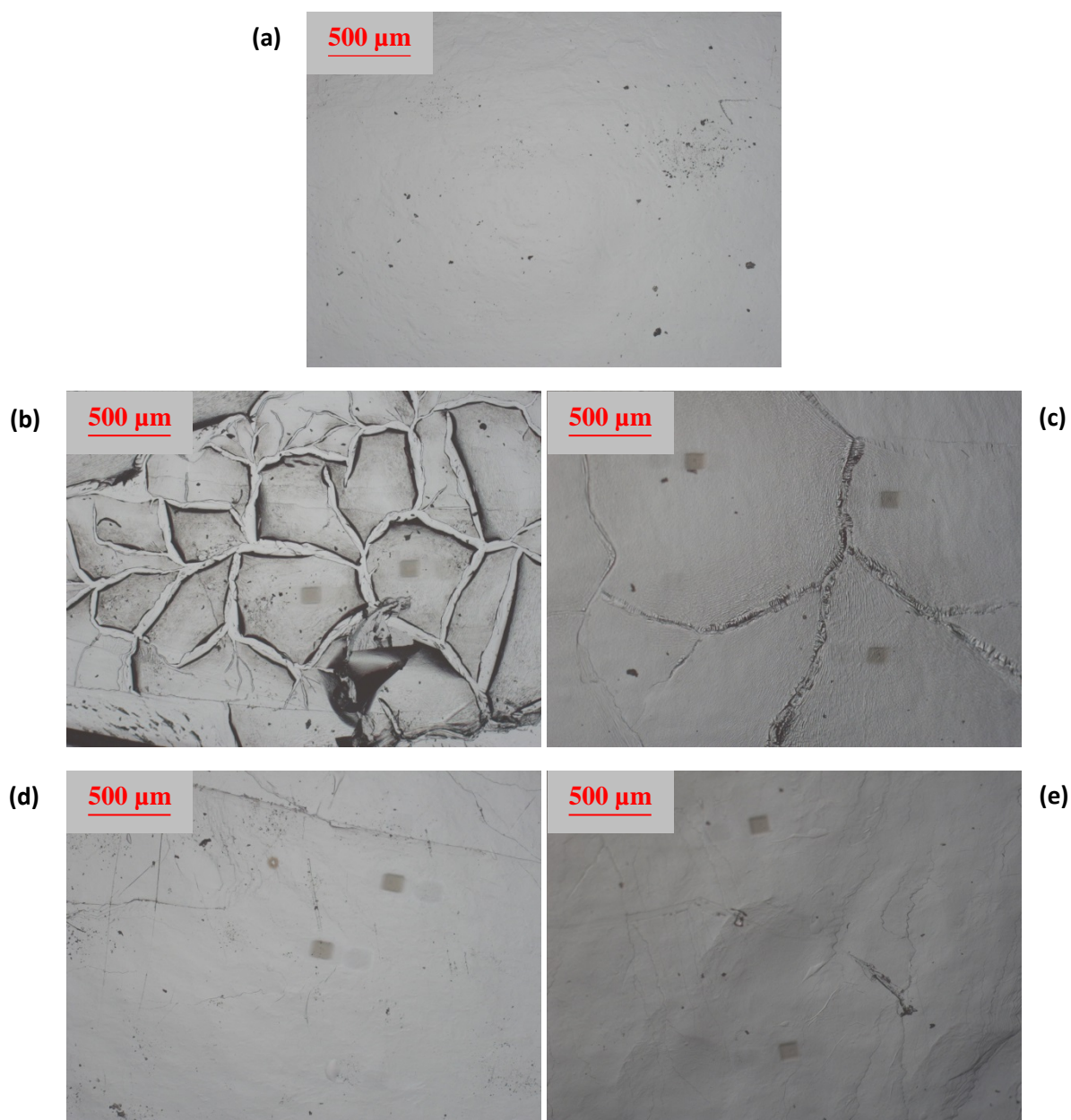
Figure 25: *Optical microscopy images of a TQI sample in ^{37}Cl (a); samples irradiated with argon ions at 200 °C (b), 500 °C (c), 1000 °C (d); and samples irradiated with carbon ions at 200 °C (e)*

The images in Figure 25 show that for irradiation with argon ions, the state of the surface depends greatly on the irradiation temperature. In fact, we go from a fractured state at 200 °C to one which is only slightly cracked at 500 °C. At 1000 °C, the surface is rough but with no apparent fissures. However, for irradiation with carbon ions, the surface is hardly altered, including at 200 °C.

CAST
Report on ^{13}C behaviour under ion irradiation in HOPG
(model graphite) (D5.18)
EURATOM

3.2.2 | Study of the graphite structure by Raman microspectrometry

We remind the reader that irradiation with C^+ ions at an energy of 400 or 600 keV realised at a fluence varying between 5 and 6 x 10^{16} at.cm^{-2} enables about 1 dpa to be obtained in the implanted zone, whereas irradiation with 800 keV Ar$^+$ ions at a fluence of 2 x 10^{16} at.cm^{-2} enables 4.4 dpa to be reached. On Figure 26, we present the Raman spectra obtained for irradiation with carbon ions (Figure 26 *a*) and argon ions (Figure 26 *b*). In addition, Table 9 gives the values of the I_{D1}/I_G ratios for the samples only heated as well as those irradiated with carbon or argon ions at different temperatures.
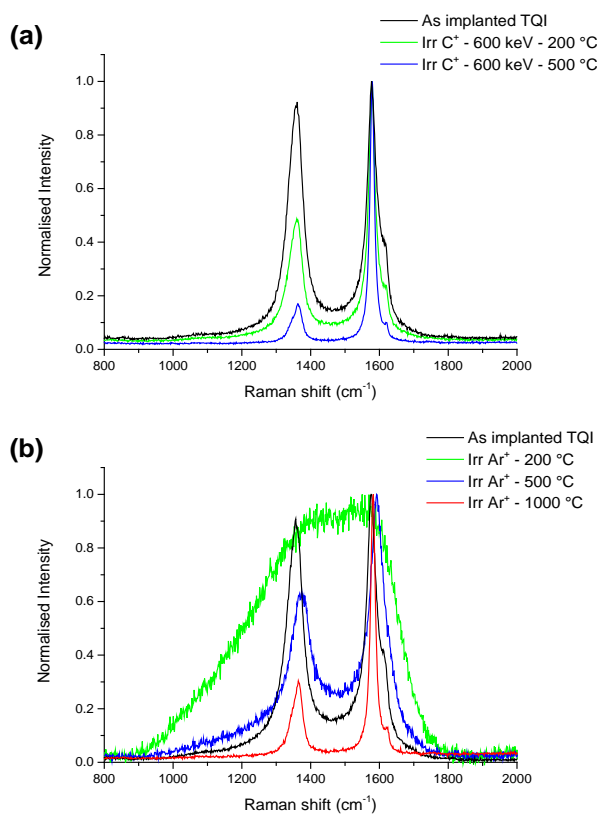
Figure 26: Comparison of the Raman spectrum of a TQI sample with those of samples irradiated with carbon ions (a) or argon ions (b) at different temperatures

Table 9: *Values of the intensity I_{D1}/I_G ratio for the samples only heated or irradiated with carbon or argon ions at different temperatures*

	I_{D1}/I_G		
	Heated only	Irr. C$^+$	Irr. Ar$^+$
TQI	**0.91**	**0.92**	**0.91**
200 °C	0.11	0.49	0.95
500 °C	0.23	0.17	0.64
1000 °C	0.05	-	0.30

For irradiation with carbon ions, the Raman spectra in Figure 26 *a* and the values in Table 9 show that the intensity of the defect band D_1 decreases with temperature. In addition, the bands become narrower indicating a reordering of the graphite. For irradiation with argon ions, irradiation realised at 200 °C disordered the graphite and we observed that the D_1 and G bands broaden considerably and so overlap. The shape of the spectrum shows that the structure tends towards amorphization. However, at 500 °C, the bands become narrower, indicating that the disordering effect of irradiation is completely balanced by the reordering effects of temperature. This phenomenon is even clearer at 1000 °C.

In conclusion, in the case of samples which are initially slightly disordered, irradiation and temperature have antagonistic effects. There therefore seems to be a critical damage value between 1 and 4.4 dpa, above which the temperature (between 200 and 500 °C) is less efficient in reordering the graphite.

3.2.3 | Study of the microstructure of graphite by HRTEM

The graphs in Figure 27 show the values of the inter-layer distances and the angular distributions as a function of depth obtained for a graphite sample previously implanted with ^{37}Cl then irradiated with 600 keV ions C$^+$ in a mainly ballistic regime at 500 °C.

(a)

(b)
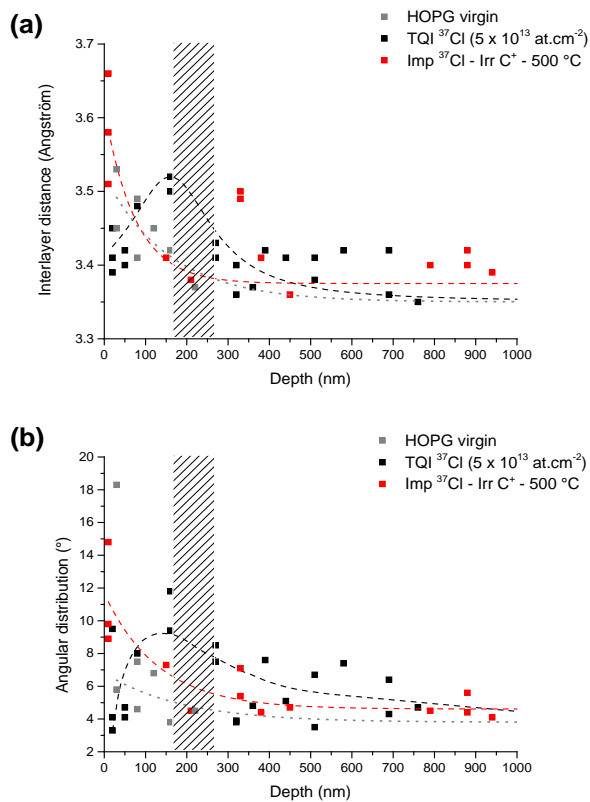
Figure 27: *Inter-layer distance (a) and angular distribution (b) measured on the TEM images at different depths for samples implanted with ^{37}Cl then irradiated. The shaded zone covers the Rp value of the implanted ^{37}Cl and the dashed lines enable the evolution of the values as a function of depth to be followed more clearly*

In comparison to a TQI sample, the values corresponding to a sample irradiated at 500 °C indicate reordering of the graphite where even in the implanted zone they are lower (except on the outer surface). These results corroborate those previously obtained by Raman microspectrometry.

3.3 | Conclusions concerning irradiation effects in a mainly ballistic regime

For all the irradiation experiments, we observed that the effects of irradiation in a mainly ballistic regime are greatly dependent on the initial structure of the graphite. For example, in **very disordered graphite** (about 7 dpa), the combined effects of **temperature and irradiation act in synergy** favouring reordering. Above 250 °C (temperature above which the vacancies and interstitials are mobile), irradiation at an elevated temperature favours the mobilisation and recombination of the pre-existing defects and of those introduced by irradiation thus enabling a progressive reordering of the structure.

However, in **graphite which is only slightly disordered** (<< 0.1 dpa), **irradiation and temperature have an antagonistic effect**. The possibility of reordering the graphite is in this case

strongly dependent on the temperature and the degree of damage. All in all, if there is a high degree of damage (about 4 dpa) and a low temperature (less than 200 °C), there will only be a poor reordering of the graphite. There is therefore a competitive effect between the irradiation and temperature with a critical damage value of between 1 and 4.4 dpa, above which the temperature (between 200 and 500 °C) is less efficient in reordering the graphite.

In both the above cases, **the ^{13}C is stabilised** in the sp^2- and sp^3-type structures where the proportion varies according to the irradiation temperature of the graphite.

4 | Effect of irradiation in a mainly electronic regime

The next part of the study concerned the effects of irradiation in a mainly electronic regime using the same procedure as above. The irradiation was done with 15.7 MeV helium ions, 100 MeV sulphur ions and 200 MeV iodine ions which enabled the electronic stopping power of 75, 3700 and 16700 keV/µm to be reached, respectively.

4.1 | For the initially very disordered graphite samples

4.1.1 | S_e lower than the track creation threshold (S_e = 3700 keV/µm)

The irradiation for this study was done with 100 MeV sulphur ions at ambient temperature and at 500 and 1000 °C. In these conditions, the electronic stopping power is 3700 keV/µm in the implanted zone. This value is higher than those encountered in a working UNGG reactor but it is lower than the theoretical threshold of track creation in HOPG graphite.

Surface state

The surface of the irradiated samples was observed by SEM. The SEM images are given in Figure 28 and are compared with that of the TQI sample.

(a)

(b)

(c)
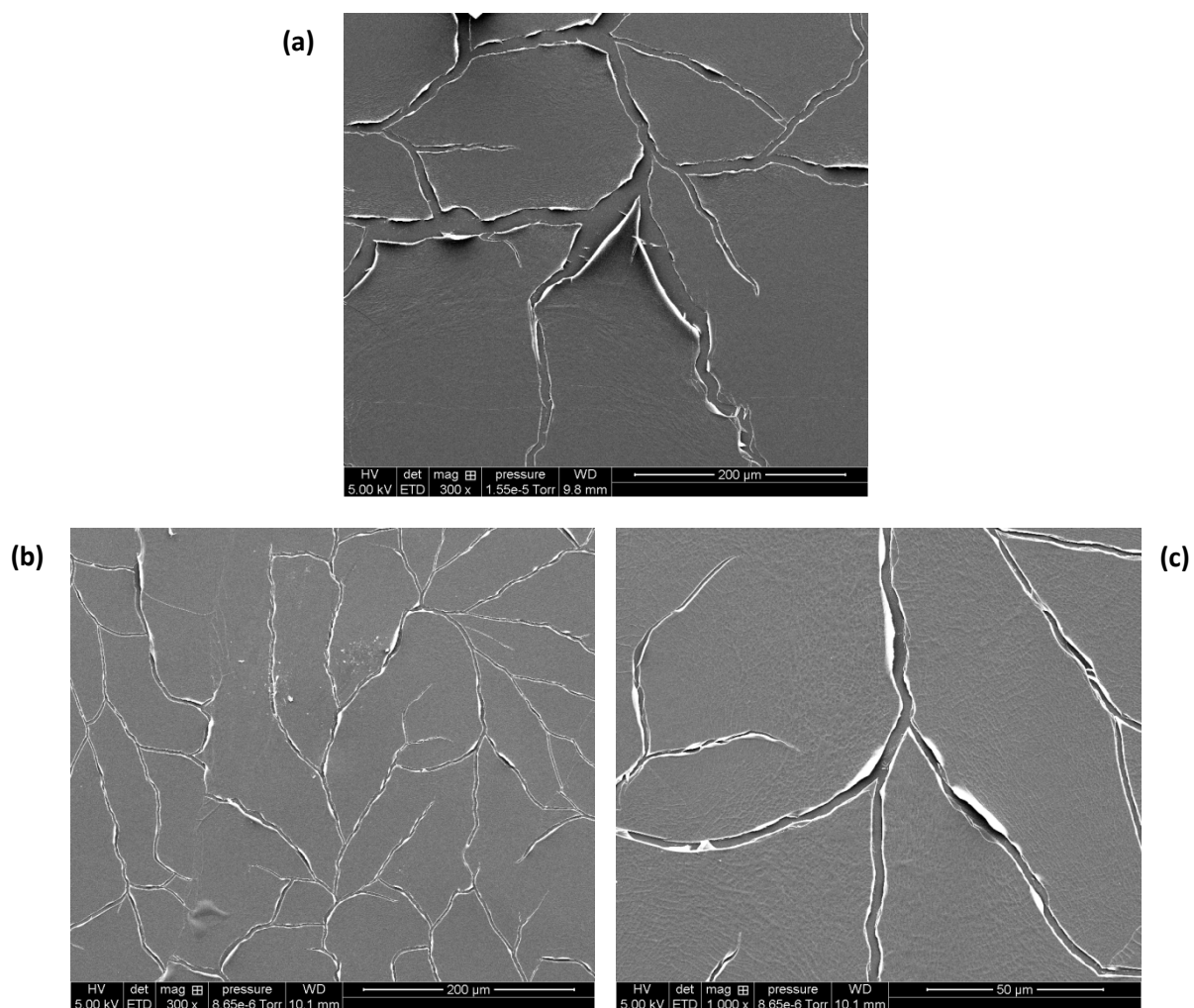
Figure 28 : *Observation by SEM of (a) the surface state of a TQI sample in ^{13}C and (b + c) a sample implanted then irradiated with 100 MeV sulphur ions at 1000 °C*

On the above magnification, we can see that the surface of the irradiated sample is similar to that of the TQI sample. Therefore, contrary to irradiation in a ballistic regime, irradiation in a highly electronic regime has only a slight impact on the state of the surface.

<u>Structural state of the graphite</u>

The structural state of the graphite was observed by Raman microspectrometry. Figure 29 shows the Raman spectra obtained for the samples irradiated with 100 MeV sulphur ions at different temperatures. Table 10 gathers the values of the I_{D1}/I_G intensity ratio as a function of irradiation temperature.
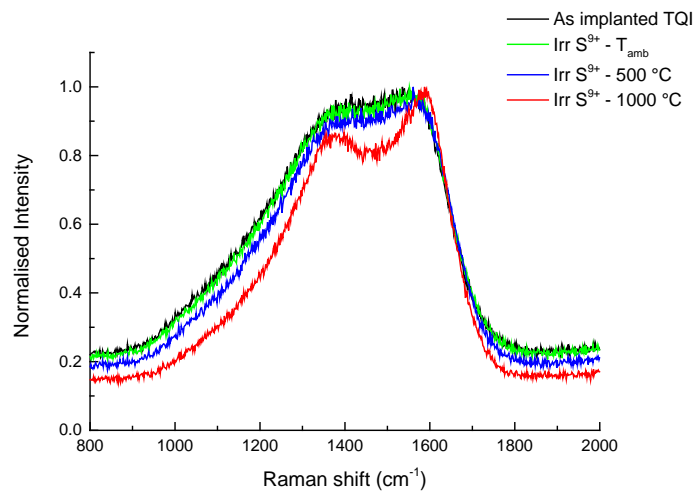
Figure 29: *Comparison of the Raman spectrum of the TQI sample with the spectra of samples irradiated with sulphur ions at different temperatures*

Table 10: *Values of the I_{D1}/I_G intensity ratio for samples only heated or irradiated with sulphur ions at different temperatures*

	I_{D1}/I_G	
	Heated only	Irr. S^{9+}
TQI	**0.94**	**0.96**
T_{amb}	-	0.94
500 °C	-	0.89
1000 °C	0.88	0.86

Figure 29 shows that for this irradiation, there is almost no reordering of the graphite at 500 °C and only slightly at 1000 °C. In fact, the D_1 and G bands only begin to separate at 1000 °C. As can be observed in Table 10, the reordering of the graphite is slightly more than that observed for the sample which has only been heated at 1000 °C (section 2.1.1). Contrary to the results obtained in a ballistic regime, the combined effects of irradiation and temperature in an electronic regime only lead to a slight reordering of the graphite, even at 1000 °C. On the atomic scale, the larger proportion of sp^3 carbons produced at the time of implantation decreases very slightly or not at all.

<u>Microstructural study of graphite by TEM</u>

To study the disordering of the graphite, we used TEM. The graphs in Figure 30 show the values for the inter-layer distances and the angular distribution measured on the graphite samples initially implanted with ^{13}C at 6 x 10^{16} at.cm^{-2} then irradiated with S[9+] ions at 1000 °C. These values are compared with those for the TQI graphite. In these conditions, the sulphur ions stop at a depth of about 24 µm. Unfortunately, the thin sections used here meant we were unable to make observations at such a depth. We probed depths only up to 1 µm.
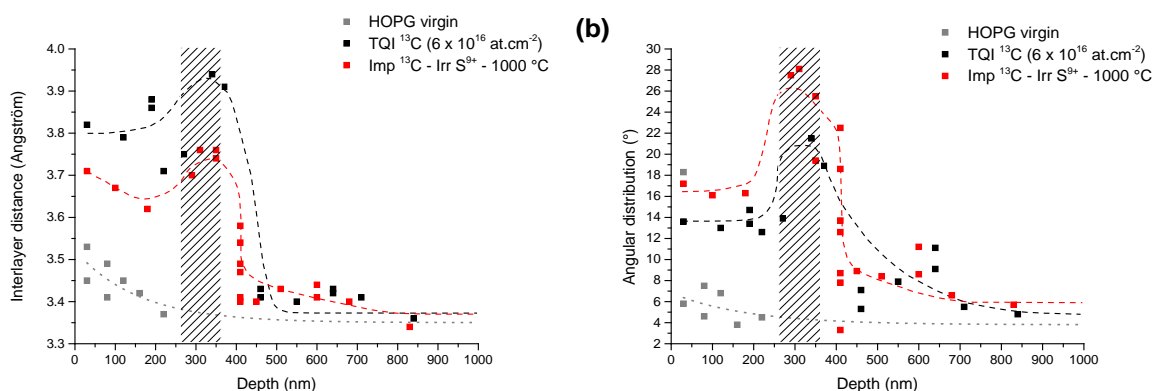
Figure 30: *(a) inter-layer distance and (b) angular distribution measured on the TEM images at different depths for the samples implanted with ^{13}C at high fluence then irradiated with 100 MeV sulphur ions. The shaded zone covers the Rp value of the implanted ^{13}C and the dashed lines enable the trends in the evolution of these values as a function of depth to be seen more clearly*

Figure 30 ***a*** shows that the inter-layer distances measured for the samples irradiated at 1000 °C are less than the TQI sample in the implanted zone. This indicates restructuring of the graphite the same as that observed by Raman microspectrometry. However, the angular distribution values for the layers do not indicate reordering in the implanted zone. Therefore, the reordering process could be similar to the model suggested by Rouzaud et al. in 1983 [Rouzaud 1983]. In this article, the authors show that the graphitisation process occurs in successive steps. Below 1200 °C, the basic structural units (BSU's) associate to form deformed columns then, above 1200 °C, these columns coalesce to form planes, which are wrinkled/ridged and deformed. In our case, at 1000 °C, it is likely that the layers associate to form stacks which remain disordered with respect to each other.

<u>Migration behaviour of ^{13}C in graphite</u>

Figure 31 shows the ^{13}C concentration profiles as a function of irradiation temperature compared to the ^{13}C profile for the TQI sample. Table 11 contains the area, FWHM and the Rp value for each profile.

Figure 31: *Comparison of the ^{13}C concentration profiles for the TQI sample and the samples irradiated with 100 MeV S^{9+} ions at different temperatures*
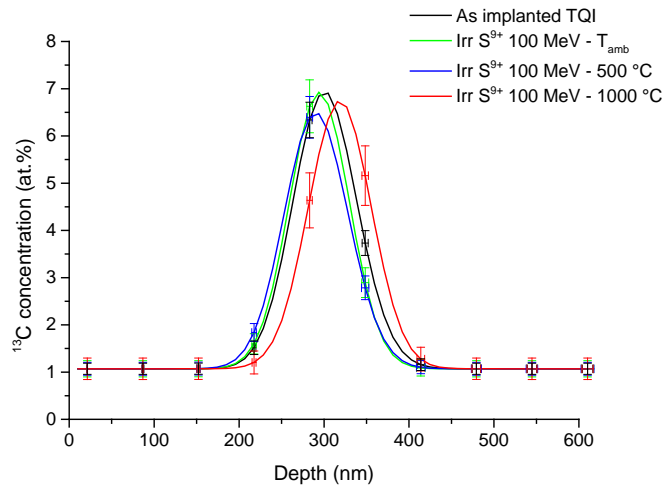
Table 11: *Area, FWHM and Rp values for the ^{13}C concentration profiles for the samples irradiated with sulphur ions at different temperatures*

	Area (% at.nm)	FWHM (nm)	Rp (nm)
TQI	552 ± 23	89 ± 9	302 ± 3
Irr. S^{9+} - T_{amb}	517 ± 23	83 ± 8	295 ± 3
Irr. S^{9+} - 500 °C	512 ± 23	89 ± 9	291 ± 4
Irr. S^{9+} - 1000 °C	525 ± 23	87 ± 9	319 ± 3

The profiles and values given in the table above show that, whatever the irradiation temperature, ^{13}C does not migrate.

4.1.2 | S_e greater than the track creation threshold (S_e = 16700 keV/µm)

We also used 200 MeV iodine ions. In these conditions, the electronic stopping power is 16700 keV/µm in the implanted zone. This S_e is much higher than that calculated for the working UNGG reactors and it is also higher than the threshold estimated for track formation in HOPG graphite. Irradiation was done at two temperatures, i.e. ambient temperature and 1000 °C.

Structural state

Figure 32 shows the Raman spectra obtained for the samples irradiated with 200 MeV iodine ions at different temperatures compared to the spectrum for the TQI sample. Table 12 gathers the I_{D1}/I_G intensity ratio values as a function of irradiation temperature.
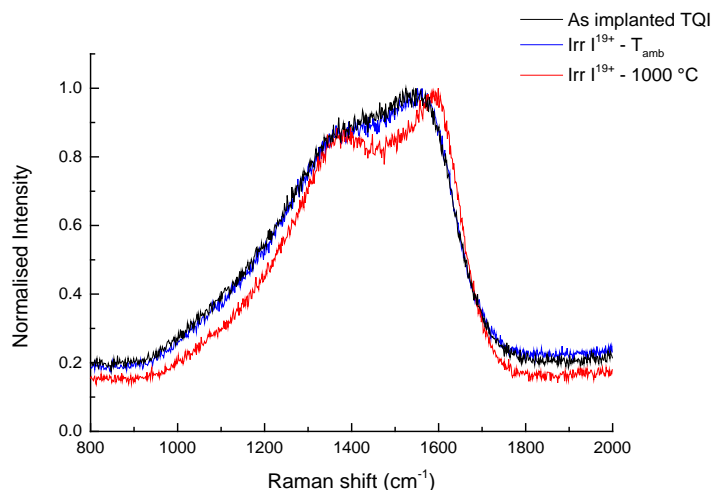
Figure 32: *Comparison of the Raman spectrum for a TQI sample with the spectra for samples irradiated with iodine ions at different temperatures*

Table 12: *I_{D1}/I_G intensity ratio values for the samples only heated and those irradiated with iodine ions at different temperatures*

	I_{D1}/I_G	
	Heated only	Irr. I^{19+}
TQI	**0.94**	**0.89**
T_{amb}	-	0.87
1000 °C	0.88	0.88

The above Figure and values in the table show that for irradiation at a high electronic stopping power (16700 keV/µm), which is above the track creation threshold in HOPG graphite for 200 MeV iodine ions, the reordering of the graphite is very slight, even at 1000 °C. In fact, the D_1 and G bands are only just beginning to separate. The reordering of graphite is of the same order as that previously observed for a sample only heated at 1000 °C (section 2.1.1).

Migration behaviour of ^{13}C in graphite

Figure 33 shows the ^{13}C concentration profiles as a function of irradiation temperature compared to the ^{13}C profiles in a TQI sample. Table 13 gathers the area, FWHM and Rp values for these profiles.
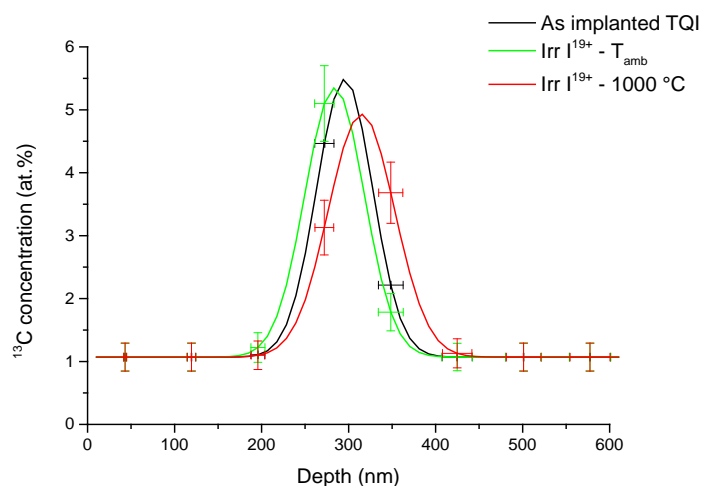
Figure 33: *Comparison of the ^{13}C concentration profiles of the TQI sample and the samples irradiated with 200 MeV I^{19+} ions at ambient temperature and 1000 °C*

Table 13: *Area, FWHM and Rp values for the ^{13}C concentration profiles for the samples irradiated with iodine ions at different temperatures*

	Area (% at.nm)	FWHM (nm)	Rp (nm)
TQI	357 ± 19	76 ± 8	295 ± 12
Irr. I^{19+} - T_{amb}	366 ± 19	80 ± 8	284 ± 12
Irr. I^{19+} - 1000 °C	368 ± 19	90 ± 9	315 ± 13

In the above case, we also observe that the Figure and values in the table reveal that the ^{13}C concentration profiles in irradiated graphite remain unchanged (within the precision limits of the analysis) and this therefore shows structural stabilisation.

In conclusion, with irradiation in a mainly electronic regime done at high Se values, greater than those encountered in UNGG reactors, the graphite reorders only very slightly, even at 1000 °C, contrary to our observations for irradiation in a ballistic regime. The implanted ^{13}C is stabilised in the graphite but mostly in sp^3-type structures.

4.1.3 | S_e in the same order of magnitude as in a reactor (S_e = 75 keV/µm)

This irradiation was done with 15.7 MeV He$^+$ ions. In these conditions, the electronic stopping power is 75 keV/µm in the implanted zone. It is therefore within the range of the S_e values in UNGG reactors which in most cases does not go above 700 keV/µm. Our objective was to get close to the UNGG reactor working conditions, and so we irradiated the graphite samples while heating them at 500 °C and also putting them in contact with a gas simulating the coolant gas of UNGG reactors. For this irradiation, we used the cell shown in section 1.2.2 which enables the structural modifications to be followed on line by *in situ* Raman microspectrometry. We irradiated a sample with helium ions at a current of 40 nA corresponding to a flux of 1 x 10^{12} at.cm^{-2}.s^{-1}, at a fluence of 1 x 10^{16} at.cm^{-2}. Figure 34 *a* shows the spectra obtained by Raman microspectrometry at the start and end of the irradiation and Figure 34 *b* shows the evolution of the I_{D1}/I_G intensity ratios during the irradiation.
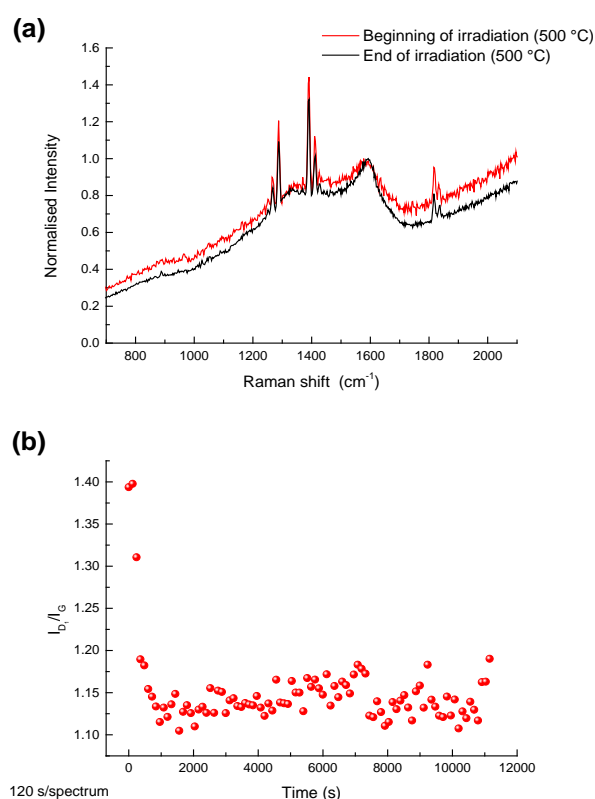
Figure 34: *(a) Raman spectra recorded at the beginning and end of irradiation, and (b) the evolution of the I_{D1}/I_G intensity ratio during irradiation with 15.7 MeV He$^+$ ions at 500 °C in the presence of UNGG gas (1 x 10^{16} at.cm^{-2})*

From Figure 34, we first observe that the Raman spectra recorded at the beginning and end of irradiation are very similar. We can identify four bands which can be attributed to the gas (two at about 1280 cm^{-1} and two at about 1400 cm^{-1}). They are either side of the defect band D_1. The G band is quite broad and is at 1590 cm^{-1}. The vibration bands of the gas are still present but do not interfere

with the analysis. If we look at the graph representing the evolution of the I_{D1}/I_G intensity ratio as a function of time, we first observe that the initial value of this ratio is almost 1.4, which is very high. This means that the band D_1 is more intense than the band G, indicating that the graphite is very disordered. However, the effect of irradiation is then to decrease this ratio which stabilises at about 1.15 indicating a structural reordering of the graphite during irradiation at higher temperatures. However, the intensity ratio of the bands remains greater than 1, which means that the defects induced by the implanting process are so significant that they completely mask the effects of irradiation. It is for this reason that virgin or slightly disordered samples will be used for the following study in these irradiation conditions (section 4.2.3).

4.2 | For initially slightly disordered graphite samples

The samples used in the following experiments were irradiated in the same conditions as the initially very disordered ones, the results of which are presented in the previous section (4.1).

4.2.1 | S_e less than the track creation threshold

Structural state of the graphite

The spectra obtained by Raman microspectrometry for the samples irradiated with 100 MeV sulphur ions at different temperatures are given in Figure 35. The values of the I_{D1}/I_G intensity ratio for these spectra are given in Table 14 and compared with those obtained for the samples which were only heated.
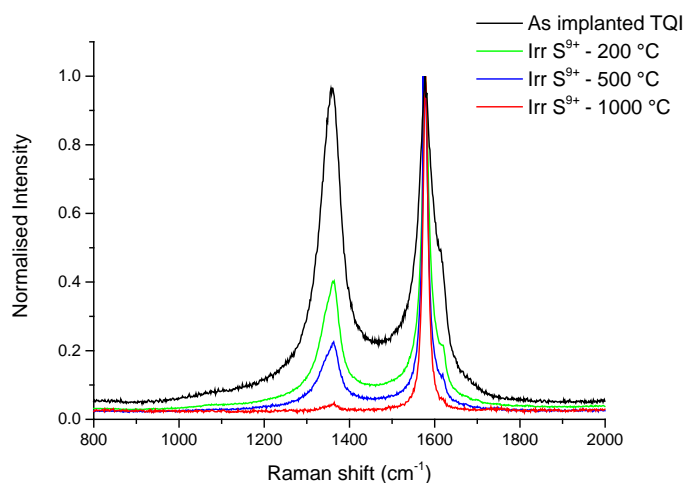
Figure 35: *Comparison of the Raman spectrum of a TQI sample with the spectra of samples irradiated with sulphur ions at different temperatures*

Table 14: *I_{D1}/I_G intensity ratio values for the samples only heated or irradiated with sulphur ions at different temperatures*

	I_{D1}/I_G	
	Heated only	Irr. S^{9+}
TQI	**0.91**	**0.97**
200 °C	0.11	0.4
500 °C	0.23	0.23
1000 °C	0.05	0.05

As can be seen from the above results for irradiation at higher temperatures, the intensity of band D_1 decreases and bands D_1 and G become narrower indicating the progressive reordering of the graphite. However, the values of the I_{D1}/I_G intensity ratio in Table 14 show that at 200 °C, the reordering is less than the effect of temperature (heating) alone. This is not the case at 500 and 1000 °C as the reordering is the same for both the irradiated sample and the one which was only heated.

Microstructural study of graphite by TEM

We also observed samples irradiated with 100 MeV sulphur ions at 500 °C by TEM. As previously, the graphs in Figure 36 show the values of the inter-layer distance and angular distribution compared to those of a TQI sample. Comparison of these values indicate a reordering of the implanted zone, and are thus in agreement with the measurements realised by Raman microspectrometry.
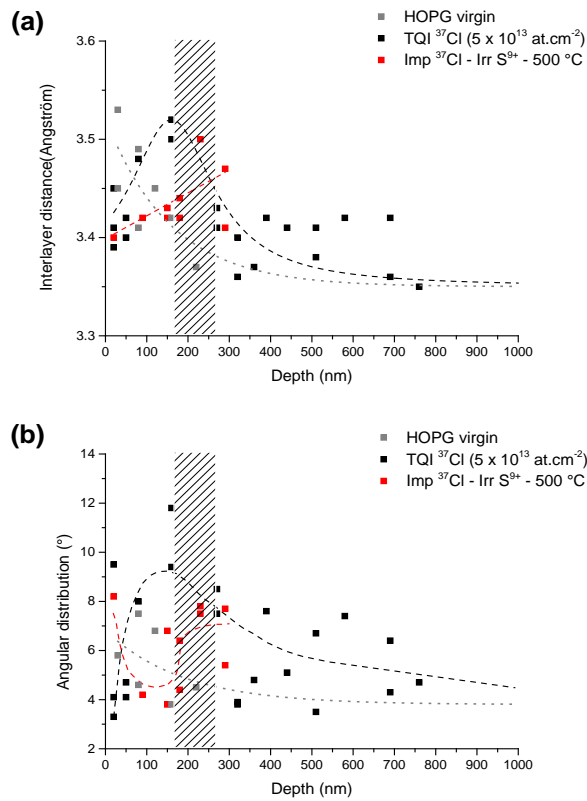
Figure 36: *Inter-layer distance and angular distribution measured on the TEM images at different depths for samples implanted with ³⁷Cl then irradiated. The shaded zone covers the Rp value of the implanted ³⁷Cl and the dashed lines enable the trends in the evolution of these values as a function of depth to be seen more clearly.*

4.2.2 | S_e greater than the track creation threshold (S_e = 16700 keV/µm)

Structural state of the graphite

The spectra obtained by Raman microspectrometry for the samples irradiated with 200 MeV iodine ions at different temperatures (200 and 1000 °C) are given in Figure 37. The values of the I_{D1}/I_G intensity ratio corresponding to these spectra are given in Table 15 and compared with those obtained for samples which were only heated.
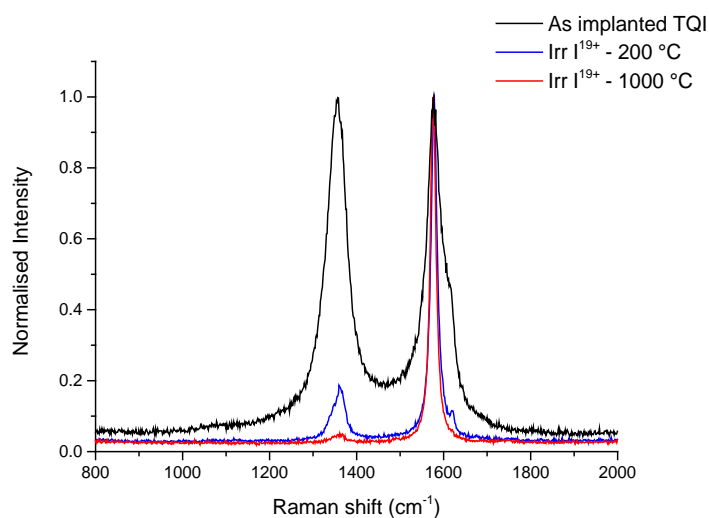
Figure 37: Comparison of the Raman spectrum for a TQI sample with the spectra of samples irradiated with iodine ions at different temperatures

Table 15: Values of the I_{D1}/I_G intensity ratio for the samples only heated or those irradiated with iodine ions at different temperatures

	I_{D1}/I_G	
	Heated only	Irr. I^{19+}
TQI	**0.91**	**1**
200 °C	0.11	0.19
1000 °C	0.05	0.05

As for the findings obtained above, these results show that during irradiation at higher temperatures, the intensity of band D_1 decreases and bands D_1 and G narrow indicating progressive reordering of the graphite. However, the values of the intensity ratios in tables 14 and 15 indicate that at 200 °C, there is slightly more reordering than during irradiation with sulphur ions but not as much as when the sample is only heated. At 1000 °C, the reordering is again the same as that for the only heated sample.

In conclusion, for irradiation in a mainly electronic regime done at a high Se, greater than the values observed in UNGG reactors, there is a progressive reordering in the samples irradiated at higher temperatures but this is less efficient than when the sample is only heated. This indicates an antagonistic effect between irradiation and temperature.

4.2.3 | S_e in the same order of magnitude as in a reactor (S_e = 75 keV/μm)

In the previous sections concerning irradiation with sulphur and iodine ions, we have seen that in a mainly electronic regime the structure of the graphite could be damaged. However, we must not ignore the hypothesis that part of the damage may also be linked to the ballistic effect even if the latter is relatively small (table 2). Consequently, irradiation with helium ions should allow us to better understand the effect of electronic damage within the limits where the S_n/S_e ratio in the implanted zone for irradiation with helium ions is 1 to 3 orders of magnitude lower than those for irradiation with sulphur and iodine ions, respectively (table 2). Therefore in the following sections, we will study in more depth the effects of irradiation with helium ions on virgin or slightly disordered samples (implanted with ^{13}C at a fluence of 4 x 10^{14} at.cm^{-2} or with ^{37}Cl at a fluence of 5 x 10^{13} at.cm^{-2}).
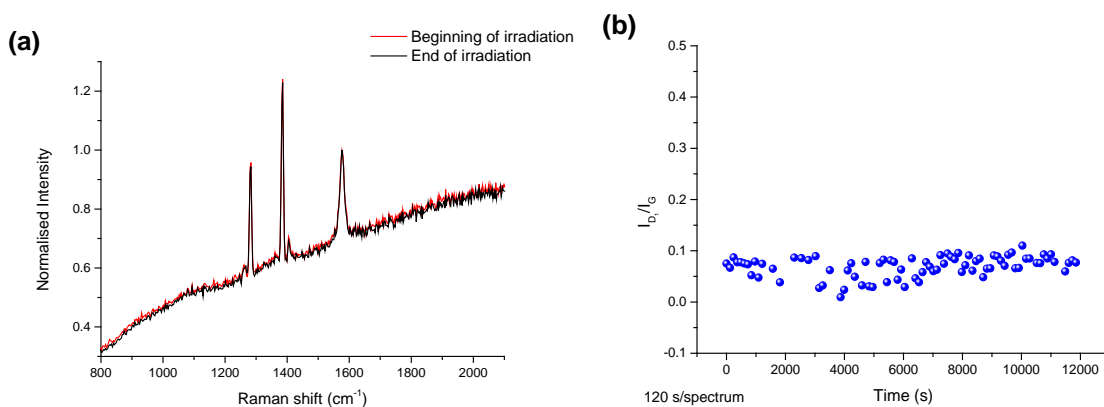
Irradiation was done with 15.7 MeV He$^+$ ions. The electronic stopping power is 75 keV/μm in the implanted zone. The irradiation was mostly done at a current of 40 nA, corresponding to a flux of 1 x 10^{12} ions.cm^{-2}.s^{-1}, with a fluence of 1 x 10^{16} ions.cm^{-2}. With the objective of testing the influence of flux and fluence, some irradiation was done with a current of 80 nA, corresponding to a flux of 2 x 10^{12} ions.cm^{-2}.s^{-1}, with a fluence of 2 x 10^{16} ions.cm^{-2}. The samples, put in contact with a gas simulating the coolant gas of the UNGG reactors (section 1.2.2), were irradiated at ambient temperature or 250 °C or 500 °C and were studied using *in situ* Raman microspectrometry. In addition, in order to understand the effects of the structural modifications associated with the variations in temperature alone, the Raman signal was recorded in certain cases before starting the irradiation, during the rise in temperature of the sample and at the end of the irradiation during the drop in temperature. The heating and cooling temperature ramps were about 10°C/min (i.e. a time of 50 minutes for irradiation at 500 °C).

A | Virgin HOPG graphite

Study of the microstructural state by Raman microspectrometry during irradiation

We began by irradiating a virgin HOPG sample (non-implanted) which had no structural defects before irradiation. Figure 38 *a* gives the spectra obtained by Raman microspectrometry on this sample (at the start of irradiation) and on the same one at the end of irradiation. From this Figure, we can see that there is only a single band G which is narrow and intense but that no defect band is observed (neither D$_1$ nor D$_2$).

Three virgin HOPG samples were irradiated in different conditions: one at ambient temperature with a fluence of 1 x 10^{16} ions.cm^{-2}, another at the same fluence at 500 °C and the last at ambient temperature but at a fluence of 2 x 10^{16} ions.cm^{-2} (the intensity of the irradiation current was doubled over the same irradiation period with the view to doubling the flux and fluence). Figure 38 *b* shows the variation in the I_{D1}/I_G ratio as a function of time measured during irradiation at ambient temperature and a fluence of 2 x 10^{16} at.cm^{-2}.

Figure 38 : *(a) Spectra recorded by Raman microspectrometry at the beginning and end of irradiation and (b) the evolution of the I_{D1}/I_G intensity ratio during irradiation with 15.7 MeV He$^+$ ions at ambient temperature in the presence of UNGG gas (2 x 10^{16} at.cm^{-2})*

We observe that for all three irradiation conditions, the evolution of the I_{D1}/I_G intensity ratio is similar and constant and the value is very low, less than 0.1, in the background noise. Therefore, we have chosen to only present one of them. On the Raman signal, there is no defect band D$_1$ even at ambient temperature when the flux and fluence of the irradiation are doubled.

Study of the microstructural state by Raman microspectrometry and TEM after irradiation

Figure 39 ***a*** gives the spectra obtained by Raman microspectrometry on a sample irradiated at 500 °C at a fluence of 1x10^{16} at.cm^{-2}. The analysis was done after irradiation, i.e. no presence of gas and with a longer measurement time. This Figure shows the appearance of the defect band D$_1$ with a low intensity (I_{D1}/I_G is about 0.04) compared to irradiation of the TQI sample. This band could not be observed during the *in situ* analysis probably because it was masked by a significant luminescence which resulted in an increase in the background noise as a function of the Raman shift. Figures 39 ***b*** and ***c*** show the evolution of the inter-layer distance and the angular distribution obtained by TEM for two irradiated samples (one at 500 °C, simple flux and simple fluence and the other at ambient temperature, but with double the flux and double the fluence) and a virgin graphite sample.
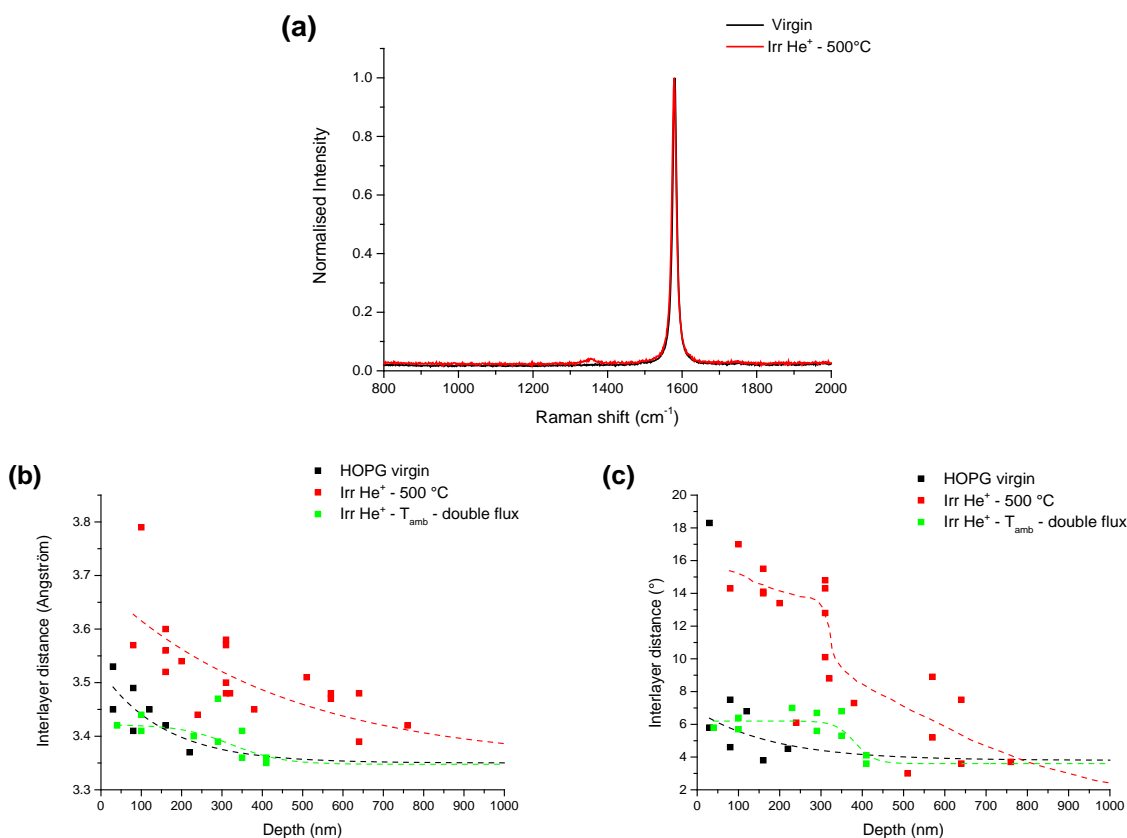
Figure 39: *(a) Raman spectra of the virgin and irradiated HOPG samples with He⁺ ions; (b) and (c) Inter-layer distance and angular distribution measured on the TEM images at different depths for the virgin and irradiated samples. The dashed lines enable the trends in the evolution of these values as a function of depth to be seen more clearly.*

The results in Figure 39 show that the values measured for a sample irradiated at double the flux are comparable to those of the virgin sample whereas the values for the irradiated sample at 500 °C and a fluence of 1 x 10^{16} at.cm^{-2} are greater on the surface but also over the depth. We therefore conjecture that the sample was already disordered before irradiation perhaps by the process of removal of the first layers that we do systematically in order to obtain a cleaner surface. Indeed, this fact has already been observed by the carbon specialist J.N. Rouzaud, (private communication).

In conclusion, it seems that irradiation with helium ions at a low electronic stopping power can lead to slight disordering as much at ambient temperature as at 500 °C.

We observed a brown-coloured deposit in the irradiated zone of the sample irradiated at a fluence of 1 x 10^{16} at.cm^{-2} at ambient temperature in the presence of UNGG gas. This deposit, spots in certain places, was observed by SEM and the images are given in Figure 40. To obtain information on the composition of this deposit and the spots, a sample was analysed by XPS (X-ray Photoelectron

Spectroscopy) in the Science and Surface Laboratory. This technique enables a semi-quantitative analysis of the elements detected. The results of these analyses are given in Table 16.
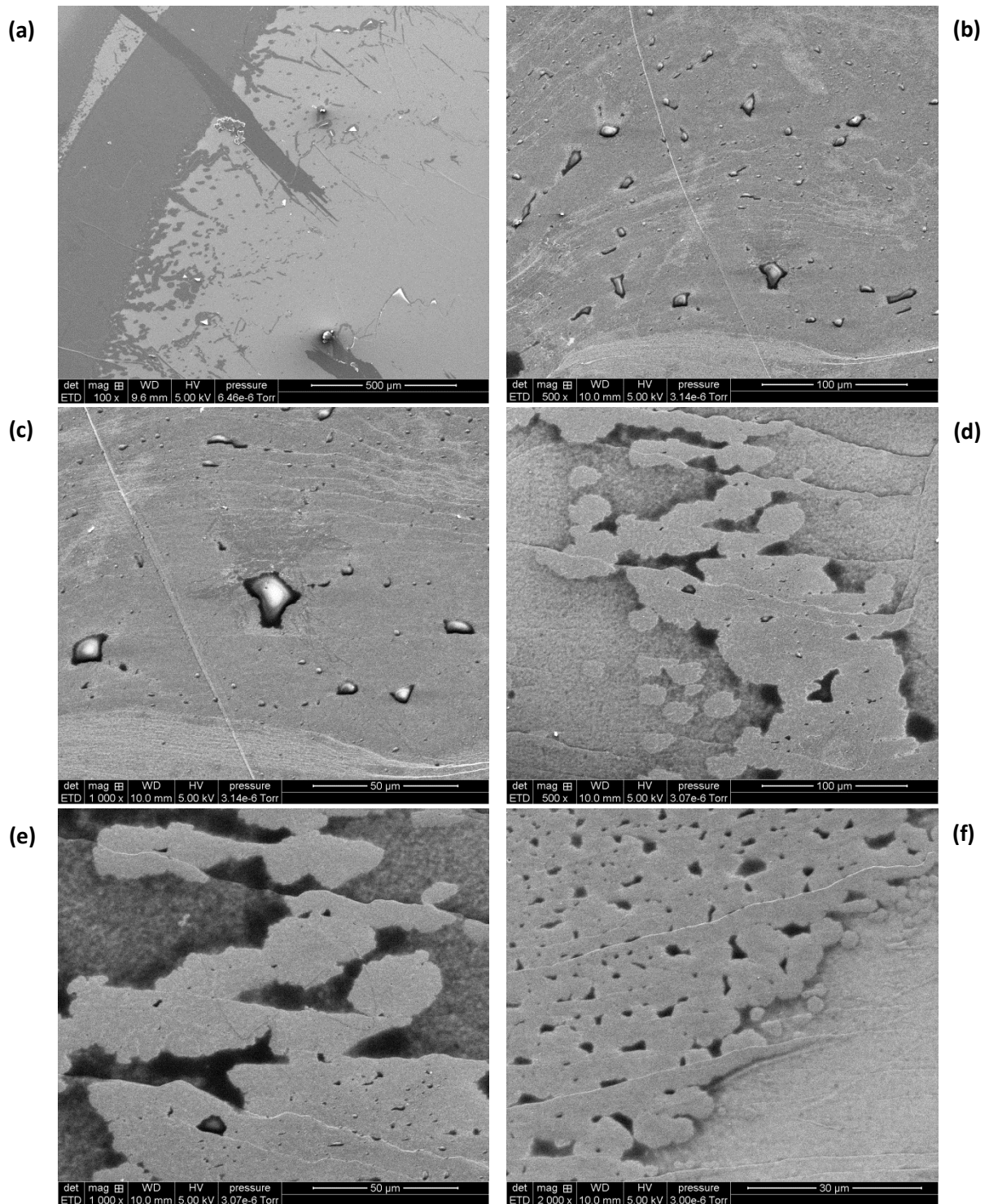
Figure 40: *SEM images of the sample surface analysed by XPS. The deposits appear in white grey colour and the spots in white.*

Table 16: *Atomic composition (%) measured by XPS of the different zones of a reference HOPG and an irradiated HOPG*

Sample	Zone	Size of the zone analysed	C	O	Si	O/C
Reference HOPG	Centre of the sample	200 µm	94.4	4.1	1.5	0.04
Irradiated HOPG	Deposit		87.6	10.3	2.1	0.12
	spot	20 µm	80.0	17.3	2.7	0.22
	Outside the deposit		89.2	9.1	1.7	0.10
	Spot	10 µm	63.5	34.6	1.9	0.54
	Outside the deposit		86.4	11.0	2.6	0.13

The above results show that the deposit and especially the spots are enriched in oxygen compared to the non-irradiated reference HOPG sample. The deposit and spots are also enriched in silicon and it is possible that this Si could have catalysed the formation of these deposits. Si pollution on the sample surface could have come from degradation of the silica tube used for heating and degassing during the sample preparation. These deposits might correspond to carboxide deposits which formation is favoured by the presence of a catalyst (often metallic in nature) as observed in a UNGG reactor by some authors [Wright 1980, Baird 1980, Faircloth 1980].

<u>Irradiation at ambient temperature under vacuum</u>

In order to eliminate the effects of the gas, we irradiated at ambient temperature but under a dynamic primary vacuum ($\approx$ 2.5 x 10^{-2} mbar) and up to a fluence of 1 x 10^{16} at.cm^{-2}. In these conditions, the ion beam no longer passes through the gas and therefore reaches the surface of the sample with an energy of 22.1 MeV. The electronic stopping power in the implanted zone is about 58 keV/µm and this irradiation induces about 8.5 x 10^{-6} dpa. It is important to point out that under the effect of irradiation, the temperature in the irradiation cell increased from 23 to 65 °C. The Raman microspectrometry spectra recorded at the beginning and end of irradiation are given in Figure 41 ***a*** and the evolution of the I_{D1}/I_G intensity ratio during the irradiation in Figure 41 ***b***.
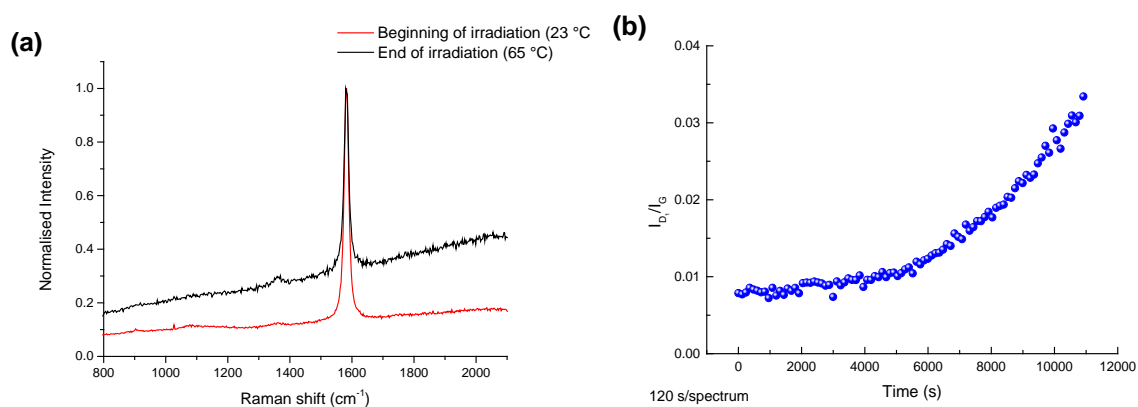
Figure 41: *Evolution of the I_{D1}/I_G intensity ratio during the period of irradiation with 22.1 MeV He$^+$ ions at ambient temperature and under dynamic vacuum (1 x 10^{16} at.cm^{-2})*

Figure 41 shows that the I_{D1}/I_G intensity ratio increases with the irradiation fluence. This means that the defect band D_1 can be seen and it also increases in intensity with the fluence. However, this increase is relatively low as the I_{D1}/I_G ratio increases from about 0.01 to 0.035. This value is comparable with that observed previously during the *ex situ* measurement made at the end of irradiation and is given in Figure 39.

B | Initially slightly disordered graphite

Structural state of the graphite

Irradiation was done on samples previously implanted with ^{13}C at a fluence of 4x10^{14} at.cm^{-2} or with ^{37}Cl at a fluence of 5x10^{13} at.cm^{-2}. The Raman spectra of the TQI samples are given in Figure 42.
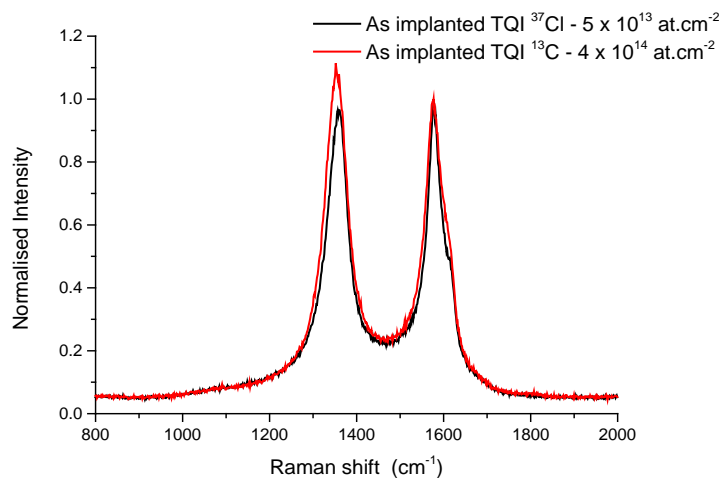
Figure 42: *Raman spectra of the TQI samples implanted with ^{37}Cl at a fluence of 5×10^{13} at.cm^{-2} and with ^{13}C at a fluence of 4×10^{14} at.cm^{-2} obtained using a laser at a wavelength of 514 nm*

The two spectra in Figure 42 can almost be superimposed. This means that the structural state of the graphite in the implanted zone is also comparable. As the irradiation results are similar, we chose, in most cases, only those coming from the implanting of ^{13}C.

<u>Role of temperature</u>

The irradiation was done at 250 and 500 °C. The results obtained are given in Figures 43 and 44, respectively. On both Figures, (**a**) is for the spectra that were recorded at different stages of the experiment; (**b**) is the evolution of the position of band G; (**c**) is the I_{D1}/I_G intensity ratio as the temperature is increased up to 250°C; (**d**) and (**e**) are the evolution of the position of band G and the I_{D1}/I_G intensity ratio during irradiation, respectively

.
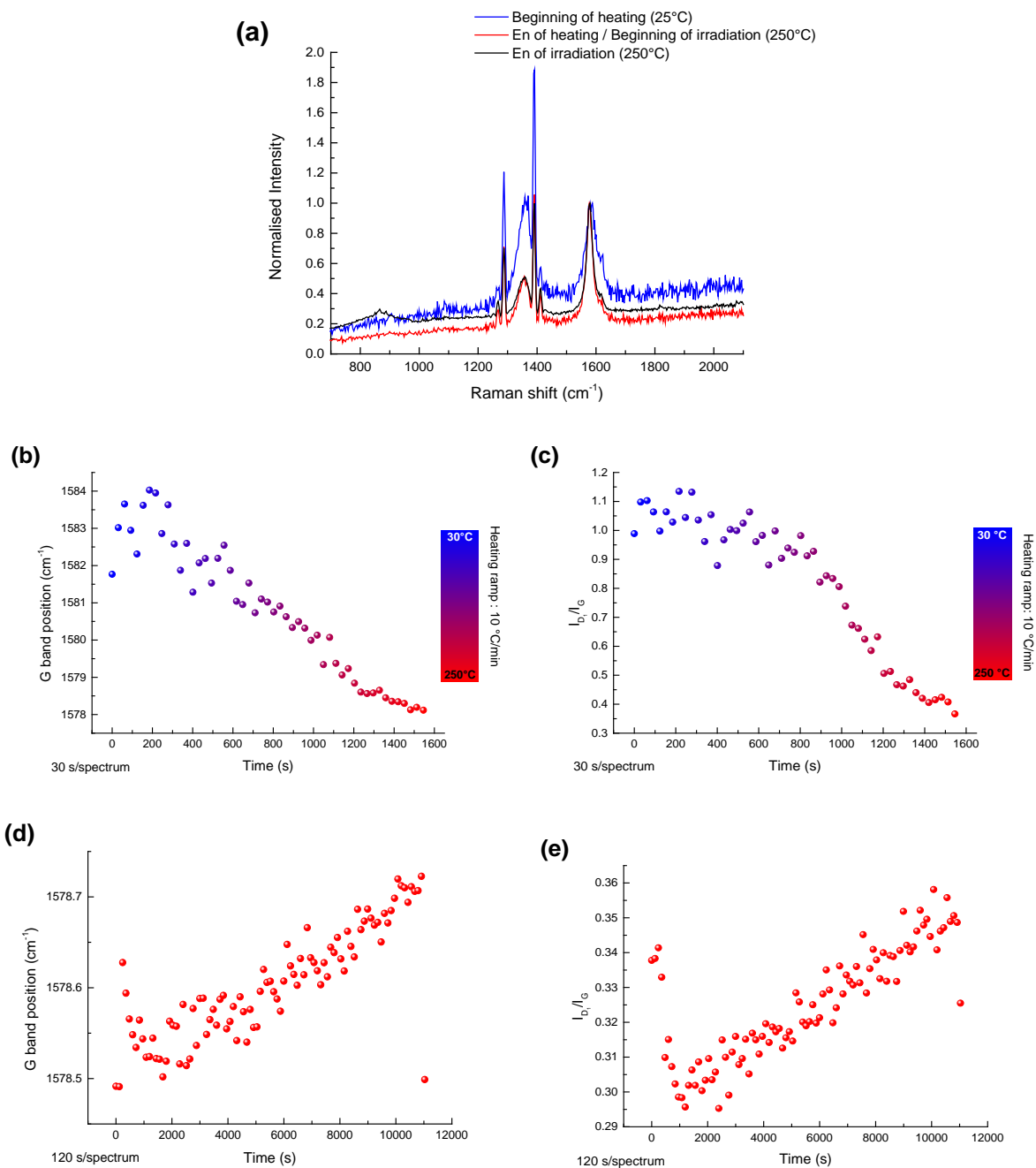
Figure 43: *(a) Spectra recorded by Raman microspectrometry at different stages of the experiment (b and c) how the position of band G and the I_{D1}/I_G intensity ratio change as the temperature is increased to 250 °C and (d and e) how the position of band G and the I_{D1}/I_G intensity ratio change during irradiation with 15.7 MeV He$^+$ ions at 250 °C and a fluence of 1 x 10^{16} at.cm^{-2}*
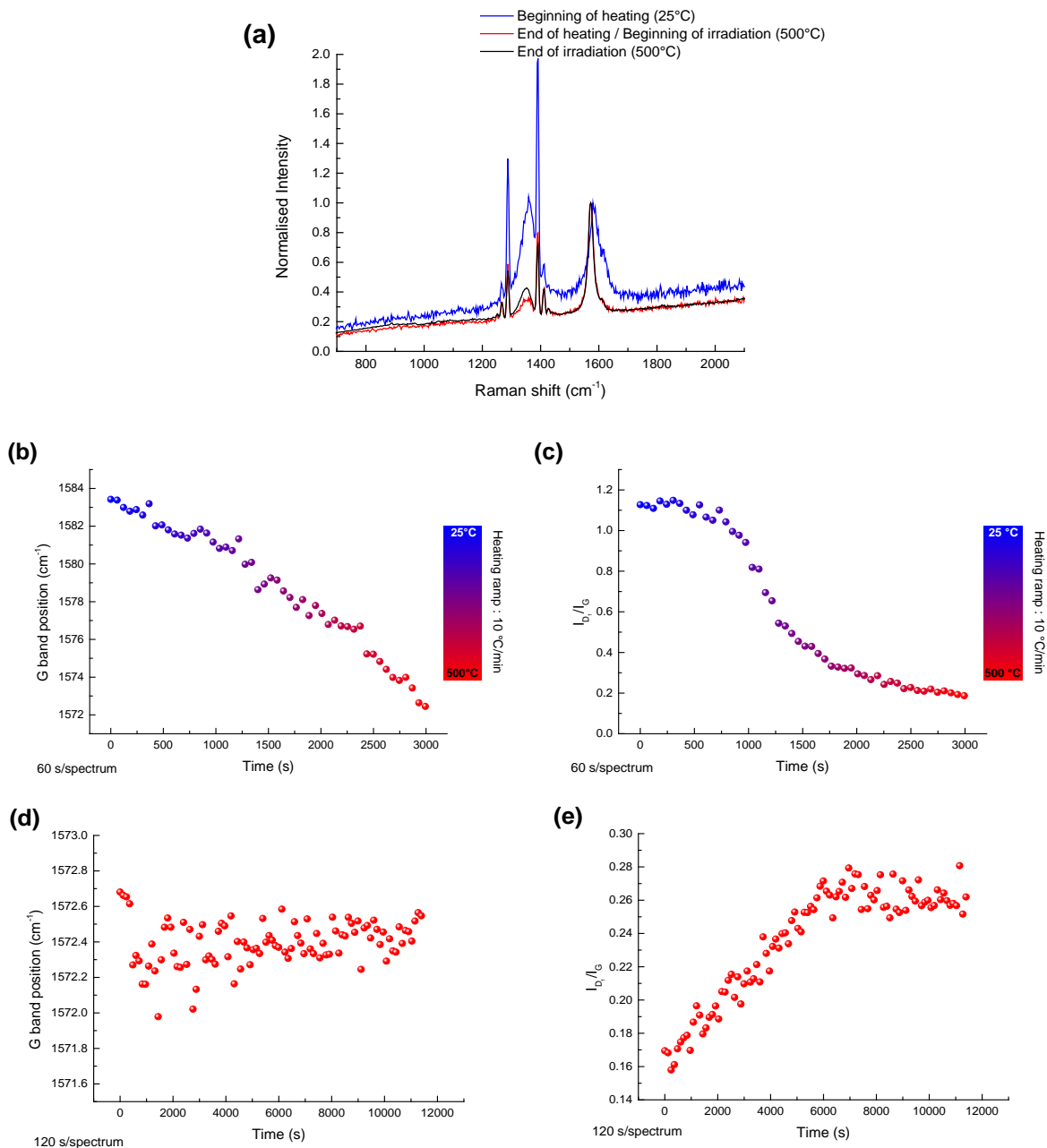
Figure 44 : *(a) Spectra recorded by Raman microspectrometry at different stages of the experiment (b and c) how the position of band G and the I_{D1}/I_G intensity ratio change as the temperature is increased to 500 °C and (d and e) how the position of band G and the I_{D1}/I_G intensity ratio change during irradiation with 15.7 MeV He$^+$ ions at 250 °C and a fluence of 1 x 10^{16} at.cm^{-2}*

Figures 43 ***b*** and 44 ***b*** show a variation in the position of band G from 1583cm^{-1} to about 1578cm^{-1} at 250°C and 1572cm^{-1} at 500°C which could be related to an expansion of the graphite structure as the temperature rises. The shift in band G as a function of temperature has already been described in the literature [Calizo 2007, Ferrari 2007, Reich 2004]. However, our experiments enable these changes to be followed in real time. Figures 43 ***c*** and 44 ***c*** show that the I_{D1}/I_G ratio decreases

over the time taken for the temperature to increase (from 250 to 500°C), from 1.1 to 0.4 at 250°C to 0.2 at 500 °C. This drop can be attributed to reordering due to temperature increase. We also point out that for these two experiments, we can clearly see an acceleration in the restructuring process between 200 and 250 °C. This effect is probably due to the relative mobility of the vacancies and interstitials which can recombine [Gauthron 1986].

During irradiation at 250 °C (Figure 43 *d*), the position of band G shifts slightly to higher values of 1578.5 to 1578.7 cm^{-1} indicating compression constraints. However, during irradiation at 500°C (Figure 44 *d*), the position of this band remains stable at around 1572.4 cm^{-1}. The I_{D1}/I_G ratio, increases linearly for both temperatures but only stabilises at 500 °C, where it reaches a threshold value of about 0.26 when the fluence reaches 5 x 10^{15} at.cm^{-2} at about 6000 s of irradiation. This plateau indicates the competitive effect of temperature which tends to reorder the graphite. In other terms, before this plateau, the effects of irradiation are dominant whereas later the effects of temperature and irradiation balance out.

Study of the microstructural state by Raman microspectrometry and TEM after irradiation

The graphs in Figure 45 are (a) the spectrum obtained by Raman microspectrometry on a sample irradiated at 500 °C compared to a TQI sample, and (b) and (c) the inter-layer distance and angular distribution values measured by TEM, respectively.

CAST
**Report on ¹³C behaviour under ion irradiation in HOPG
(model graphite) (D5.18)**
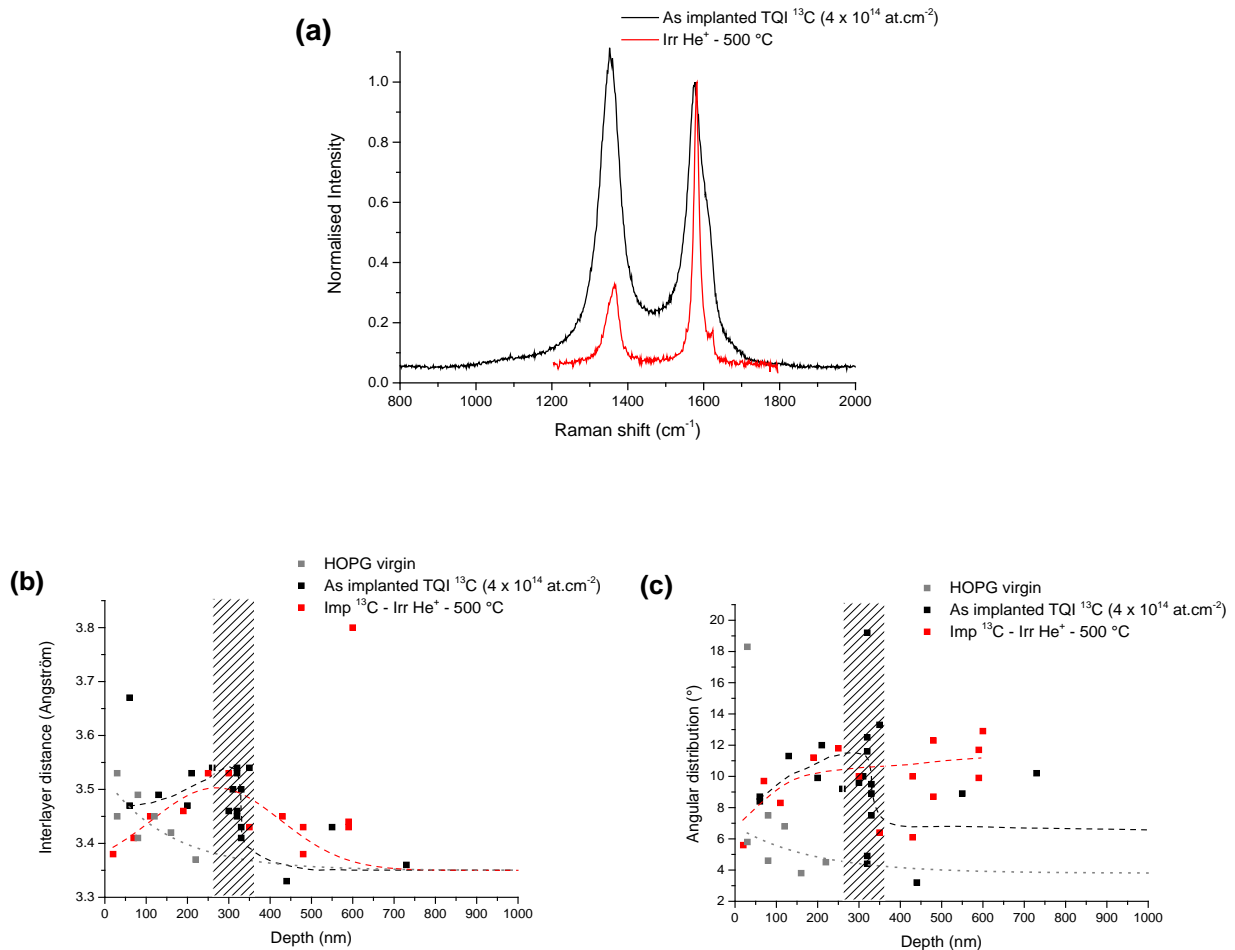
Figure 45: *(a) spectrum obtained by Raman microspectrometry of a sample irradiated at 500 °C compared to a TQI sample, and (b) and (c) inter-layer distance and angular distribution values measured by TEM, respectively. The shaded zone indicates the Rp values for the implanted ¹³C and the dashed lines enable the trends in the evolution of all the values as a function of depth to be clearly seen*

The Raman spectrum indicates reordering of the sample irradiated at 500 °C compared to the TQI sample. This phenomenon cannot be seen on the results obtained by TEM, as the inter-layer distance and the angular distribution measured for the sample irradiated at 500 °C are very similar to those of the TQI sample. However, we observed that the values for the inter-layer distance measured at the surface, for the sample irradiated at 500 °C and at a depth up to 100 nm, are lower and in fact closer to the value of 3.35 Å which is characteristic of virgin graphite. The latter result could explain the better state of the structure measured by Raman microspectrometry compared to that observed by TEM because the depth analysed by Raman spectroscopy is of some hundred nanometres.

Role of the irradiation flux

To help complete this part of the study, we also wanted to double the flux (2×10^{12} at.cm^{-2}.s^{-1}) and the irradiation fluence (2×10^{16} at.cm^{-2}) during an experiment at 500 °C. This was done on a sample initially implanted with ^{37}Cl at a fluence of 5×10^{13} at.cm^{-2}, so that the initial structural state is very similar to that of samples implanted with ^{13}C at a fluence of 4×10^{14} at.cm^{-2} and therefore the behaviour under irradiation at higher temperatures is very similar. Figure 46 shows the results obtained where (*a*) shows the spectra recorded at different steps of the experiment using Raman microspectrometry; (*b*) the evolution in the position of band G, (*c*) the I_{D1}/I_G intensity ratio as the temperature increases, and (*d*) and (*e*) the evolution in the position of band G and the I_{D1}/I_G intensity ratio during irradiation, respectively.

CAST
**Report on ^{13}C behaviour under ion irradiation in HOPG
(model graphite) (D5.18)**

EURATOM
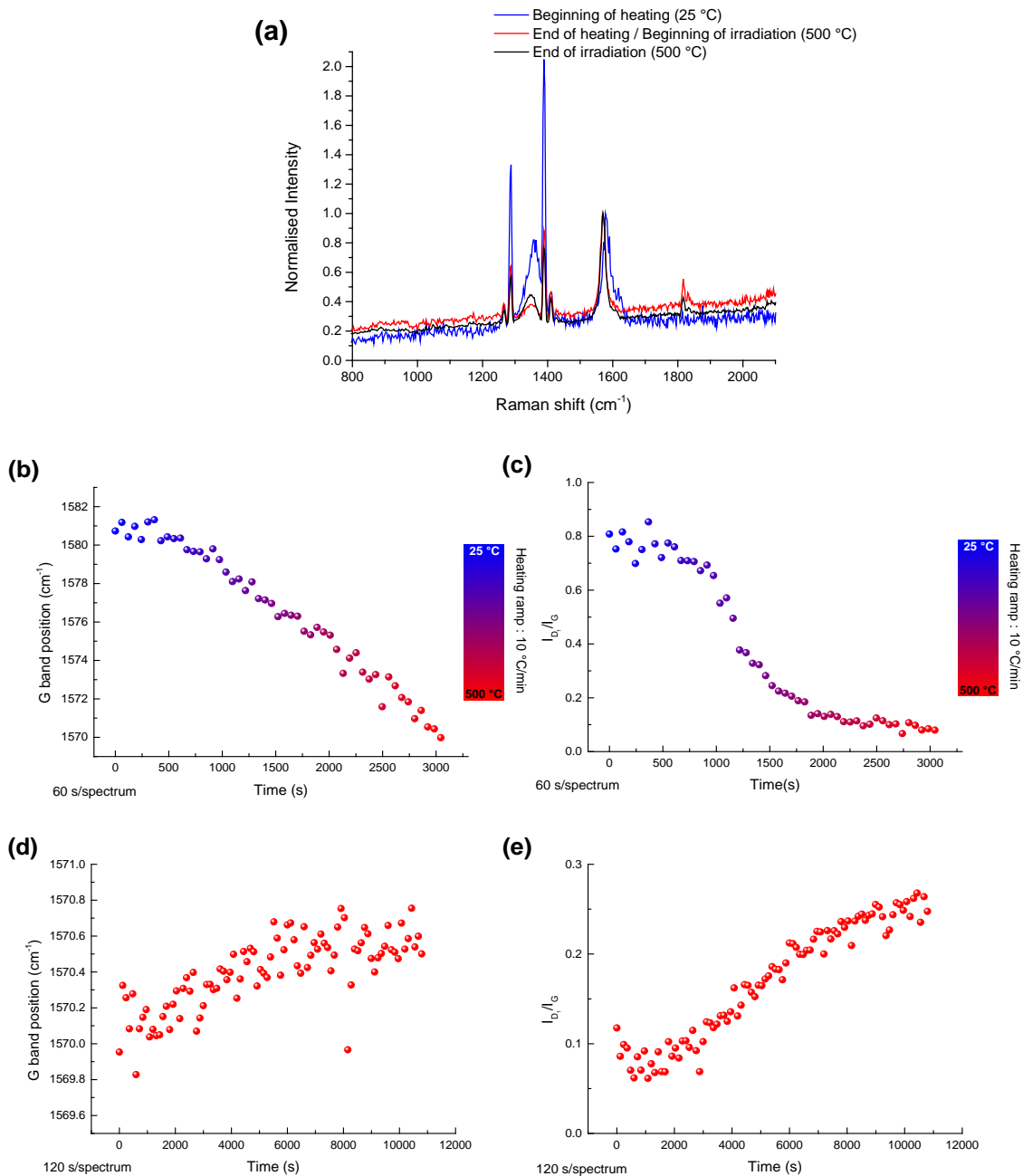
*Figure 46: (**a**) spectra recorded at different steps of the experiment using Raman microspectrometry, (**b**) and (**c**) show the evolution in the position of band G and the I_{D1}/I_G intensity ratio as the temperature increases, respectively, and (**d**) and (**e**) show the evolution in the position of this band and the intensity ratio during irradiation with 15.7 MeV He$^+$ ions at 500 °C at a fluence of 2 x 10^{16} at.cm^{-2}, respectively.*

In the same way as above, i.e. for irradiation at a fluence of 1 x 10^{16} at.cm^{-2} and as the temperature is increased to 500 °C, the position of band G shifted down from about 1581 cm^{-1} to about 1570 cm^{-1}. This shift of about 11 cm^{-1} is comparable with that observed during the previous irradiation at a lower flux but still at 500 °C. The I_{D1}/I_G intensity ratio also decreased from 0.8 to 0.1, which again confirms the reordering of the graphite with temperature. We also observe the acceleration in this decrease between 200 and 250 °C. We point out that the initial values of the I_{D1}/I_G intensity ratios differ slightly from those during irradiation at a lower flux as the implanted isotope is not the same and because of this, the Raman spectra also differ slightly. In fact, this can be seen on Figure 42 where the intensity of band D_1 is slightly lower for the sample implanted with ^{37}Cl. In addition, the initial shift in the position of band G can be explained by a slight difference in the calibration.

During irradiation, we observed a small shift in band G of about 0.5 cm^{-1} to 1570.6 cm^{-1} (Figure 46 *e*). The I_{D1}/I_G intensity ratio increases linearly in the same way as before from 0.1 to 0.28 at 12000s, corresponding to a fluence of 2 x 10^{16} at.cm^{-2}. However, this value does not stabilize i.e. there is no visible plateau.

In conclusion, in a mainly electronic regime, these results again indicate the antagonistic effects of temperature and irradiation on the evolution of the graphite structure. Furthermore, they clearly show the existence of a critical damage value above which the effects of irradiation and temperature balance out. This threshold value is reached more quickly when the temperature is higher.

The role of the flux is clearly shown in as far as it is necessary to increase the temperature to reach a balance between the effects of temperature and irradiation. We can then observe a plateau, as seen before.

C | Virgin nuclear graphite

We finally wanted to study the structural behaviour under irradiation of virgin nuclear graphite in order to compare it with the HOPG model graphite. We remind the reader that nuclear graphite has a heterogeneous structure due to the presence of coke grains and binder which therefore enables us to better simulate the conditions encountered in a UNGG reactor. The virgin nuclear graphite samples come from a G2 reactor. It is important to point out that the initial structural state is similar to that of SLA2 nuclear graphite [Vaudey 2010].

Irradiation at ambient temperature

The first sample was irradiated at ambient temperature with a flux of 1 x 10^{12} at.cm^{-2}.s^{-1} and a fluence of 1 x 10^{16} at.cm^{-2}. The spectra recorded by Raman microspectrometry at different stages of the irradiation as well as the evolution in the I_{D1}/I_G intensity ratio during this irradiation are given in Figures 47 *a* and 47 *b*, respectively.
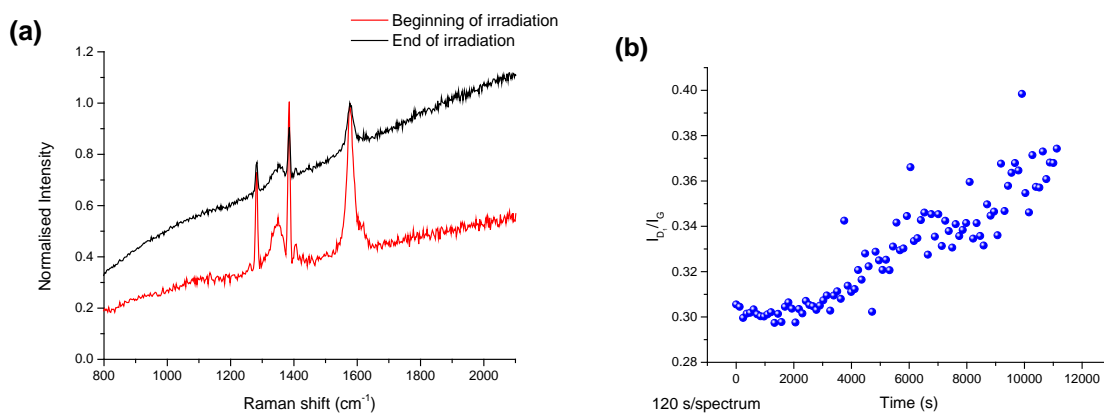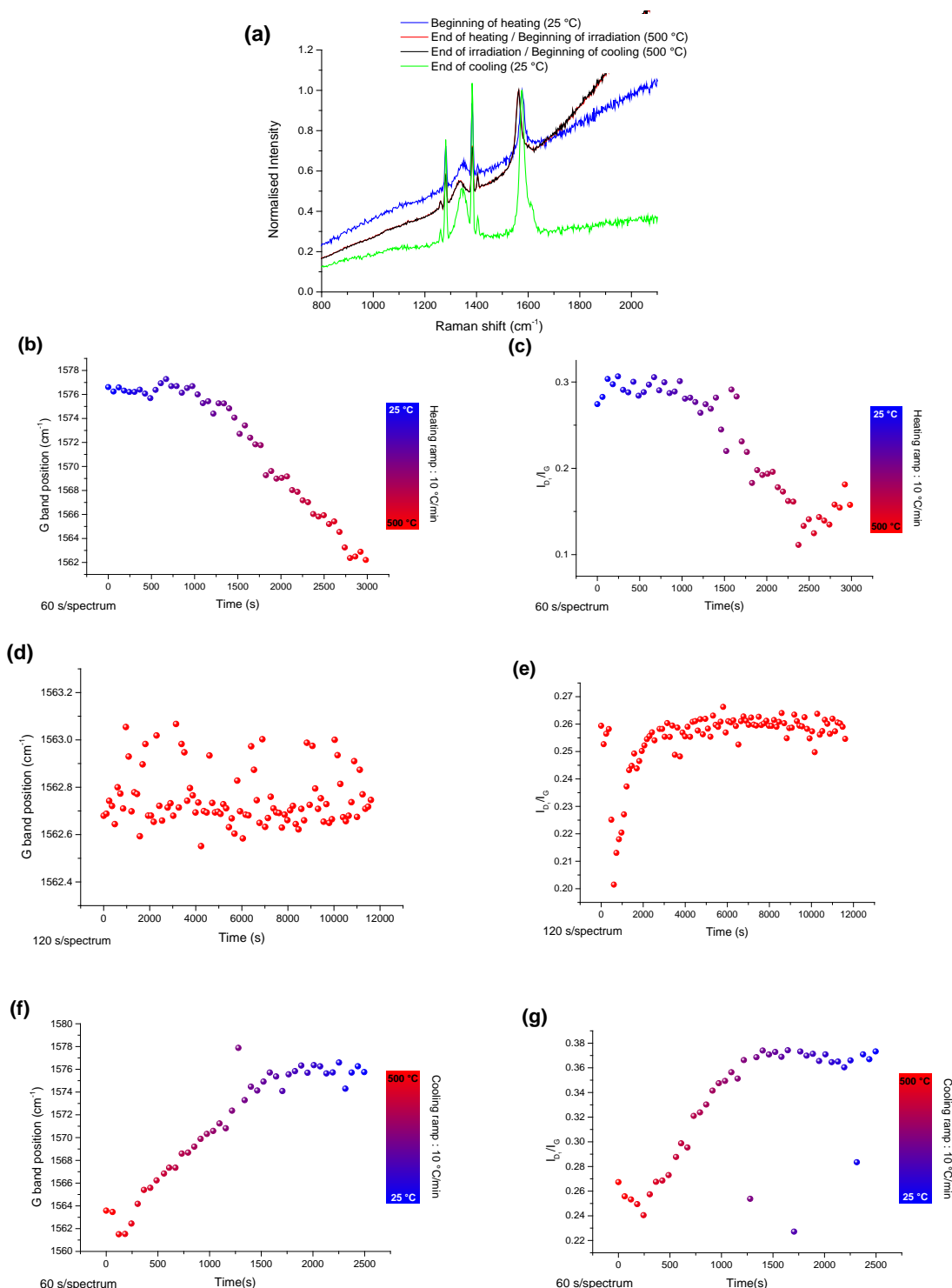
Figure 47: *(a) Raman microspectrometry spectra recorded on a sample of G2 graphite at the start and end of irradiation and (b) the evolution of the I_{D1}/I_G intensity ratio during the whole period of irradiation with 15.7 MeV He$^+$ ions at ambient temperature in the presence of UNGG gas (1 x 10^{16} at.cm^{-2})*

Figure 47 ***a*** shows that the virgin nuclear graphite is initially more disordered than the virgin HOPG model graphite, where the spectrum shows no defect band (D$_1$). In fact, for a sample of nuclear graphite, the defect band D$_1$ is already present on the spectrum before irradiation and the I_{D1}/I_G intensity ratio is about 0.3. Figure 47 ***b*** shows that this ratio increases slightly with irradiation at a fluence of 1 x 10^{16} at.cm^{-2} to reach 0.35 at the end of the experiment indicating the progressive disordering of the graphite.

<u>Irradiation at 500 °C</u>

We did the same irradiation experiment at 500 °C. Figure 48 ***a*** shows the spectra recorded by Raman microspectrometry at different stages of the irradiation, ***b*** and ***c*** the evolution of the position of band G and the I_{D1}/I_G intensity ratios during the increase in temperature, during irradiation (***d*** and ***e***) and during cooling (***f*** and ***g***).

Figure 48: *(a) shows the spectra recorded by Raman microspectrometry at different stages of the irradiation, (b and c) the evolution of the position of band G and the I_{D1}/I_G intensity ratios during the increase in temperature up to 500°C, respectively, (d and e) during irradiation with 15.7 MeV He$^+$ ions at 500 °C at a fluence of 1 x 10^{16} at.cm^{-2}, and, finally, (f and g) during cooling*

67

CAST
**Report on ^{13}C behaviour under ion irradiation in HOPG
(model graphite) (D5.18)**

During the temperature increase, band G shifts from 1576 cm^{-1} (ambient temperature) to 1562 cm^{-1} (500 °C). In addition, the I_{D1}/I_G intensity ratio decreases from 0.3 (at ambient temperature) to 0.15 (at 500 °C). As shown previously, there is a reordering of the graphite structure due to heating. In fact, the initial shift in the position of band G can be explained by a slight difference in the calibration. During irradiation, the I_{D1}/I_G intensity ratio rises to about 0.26 (similar to that measured for HOPG irradiated in the same conditions) then stabilises quickly above 3000 seconds of irradiation i.e. from a fluence of about 2 x 10^{15} at.cm^{-2}. As seen previously, it seems that we reach a disordering threshold. However, this is reached earlier at a lower fluence. In fact, the equilibrium between temperature and irradiation effects is reached at a lower graphite disordering threshold value.

We then studied the shift in band G and the change in the I_{D1}/I_G intensity ratio during cooling (Figure 48 *f* and *g*). The values of these two parameters increase as a function of cooling time. Band G stabilises at its initial position at about 1576 cm^{-1}. This shift corresponds at the contraction of the matter network during cooling. The I_{D1}/I_G intensity ratio also stabilises at about 0.37 at ambient temperature, a higher value than the initial one.

This experiment shows that dynamic heating of the graphite structure is extremely dependent not only on the initial state, in particular the degree of disorder, but also on the nature of the graphite. In fact, the threshold value for which an equilibrium is reached between the disordering effects of irradiation and the reordering effects of temperature for the implanted HOPG samples is reached at higher fluences compared to the G2 graphite for the same temperature and irradiation conditions.

### 4.3 | Conclusion concerning the effects of irradiation in a mainly electronic regime

As seen above, **the effect of irradiation in a mainly electronic regime is greatly dependent on the initial structural state of the graphite**. Furthermore, the implanted ^{13}C is stabilised in the graphite mainly in sp^3-type structures. For **initially very disordered graphite** which is then irradiated at a high electronic stopping power S_e (greater than in the range of UNGG reactors), **its structure only slightly reorders**, even at 1000 °C, contrary to that observed for irradiation in a mainly ballistic regime.

In **initially very disordered graphite**, whatever the value of S_e, there is **competition between disordering caused by irradiation and temperature which clearly have antagonistic effects**. Even at very low S_e values, found in the lower range of those in UNGG reactors, induces **slight disordering** of the graphite as much at ambient temperature as at 500 °C. In addition, **the ability of irradiation to cause disordering depends not only on the flux, temperature and initial structural state, but also on the nature of the graphite itself.**

5 | Discussion and conclusion

Let us now compare the results obtained for the **slightly disordered graphites** and the **very disordered graphites,** in relation to the two irradiation regimes.

In order to illustrate this study, we first chose a few Raman spectra obtained for the **initially very disordered HOPG** samples (7.4 dpa) irradiated with sulphur and carbon at 1000 °C. These spectra are given in Figure 49 *a* and we have added the inter-layer distance and the angular distribution for the same samples in Figure 49 *b* and *c*, respectively. Figure 50 shows the evolution of the I_{D1}/I_G intensity ratio as a function of temperature for the different irradiations on these initially very disordered samples.
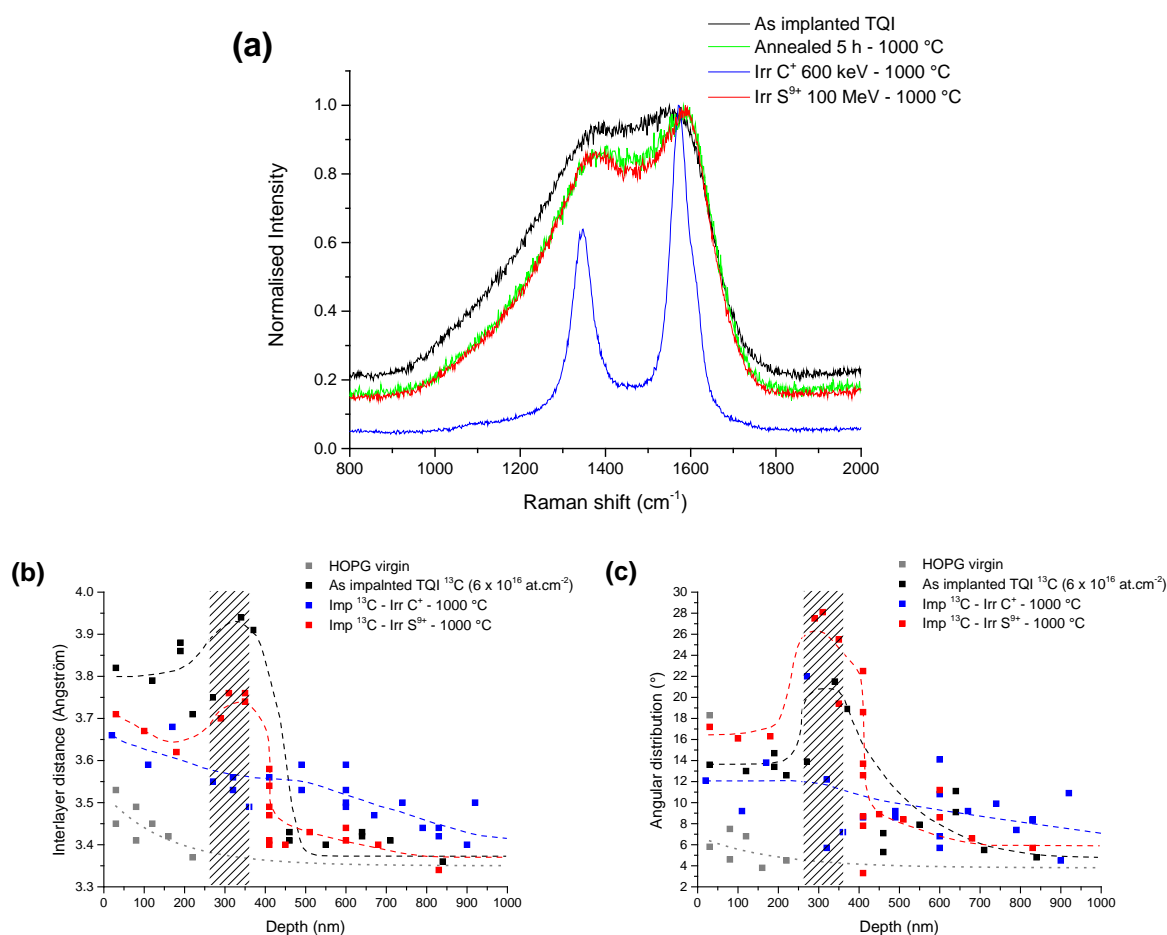
Figure 49: (a) Raman microspectrometry spectra for initially very disordered HOPG samples which have been only heated or irradiated with carbon or sulphur ions at 1000 °C, (b and c) the evolution of the inter-layer distance and angular distribution for the same samples, respectively. The shaded zone indicates the Rp values for the implanted ^{13}C and the dashed lines enable the trends in the evolution of all the values as a function of depth to be clearly seen
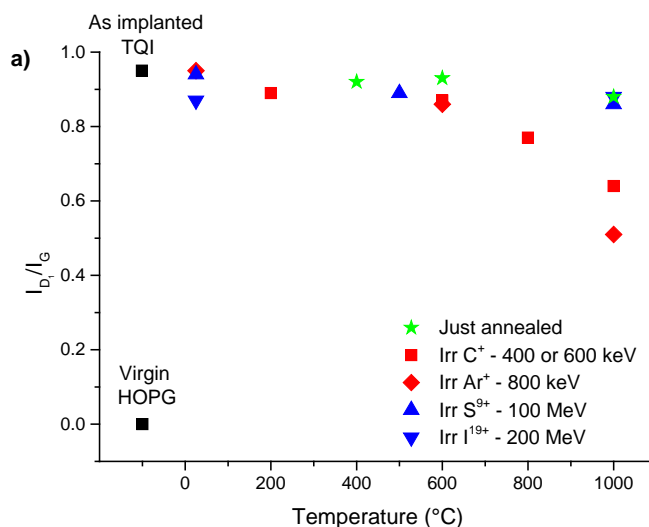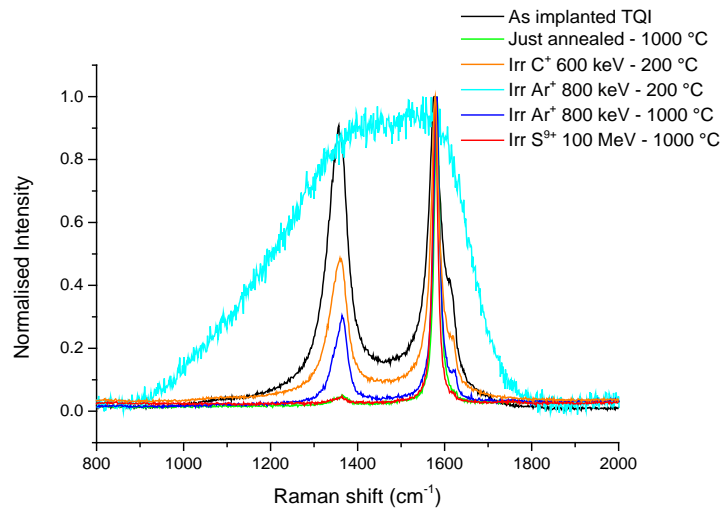
Figure 50: *Evolution of the I_{D1}/I_G intensity ratio as a function of temperature and the type of irradiation for the initially very disordered samples*

If we look at all the graphs together, they clearly show a difference in behaviour depending on whether the samples are irradiated in a ballistic or electronic regime. Irradiation in a ballistic regime, at higher than ambient temperature, favours the reordering of the graphite and the stabilisation of the ^{13}C in the sp^2 structures (Figure 49 ***a***). This effect is even clearer when the sample is irradiated at a high damage rate. In fact, Figure 50 shows that the value of the I_{D1}/I_G intensity ratio for the sample irradiated with argon ions at 1000 °C at a high dpa rate (4.4 dpa) is lower than for the sample irradiated with carbon ions (1 dpa). This Figure also shows that irradiation in an electronic regime, even at 1000 °C, leads to almost no reordering of the graphite.

The difference between the effects of irradiation in electronic and ballistic regimes is also demonstrated by the TEM results (see Figures 49 ***b*** and ***c***). In particular, the values of the inter-layer distance are clearly lower for the sample irradiated with carbon ions. In conclusion, we can state that there is a synergy between temperature and irradiation i.e. when working at higher than ambient temperature and during irradiation in a ballistic regime, the reordering of initially very disordered graphite is favoured. This effect is particularly visible above 600 °C as seen on Figure 50, most certainly due to the greater relative mobility of the vacancies and interstitials. Up to 600 °C, the irradiation regime has only a small impact on the structural state of the graphite.

We next selected some results obtained using **initially slightly disordered HOPG** samples (<< 0.1 dpa). Figure 51 shows the Raman microspectrometry spectra for samples irradiated with sulphur, carbon or argon ions. We also show the evolution of the I_{D1}/I_G intensity ratio as a function of temperature for all irradiation conditions (Figure 52).

Figure 51: *Spectra obtained by Raman microspectrometry for initially slightly disordered HOPG samples which are only heated or irradiated with argon, carbon or sulphur ions at different temperatures*
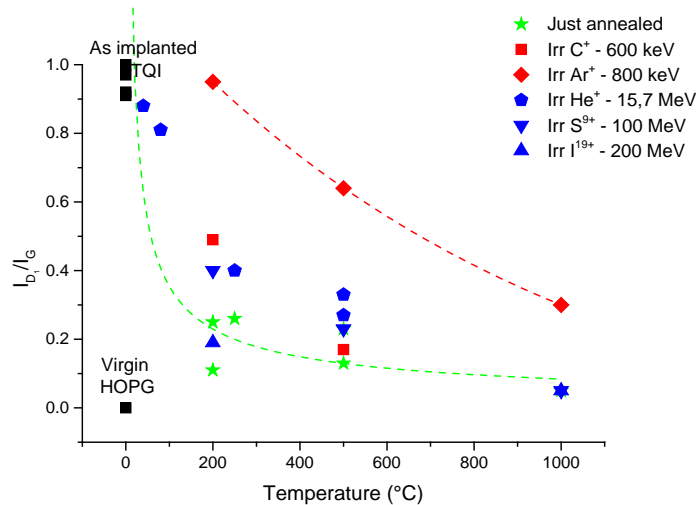
Figure 52: *Evolution of the I_{DI}/I_G intensity ratio as a function of temperature and the type of irradiation for initially slightly disordered samples. The dashed lines enable the trends of these values as a function of temperature to be clearly seen*

We observe that **whatever the regime, irradiation and temperature have antagonistic effects.** As shown in Figure 51, irradiation in a ballistic regime with argon ions at 200 °C greatly disordered the HOPG, whereas the structure reorganises at 1000 °C. In fact, above 250 °C, the recombining of the vacancies and interstitials is favoured because of their mobility. The possibility of the reordering of the graphite is in this case greatly dependent on the temperature and the rate of damage. If the latter is high (about 4 dpa for irradiation with argon ions) and at a low temperature (below 200 °C), the graphite cannot reorganise due to the reduced mobility of the defects. However, with a smaller damage rate (i.e. for irradiation with carbon ions) there is some reordering of the

CAST
**Report on ^{13}C behaviour under ion irradiation in HOPG
(model graphite) (D5.18)**

graphite, even at 200 °C. Between these two damage rates, there is probably a threshold value below which the effect of temperature cannot counterbalance the effects of irradiation.

For irradiation in the electronic regime at higher than ambient temperature, some reordering of the samples is observed but less than that under the effect of temperature alone, as can be seen in Figure 51. For example, at 200 °C the comparison of the I_{D1}/I_G intensity ratio shows that the reordering of samples irradiated with helium, sulphur or iodine ions is not as much as when the sample is only heated.

Figure 52 also highlights the fact that, whatever the irradiation regime, there is some reordering of the graphite at higher than ambient temperature. However, for irradiation at a high rate of ballistic damage (i.e. with 800 keV argon ions), the reordering of the graphite does not reach that obtained for a sample irradiated at a low rate of ballistic damage (i.e. with 400 or 600 keV carbon ions) or in an electronic regime.

The *in situ* study of the structural modifications by Raman microspectrometry of the graphite samples irradiated with helium ions showed that even a low S_e induced a disordering of the graphite as much at ambient temperature as at 500 °C. We also determined the damage threshold at which an equilibrium between the disordering effects of irradiation and the reordering effects of temperature is reached. For a given temperature and irradiation flux, the value of this threshold is decided by the type of graphite and its initial amount of damage (structural state).

Extrapolation of the results to UNGG reactors

We can now try to extrapolate these results to the structural modifications induced in graphite by irradiation in a reactor and also the behaviour of the ^{14}C in the irradiated graphite. In order to do this, we can use Figure 53 which shows schematically the neutron flux conditions and the temperatures the graphite was subjected to as a function of its position in the SLA2-type graphite stack.
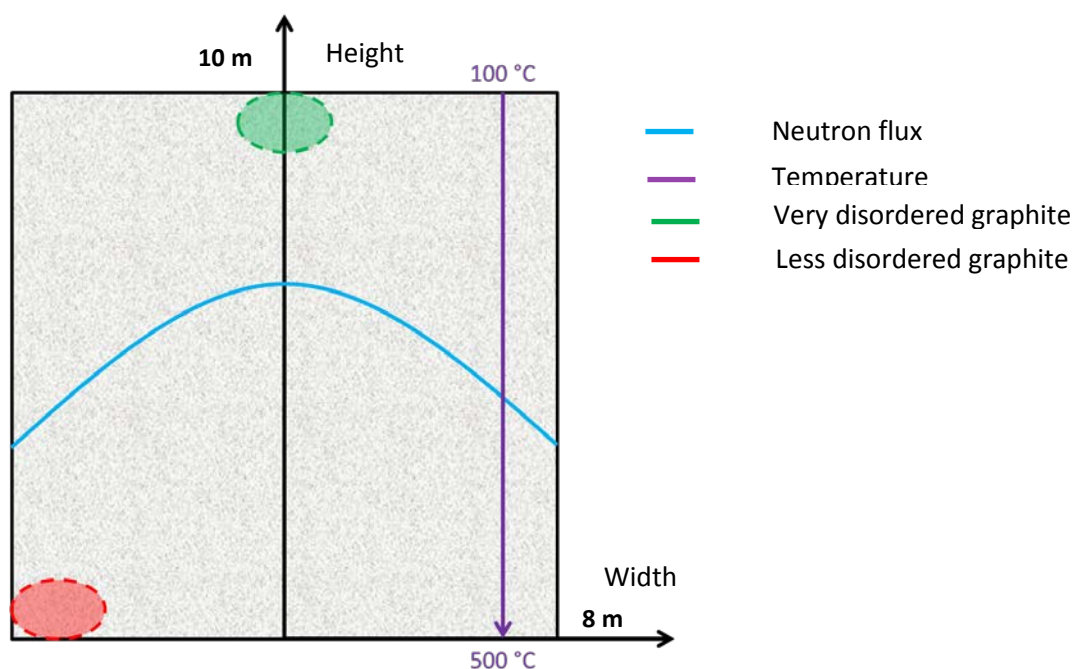
Figure 53: Structural behaviour of the graphite depending on its location in the SLA2-type stack

Let us remind that the aim is to simulate the behaviour of ^{14}C during reactor operation and evaluate the independent or synergistic effects of temperature and irradiation on ^{14}C behaviour. Indeed, the knowledge of the location and speciation of ^{14}C in irradiated graphite at reactor shutdown is important to understand and foresee its behaviour during dismantling, to optimize an eventual decontamination process and to evaluate its migration behaviour during disposal. [14]C is mainly formed through the activation of ^{13}C but a certain amount may also be generated through the activation of [14]N. In this study, ^{13}C implanted into model HOPG graphite is mainly used to simulate the behaviour of ^{14}C, displaced from its original structural site through recoil, in coke grains which build around 80% of nuclear graphite. [13]C was implanted at different fluences. This allows inducing a high or a low disorder into the graphite matrix which is representative of the multiplicity of the structure states already present in nuclear graphite. It also allows simulating structural differences resulting from early neutron irradiation in high or low flux regions of the reactor. Then, the samples were ion irradiated to simulate neutron irradiation.

The collision of the impinging neutrons with the graphite matrix carbon atoms induces mainly ballistic damage. However, a part of the recoil carbon atom energy is also transferred to the graphite lattice through electronic excitation. Therefore we simulated the effects of the different irradiation regimes coupled with temperature using ion irradiation by varying the Sn(nuclear)/Se(electronic) stopping power ratio. Thus, the samples were irradiated with different ions of different energies at various facilities using dedicated irradiation cells.

The results show that temperature generally counteracts the disordering effects of irradiation but the achieved reordering level strongly depends on the initial structural state of the graphite matrix. Ion irradiation in both ballistic and electronic regimes disorders the graphite structure and promotes the formation of sp^3 bonds. On the contrary, temperature has reordering effects in both regimes,

73

resulting into the formation of new sp^2 structures. The results also show that graphite structure modifications are mainly due to the ballistic impact. When the structure is already strongly disordered, ballistic irradiation and temperature have a synergistic reordering action due to temperature enhanced mobility of the pre-existing and irradiation induced vacancies and interstitials. When the electronic excitation values are "low", as in the case of UNGG or Magnox reactors, they have low impact on graphite structure evolution.

For a very damaged graphite structure (for example, coke grains which have remained in a reactor for several years in a high neutron flux zone), the irradiation will have little impact on the evolution of its structure. This is because the temperatures at which the UNGG reactors function, i.e. between 200 and 500 °C at the most, are insufficient in annealing the defects. However, the evolution of an initially slightly disordered graphite structure (in the case of coke grains irradiated with a low neutron flux), will be greatly affected by the irradiation flux and temperature. The result could therefore lead to very different structural states as a function of the position of the graphite in the reactor. Consequently, graphite irradiated with a low neutron flux and situated in a hot zone (500 °C), such as the red zone in Figure 53, would probably be characterised by a structure similar to that of well-ordered graphite. However, graphite irradiated with a high neutron flux situated in a cold zone (200 °C), such as the green zone in Figure 53, would keep its damaged/disordered structure. This phenomenon can also be seen on Figure 52.

We have demonstrated that both the nature and initial structural state of the graphite as well as the irradiation conditions in the reactor are likely to generate significant structural heterogeneity in the graphite moderator in the UNGG reactors. These results could explain, at least partly, the significant structural contrasts observed by J. Pageot [Pageot 2014] for graphites irradiated with neutrons.

Concerning ^{14}C, apart from the ^{14}C formed by activation of ^{14}N located close to free surfaces for which a great part has probably been removed through radiolytic corrosion, both temperature and irradiation would tend to be stabilise it in the irradiated graphite structure: in planar sp^2 structures (in both aromatic cycles and chains) or three dimensional sp^3 structures (allowing interstitials carbon atoms to bond between the basal layers) [Ammar 2015, Eapen 2014]. The proportion of these structures would be variable and linked with the irradiation history. Thus, in case of disposal, the ^{14}C stabilisation, especially into sp^2 aromatic structures, should lead to reduced leaching rates in comparison to ^{14}C present in degraded and porous graphite.

Furthermore, in case of prior purification, ^{14}C stabilised into the "hot" parts of the irradiated graphite should be more difficult to extract in comparison to ^{14}C present in "cold" and disordered zones. Moreover, as the majority of the ^{14}C would have been produced in zones submitted to high neutron flux and greatly disordered, these ^{14}C enriched zones would then be more easy to decontaminate using CO_2 gasification based or steam reforming processes as shown by Pageot [Pageot 2015] and Galy [Galy 2016] due to the selective gasification of the most degraded areas. Thus, keeping a reduced mass loss of around 5%, Pageot showed that around 20% of the total ^{14}C could be gasified in SLA2 or G2 graphites.

References

[Ammar 2010 b] M.R. Ammar, J.N. Rouzaud, C.E. Vaudey, N. Toulhoat, N. Moncoffre, Characterization of graphite implanted with chlorine ions using combined Raman microspectrometry and transmission electron microscopy on thin sections prepared by focused ion beam. Carbon. 2010; 48(4):1244-51

[Ammar 2015] M. R. Ammar, N. Galy, J.-N. Rouzaud, N. Toulhoat, C.-E. Vaudey, P. Simon, N. Moncoffre, Characterizing various types of defects in nuclear graphite using Raman scattering: Heat treatment, ion irradiation and polishing, Carbon 95 (2015) 364-373

[Baird 1980] T. Baird, 1980. Carbon deposition on metals. Proceeding 4 of Salford: 34-39.

[Beny-Basset 1985] C. Beny-Bassez, J.N. Rouzaud. Scanning electron microscopy, Vol. I. SEM Inc., AMF O'Hare (Chicago), IL 60666 USA, 1985, 119pp**.**

[Blondel 2013] BLONDEL, A. (2013). *Effets de la température et de l'irradiation sur le comportement du chlore 37 dans le graphite nucléaire : Conséquences sur la mobilité du chlore 36 dans les graphites irradiés*. Thèse de doctorat, Université Claude Bernard Lyon 1, IPNL. Physique des *Matériaux, LYCEN T 2013-15*

[Blondel 2014] A. Blondel, N. Moncoffre, N. Toulhoat, N. Bérerd, G. Silbermann, P. Sainsot, J.-N. Rouzaud, D. Deldicque, New advances on the thermal behaviour of chlorine in nuclear graphite, Carbon Volume 73, July 2014, Pages 413–420

[Bonal 2006] BONAL, J.-P. et ROBIN, J.-C. (2006). *Les réacteurs nucléaires à caloporteur gaz*, pages 27–32. CEA/DEN.

[Calizo 2007] I. Calizo, A.A. Balandin, W. Bao, F. Miao, C.N. Lau, Temperature dependence of the Raman spectra of graphene and graphene multilayers, Nano Letters, 2007, Vol. 7, No.9, 2645-2649

[Couzi 2016] M. Couzi, J.-L. Bruneel, D. Talaga, L. Bokobza, A multi wavelength Raman scattering study of defective graphitic carbon materials: The first order Raman spectra revisited, Carbon 107 (2016) 388-394

[Eapen 2014] J. Eapen, R. Krishna, T.D. Burchell, K.L. Murty (2014), Early damage mechanisms in nuclear grade graphite under irradiation, Materials Research Letters 2:1, 43-50

[Ewels 2003] C.P. Ewels, R.H Telling, A.A. El-Barbary, M.I. Heggie, Metastable Frenkel Pair Defect in Graphite: Source for Wigner Energy?, Physical Review Letter, Vol 91, 2 (2003)

[Faircloth 1980] R.L. Faircloth, 1980. Coolant chemistry of the advanced carbon dioxide cooled reactor. Specialists meeting on coolant chemistry, plate-out and decontamination in gas-cooled reactors Juelich, Federal Republic of Germany IAEA, B 9-06: 125-131.

[Ferrari 2000] Ferrari, A.C. & Robertson, J., 2000. Interpretation of Raman spectra of disordered and amorphous carbon., 61(20), pp.95–107

[Ferrari 2007] A.C. Ferrari, Raman spectroscopy of graphene and graphite: Disorder, electron-phonon coupling, doping and nonadiabatic effects, Solid State Communications 143 (2007) 47-57

[Frank 2010] O. Frank et al., (2010), Compression Behavior of single-layer graphene

[Frank 2011 a] O. Frank et al., (2011), Graphene under uniaxial deformation: a Raman study, Nanocon 2011, 21-23/09/2011, Brno, Czech Republic, EU

[Frank 2011 b] O. Frank et al., Development of a universal stress sensor for graphene and carbon fibres, Nature communications 2:255, 2011, DOI: 10.1038/ncomms1247

[Galvez 2002] A. Galvez, N. Herlin-Boime, C. Reynaud, C. Clinard, J.N. Rouzaud, Carbon 40 (2002) 2775–2789.

[Galy 2016] N. Galy, (2016) *Comportement du 14C dans le graphite nucléaire: Effets de l'irradiation et décontamination par vaporéformage*, Thèse de Doctorat, Université Claude Bernard Lyon 1, LYCEN – T 2016-12

[Galy 2017] N. Galy, N. Toulhoat, N. Moncoffre, Y. Pipona, N. Bérerd , M.R. Ammar, P. Simon, D. Deldicque, P. Sainsot, Ion irradiation to simulate neutron irradiation in model graphites: consequences for nuclear graphite, Nucl. Instr. Meth. B (2017), http://dx.doi.org/10.1016/j.nimb.2017.05.056

[Gauthron 1986] GAUTHRON, M. (1986). *Introduction au génie nucléaire Tome 1 : Neutronique et matériaux*. INSTN/CEA.

[Le Guillou 2015] M. Le Guillou, J.N. Rouzaud, D. Deldicque, N. Toulhoat, Y. Pipon, N. Moncoffre, Carbon 94 (2015) 277–284.

[Lehtinen 2011] O. Lehtinen and T. Nikitin (2011). "Characterization of ion-irradiation-induced defects in multi-walled carbon nanotubes." New Journal of Physics 13.

[Liu 2006] J. Liu, H.-J. Yao, et al. (2006). "Temperature annealing of tracks induced by ion irradiation of graphite." Nuclear Instruments and Methods in Physics Research Section B: Beam Interactions with Materials and Atoms 245(1): 126-129.

[Mohiuddin 2008] T. M. G. Mohiuddin et al. Uniaxial strain in graphene by Raman spectroscopy: G peak splitting, Gruneisen parameters and sample orientation, arXiv:0812.1538v1, 2008

[Moncoffre 2016] N. Moncoffre et al., Impact of radiolysis and radiolytic corrosion on the release of ^{13}C and ^{37}Cl implanted into nuclear graphite: Consequences for the behaviour of ^{14}C and ^{36}Cl in gas cooled graphite moderated reactors, Journal of Nuclear Materials 472 (2016) 252-258

[Pageot 2014] J. Pageot, Etude d'un procédé de décontamination du 14C par carboxy-gazéification des déchets de graphite nucléaire, thèse de doctorat de l'Université Paris-Sud, Andra, 2014.

[Pageot 2015] J. Pageot, J.-N. Rouzaud, M. Ali Ahmad, D. Deldicque, R. Gadiou, J. Dentzer, L. Gosmain, Milled graphite as a pertinent analogue of French UNGG reactor graphite waste for a CO2 gasification-based treatment, Carbon 86 (2015) 174-187

[Pimenta 2007] M. A. Pimenta, G. Dresselhaus, M. S. Dresselhaus, L. G. Cancado, A. Jorio, and R. Saito, Studying disorder in graphite-based systems by Raman spectroscopy, Physical Chemistry Chemical Physics 9, 1276 (2007).

[Poncet 2013] B. Poncet, L. Petit, Method to assess the radionuclide inventory of irradiated graphite waste from gas-cooled reactors, J. Radioanal. Nucl. Chem. 298, 941-953, 2013

[Reich 2004] S. Reich, C. Thomsen, Raman spectroscopy of graphite, The Royal Society, Phil. Trans. R. Soc. Lond. A (2004) 362, 2271-2288

[Rouzaud 1983] Rouzaud, J.-N., Oberlin, A. & Beny-Bassez, C., 1983. Carbon films: Structure and microtexture (optical and electron microscopy, Raman spectroscopy). Thin Solid Films, 105(1), pp.75–96.

[Rouzaud 2002] J.-N. Rouzaud, C. Clinard, Quantitative high-resolution transmission electron microscopy: a promising tool for carbon materials characterization, Fuel Processing Technology 77-78 (2002) 229-235

[Seitz 1956] F. Seitz, J.S. Koehler, Solide state physics 2, 305, 1956

[Sgouros 2016] A.P. Sgouros, G. Kalosakas, C. Galiotis, K. Papagelis, Uniaxial compression of suspended single and multilayer graphenes, DOI: 10.1088/2053-1583/3/2/025033, 2016

[Silbermann 2013] SILBERMANN, G. (2013). *Effets de la température et de l'irradiation sur le comportement du ^{14}C et de son précurseur ^{14}N dans le graphite nucléaire. Etude de la*

décontamination thermique du graphite en présence de vapeur d'eau. Thèse de doctorat, Université Claude Bernard Lyon 1, IPNL & EDF/CIDEN, LYCEN T 2013-12

[Silbermann 2014] G. Silbermann, N. Moncoffre, N. Toulhoat, N. Bérerd, A. Perrat-Mabilon, G. Laurent, L. Raimbault, P. Sainsot, J.-N. Rouzaud, D. Deldicque, Temperature effects on the behavior of carbon 14 in nuclear graphite, Nuclear Instruments and Methods in Physics Research B 332, 106–110, 2014.

[Telling 2003] R.H Telling, C.P. Ewels, A.A. El-Barbary, M.I. Heggie, Wigner defects bridge the graphite gap, Nature Materials, Vol 2 May 2003 doi:10.1038/nmat876

[Thomé 2010] L. Thomé, S. Moll, J. Jagielski, A. Debelle, F. Garrido, G. Sattonnay, Damage Accumulation in Nuclear Ceramics, VIII International Conference ION 2010, Kazimierz Dolny, Poland, 2010, pp. 7-12.

[Toulemonde 1993] M. Toulemonde, E. Paumier, C. Dufour, Thermal spike model in the electronic stopping power regime, Radiation Effects and Defects in solide 126 (1993) 201-206

[Toulemonde 2012] M. Toulemonde, W.Assmann, C.Dufour, A. Meftah, C. Trautmann Nanometric transformation of the matter by short and intense electronic excitation: Experimental data versus inelastic thermal spike model, Nuc. Ins. Meth. B 277 (2012) 28-39

[Toulhoat 2015] N. Toulhoat, N. Moncoffre, N. Bérerd, Y. Pipon, A. Blondel, N. Galy, P. Sainsot, J.-N. Rouzaud, D. Deldicque, Ion irradiation of 37Cl implanted nuclear graphite: Effect of the energy deposition on the chlorine behavior and consequences for the mobility of 36Cl in irradiated graphite Journal of Nuclear Materials Volume 464, September 2015, Pages 405–410**[Tuinstra 1970]** F. Tuinstra, & L. Koenig, (1970). Raman Spectrum of Graphite. *The Journal of Chemical Physics*, 53, pp.1126–1130.

[Vaudey 2009] C-E.Vaudey, N.Toulhoat, N.Moncoffre, N.Bérerd, L.Raimbault, P.Sainsot, J-N.Rouzaud, A.Perrat-Mabilon, Thermal behaviour of chlorine in nuclear graphite at a microscopic scale, Journal of Nuclear Materials, Volume 395, Issues 1-3, December 2009, Pages 62-68

[Vaudey 2010 a] C.E.Vaudey, N.Toulhoat, N.Moncoffre, N.Bérerd, Chlorine speciation in nuclear graphite: consequences on temperature release and on leaching, Radiochim. Acta 98, 1–7 (2010) / DOI 10.1524/ract.2010.1767

[Vaudey 2010 b] Vaudey, C.-E. (2010). *Effets de la température et de la corrosion radiolytique sur le comportement du chlore dans le graphite nucléaire : conséquences pour le stockage des graphites irradiés des réacteurs UNGG.* Thèse de doctorat, Université Claude Bernard Lyon 1, IPNL. LYCEN T 2010-12

[Wirth 2009] R. Wirth, Focused ion beam (FIB) combined with SEM and TEM: advanced analytical tools for studies of chemical composition, microstructure and crystal structure in geomaterials on a nanometer scale, Chem. Geol. 261 (2009) 217– 229.

[Wright 1980] J. Wright, 1980. Historical introduction to gas chemistry in nuclear reactors. Introduction of Salford Proceeding: 1-5.

[Ziegler 1985] J-F.Ziegler et al., (1985) « The Stopping and Range of Ion in Solids », Pergamon Press, New York.

[Ziegler 2010] J.F. Ziegler et al., 2010. Srim ‑ the stopping and range of ions in matter (2010). Nuclear Instruments and Methods in Physics Research Section B: Beam Interactions with Materials and Atoms, 268(11‑12): 1818-1823.

ANNEX

1 Simulation of the presence of ^{14}C and of the different structural states using ion implantation

We used stable isotope implantation to simulate the presence of radionuclides. ^{13}C is used to simulate the presence of ^{14}C. Moreover, in order to simulate different structural states of nuclear graphite, we implanted ^{13}C or ^{37}Cl at different fluences.

The implantations were carried ou on the IMIO 400 implantor of IPNL by Anthony Duranti or by Yann le Gall.on the EATON 200 MC implantor at Strasbourg (France).
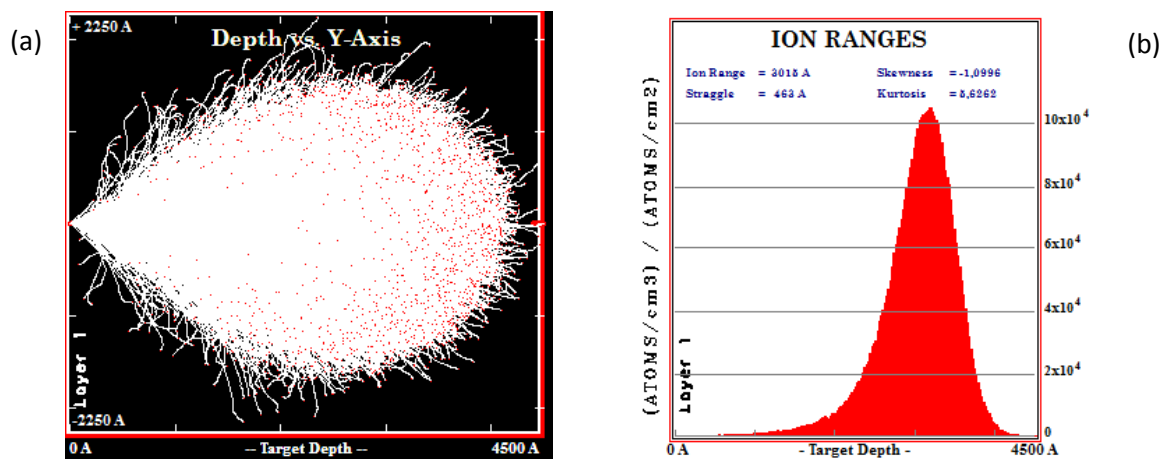
1.1 ^{13}C implantation

^{14}C has two main precursors, ^{14}N and ^{13}C and ^{14}C is produced by neutron activation respectively through following reactions ^{14}N(n,p)^{14}C and ^{13}C(n,γ)^{14}C. Knowing that in UNGG reactors, most of the remaining ^{14}C has been produced from ^{13}C (around 1,07 at.%) which is uniformly distributed in the graphite structure [Poncet], the implanted ^{13}C is in our case representative of ^{14}C issued from ^{13}C.

[Silbermann 2013] calculated that fore over 99 % neutron captures, the values of the recoil energies of ^{14}C are between 1431.5 et 2577.1 eV (respectively 16 % and 83 %). These values are higher than that of the C=C bounds in the graphene planes and show that almost all the ^{14}C has been displaced from its original structural sites. Hence, ^{13}C implantation seems to be a good choice to simulate the presence of ^{14}C issued through the neutron activation of ^{13}C as the implantation process places ^{13}C into an interstitial position.

^{13}C was implanted parallel to c axis at two fluences: 6 x 10^{16} at.cm^{-2} on one hand and 4 x 10^{14} at.cm^{-2} on the other hand in both cases at room temperature. The highest fluence allows implanting around 5 at.% at the maximum projected range R_p. This value is five times higher than the natural abundance of 1.07 at.% and is necessary to enable the analyses of ^{13}C by Secondary Ion Mass Spectrometry (SIMS). It induces a great disordering of the structure (around 7.4 dpa at the maximum projected defect range R_d). This value of the disordering is high but it is in the same order of magnitude than that reached in UNGG reactors after 11.3 years of full power operation at neutron fluence of 3.4 x 10^{21} n.cm^2 (around 2.6 dpa) [Bonal 2006]. The lowest fluence allows obtaining a less disordered structure (around 0.05 dpa at the R_d) but the maximum ^{13}C concentration is of 0.039 at/% and is therefore not measurable by SIMS. It allows creating around 0.02 dpa at the R_d. Thus, the disorder induced by the low fluence implantation might reflect the early operation stage while the one induced by the high fluence implantation might reflect the graphite structure at the reactor operation breakdown. The implantation parameters have been calculated using SRIM [Ziegler 1985, Ziegler 2010] considering a matrix density of 2.2 (close to the mean density of HOPG). The calculations were made using the Quick Kinchin-Pease model and assuming a carbon displacement energy of 28 eV. The implantation energy was of 150 keV thus allowing ^{13}C to be implanted at a depth of 300 nm which is good compromise for subsequent SIMS analyses and Raman characterizations.

Figure 1 *a* shows the path calculated for 100 000 implanted ions and Figure 1*b* represents the quasi Gaussian theoretical implantation profile. Figure 2 represents the vacancy profile. Table 1 resumes the implantation features.

(a)
(b)

Figure 1 : *a) Ion path calculated for 100 000 implanted ions and b) theoretical implantation profile of* [13]*C at 150 keV in graphite of density densité 2.2 according to SRIM-2013 [Ziegler 1985, Ziegler 2010]*
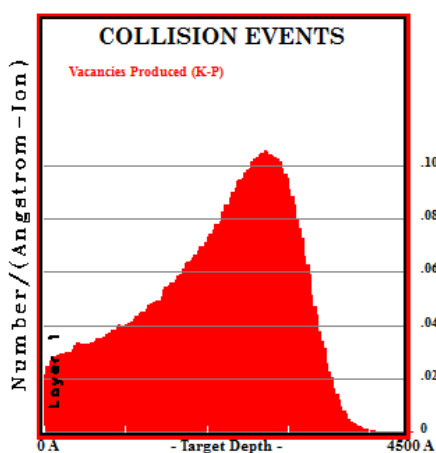

Figure 2 : *Simulation of the vacancy profile induced by* [13]*C implantation at 150 keV into graphite according to SRIM 2013[Ziegler 1985, Ziegler 2010]*

Table 1: [13]*C implantation features into graphite*

Implanted element	Implantation energy (keV)	Implantation fluence (at.cm^{-2})	Concentration at the profile max. (at.%)	Rp (nm)	Rd (nm)	Number of dpa at Rd
[13]C	150	4×10^{14}	0,039	315	275	0,05
[13]C	150	6×10^{16}	5,53	315	275	7,5

Figure 3 represents the ^{13}C implantation profiles for fluences of 6 x 10^{16} at.cm^{-2} and 4 x 10^{14} at.cm^{-2} as well as the nuclear and electronic stopping powers and the dpa induced by implantation
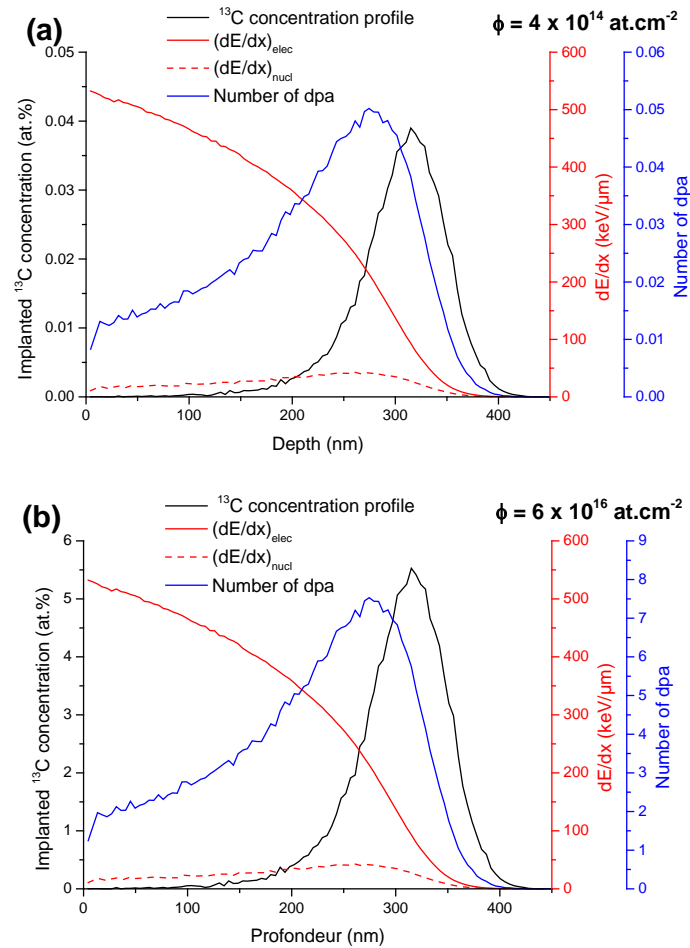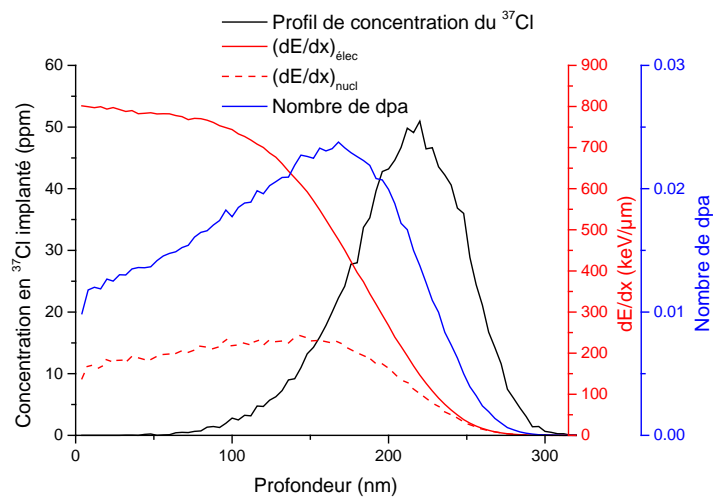

Figure 3 : *^{13}C implantation features at an energy of 150 keV and fluences of 4 x 10^{14} at.cm^{-2} (a) and 6 x 10^{16} at.cm^{-2} (b) calculated with SRIM-2013 [Ziegler 1985, Ziegler 2010]*

1.2 | ^{37}Cl implantation

Because the behaviour of ^{37}Cl was also studied in our laboratory, we used in some cases samples implanted with ^{37}Cl to induce a low disorder level into the graphite structure. In this case the implantation energy was of 250 keV and the R_p around 200 nm. An implantation fluence of 5 x 10^{13} at.cm^{-2} allows simulating a disorder level close to that induced by the implantation of ^{13}C at 4 x 10^{14} at.cm^{-2}. This fluence corresponds to a maximum ^{37}Cl concentration of 51 at.ppm [Vaudey 2010]. The number of dpa was evaluated at 0,024 dpa at the R_d [Vaudey 2010]. The implantation features are resumed in table 2 and Figure 4.

Table 2: *[37]Cl implantation features into graphite*

Implanted element	Implantation energy (keV)	Implantation fluence (at.cm^{-2})	Concentration at the profile max. (at.%)	Rp (nm)	Rd (nm)	Number of dpa at Rd
[37]Cl	250	5 x 10^{13}	51	220	168	0,024

Figure 4: *[37]Cl implantation features at a fluence of 5 x 10^{13} at.cm^{-2} and an energy of 250 keV according to SRIM-2013[Ziegler 1985, Ziegler 2010]*

2 Sample characterization

2.1 SIMS analysis

SIMS analyses were carried out by J.Brissot and J.Amalric on the IONTOF ToF-SIMS V at the Science et Surface laboratory, Ecully, France.

Figure 5: *Pictures of the IONTOF ToF-SIMS V and the ionisation chamber*

The focused primary beam was rastered over an area of 100 x 100 µm on the sample surface. Secondary ions were collected from a smaller region (20 · 20 µm^2) located at the centre of the sputtered area to minimize crater-edge effects. Figure 6 displays both zones: the sputtered region (red dots) and the analyzed zone (red filled square). This image was recorded using polarized light microscopy (Axioskop 40, ZEISS).
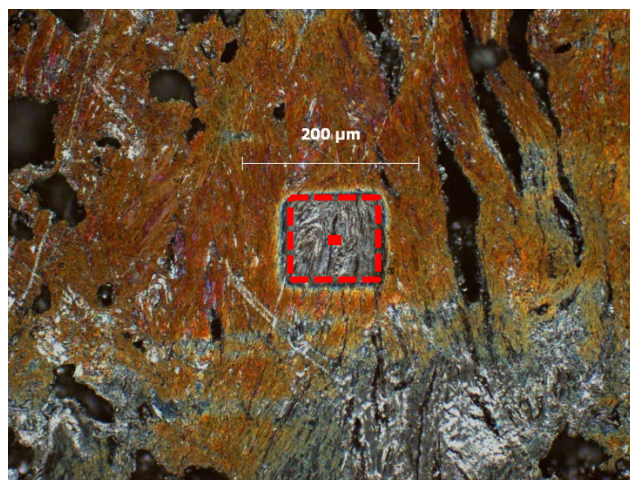
Figure 6: *Polarized light microscopy image of the sputtered (red dots) and analyzed zone (red filled square) by SIMS*

The sputter profiles measured by SIMS are given in function of the sputtering time (Figure 7). The depth scale for each sputter profile was determined by measuring the crater depth by optical interferometry at the INSA (*Institut National des Sciences Appliquées*) of Lyon in collaboration with P. Sainsot using a FOGAL NANOTECH optical profilometer coupled to a 3D Microsurf microscopic interferometer in order to convert the sputter time into depth scale.
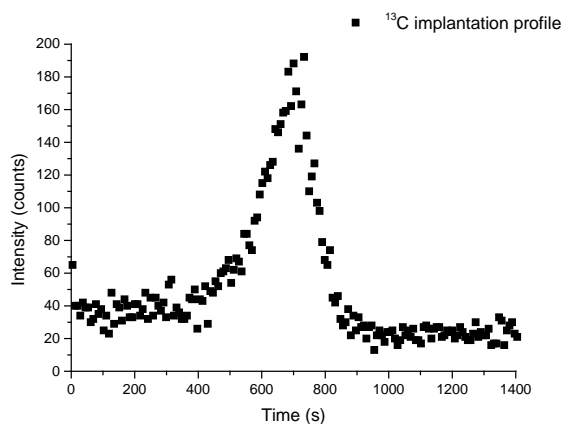
Figure 7: *Sputter profile of a* ^{13}C *as implanted HOPG*

The intensity (counts) is converted into ^{13}C at.% knowing that the natural 13C abundance is of 1.07 at.% and corresponds to the baseline (used as internal standard). Thus we obtain,

$$C(p) = (I(p) \times 1,07) \times I_{LB}$$

where C(p) is the ^{13}C at depth p, I(p) the ^{13}C intensity at depth p and I_{LB} the ^{13}C intensity at the baseline.

The same kind of procedure was followed for ^{37}Cl monitoring. The detected secondary ions were ^{37}Cl (mostly implanted ions), ^{35}Cl (initial impurity) and ^{12}C (matrix ions). The mass resolution M/DM was set to 7000 to avoid a major polyatomic interference due to ^{12}C^{1}H. The ^{12}C signal was used as an internal reference to normalize the ^{37}Cl signal. ^{37}Cl contribution due to pristine chlorine present as an initial impurity was estimated from ^{35}Cl signal and subtracted from the total ^{37}Cl signal (pristine+implanted) to obtain the actual ^{37}Cl implanted concentration. Finally following parameters are obtained for ^{13}C and ^{37}Cl resumed in table 3:

***Tableau 3 :*** *^{13}C et du ^{37}Cl implantation parameters in HOPG*

	Energy (keV)	→	Depth (nm)	Fluence (at.cm^{-2})	→	Concentration
^{13}C	150		300	6 x 10^{16}		4 à 5at. %
^{37}Cl	250		220	5 x 10^{13}		50 ppm

2.2 Raman microspectrometry

Raman spectrometry analyses were carried out using a Renishaw INVIA Reflex spectrometers equipped with an Ar lasersource (514.5 nm wavelength, i.e., 2.41 eV), focused through a Leica

microscope. The Rayleigh scattering component was removed by an Edge filter, and the Raman scattered light was dispersed by a holographic grating with 1800 lines/mm and detected by a CCD camera. The spectra were collected under microscope (x50 objective). A very low incident power (<1 mW) was used to avoid heating effect and possible subsequent structural modifications. The experiments were carried out at ENS, Paris, France in collaboration with J.N. Rouzaud and D. Deldicque , or at CEMHTI, Orléans, France in collaboration with M.R. Ammar, P. Simon and A. Canizares.
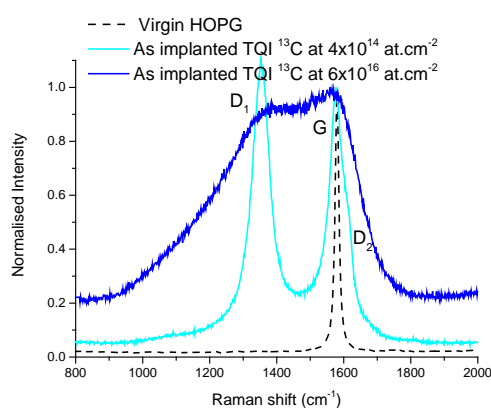
Figure 8 : *Raman spectra of the as HOPG samples implanted with ^{13}C respectively at $4x10^{14}$ at.c$^-$m^2 and $6x10^{16}$ at.cm^{-2} compared to the virgin HOPG*

Figure 8 represents the Raman spectra of the as HOPG samples implanted with ^{13}C respectively at $4x10^{14}$ at.c$^-$m^2 (disorder evaluated to about 7.4 dpa) and $6x10^{16}$ at.cm^{-2} compared to the virgin HOPG (disorder : << 0.1 dpa). Compared to the virgin HOPG characterized by a unique band centered at around 1580 cm^{-1} corresponding to the ''graphite'' band, all other spectra, normalized to the G band (Raman shift around 1581 cm^{-1}) of the virgin sample, display additional bands called D for ''Defect'' bands. They are known to be characteristic of disordered graphite and change in intensity relative to the G band with increasing degree of disorder of the graphitic structure [Beny-Basset 1985, Rouzaud 1983]. The G band corresponds to one-phonon Raman scattering process at the 1st Brillouin zone center and consists of the collective in-plane bond stretching of the polyaromatic carbon atoms (E_{2g} symmetry). The D_1 band, located at 1350 cm^{-1}, corresponds to the breathing of the polyaromatic carbon atoms (A_{1g} symmetry). The D_2 band, located at $\approx$ 1625 cm^{-1}, which appears as a shoulder on the G band is assigned to phonons near the Brillouin zone center. The activation process of these defect-induced bands involves peculiar electron-phonon interaction mediated by defects [Pimenta 2007, Tuinstra 1970]. It can be noticed that the implantation process results in a strong increase of the defect bands reflecting a strong disordering of the graphite structure tending to amorphization because ion beam irradiation leads to a significant breaking of aromatic cycles, especially for the high implantation fluence with the occurrence of chain sp^2 carbons and sp^3 hybridized carbons. Thus, the G band becomes an average measure of the sp^2 C-C carbons in both aromatic cycles and chains and shifts continuously down to ~1530 cm^{-1} [Ammar 2015]. The disordering results also in an increase of

the G band FWHM reaching values around 200 cm^{-1} for the as implanted sample at 6×10^{16} at.cm^{-2} whereas the FWHM of G band value of the virgin HOPG is around 15cm^{-1}.

## 2.3 High Resolution Transmission Electron Microscopy (HRTEM)

2.3.1 Processing

Ultrathin sections were prepared using Focused Ion Beam (FIB) technique which was shown to be an especially relevant method to prepare implanted graphite samples [Ammar 2010 b]. The thin sections were cut perpendicularly to the sample surface. The preparation method, which is well described in [Wirth 2009], was performed with a FEI Strata DB 235 dual beam FIB at the Institut d'Electronique, de Microélectronique et de Nanotechnologie (IEMN, Université Lille 1, France). A thin layer of platinum was deposited on the samples beforehand, aiming to protect the HOPG surfaces from Ga+ ion implantation during the milling process. The HOPG thin sections were afterwards transferred to TEM lacey grids.

Then, the HRTEM experiments were carried out by D. Deldicque and J.N. Rouzaud from ENS Paris with the help of Patricia Beaunier from the Laboratoire de Réactivité de Surface (UPMC, Paris 6) using a JEOL JEM 2011 facility with an operating voltage of 200 kV at the ''Laboratoire de Réactivité de Surface'' of the Université Pierre et Marie Curie (UPMC – Paris 6), France. The microscope resolution is of 1.8 Å.

The HRTEM images processing was then made in two steps according to a method proposed by Rouzaud and Galvez [Rouzaud 2002,Galvez 2002] and the processing is well described in [Le Guillou 2015].

The first step of the process aimed at obtaining homogeneous images without background noise. Thus, 1024 x1024 pixels areas were first cut in each image and then skeletonized using the Visilog 5.1 software through the stages based on the use of the Fourier transform (FT) allowing image filtration as illustrated in Fig. 9.
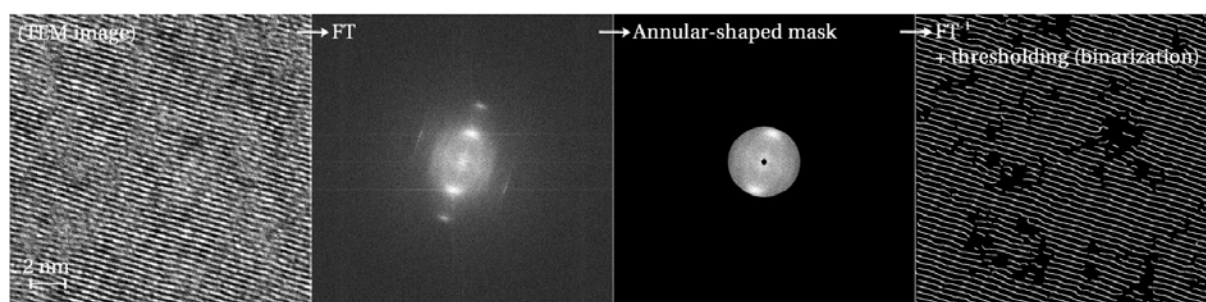

Figure 9 : *Skeletonized image of a 1024 x1024 pixels area taken from a TEM image obtained on an as-implanted HOPG thin section at a magnification of 400,000.*

A bandpass filtering of the raw TEM input image (annular-shaped mask) in the Fourier space allows eliminating background noise. Then, the inverse Fourier transform (FT1) gives a noise free image, retaining only contrasted fringes corresponding to the profile of graphene layers. The so-obtained grey scale image is processed by setting grey level thresholds, and a binary image is then

obtained thanks to a top-hat mathematical operation. This resulting image is finally skeletonized (i.e. each fringe is then 1 pixel wide).

In a second step, we used a computerized interface (AnalysePlan homemade programme) based on the statistical analysis of the skeleton segments in order to get structural and nanostructural data from the skeletonized images. This processing, schematized in Fig. 10, allows defining coherent domains (called BSUs for ''Basic Structural Units'' in the following) made of more or less large stacks of layers (dotted grey rectangles).
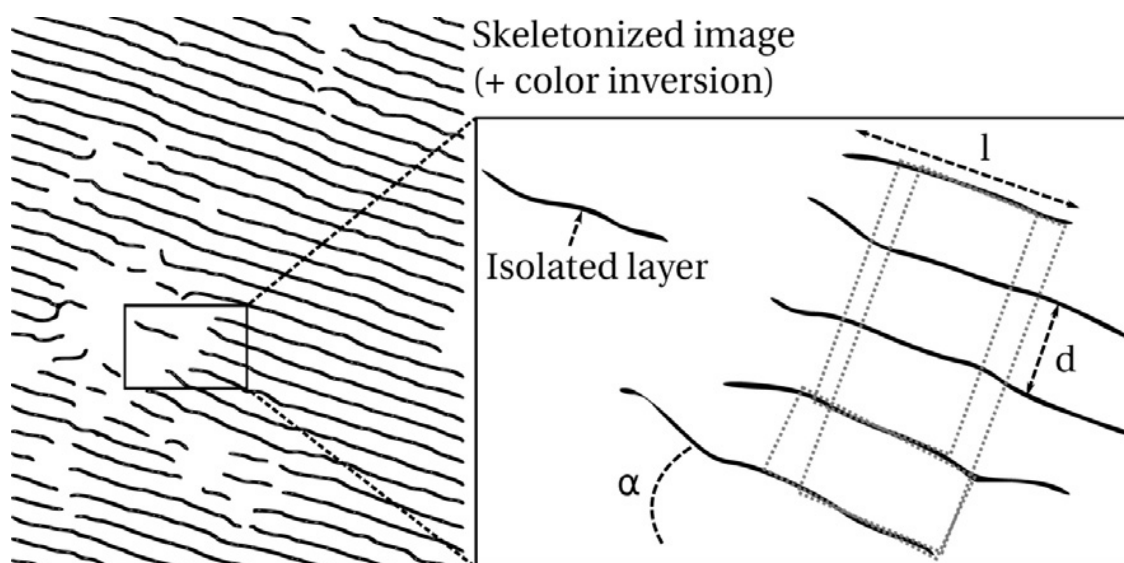
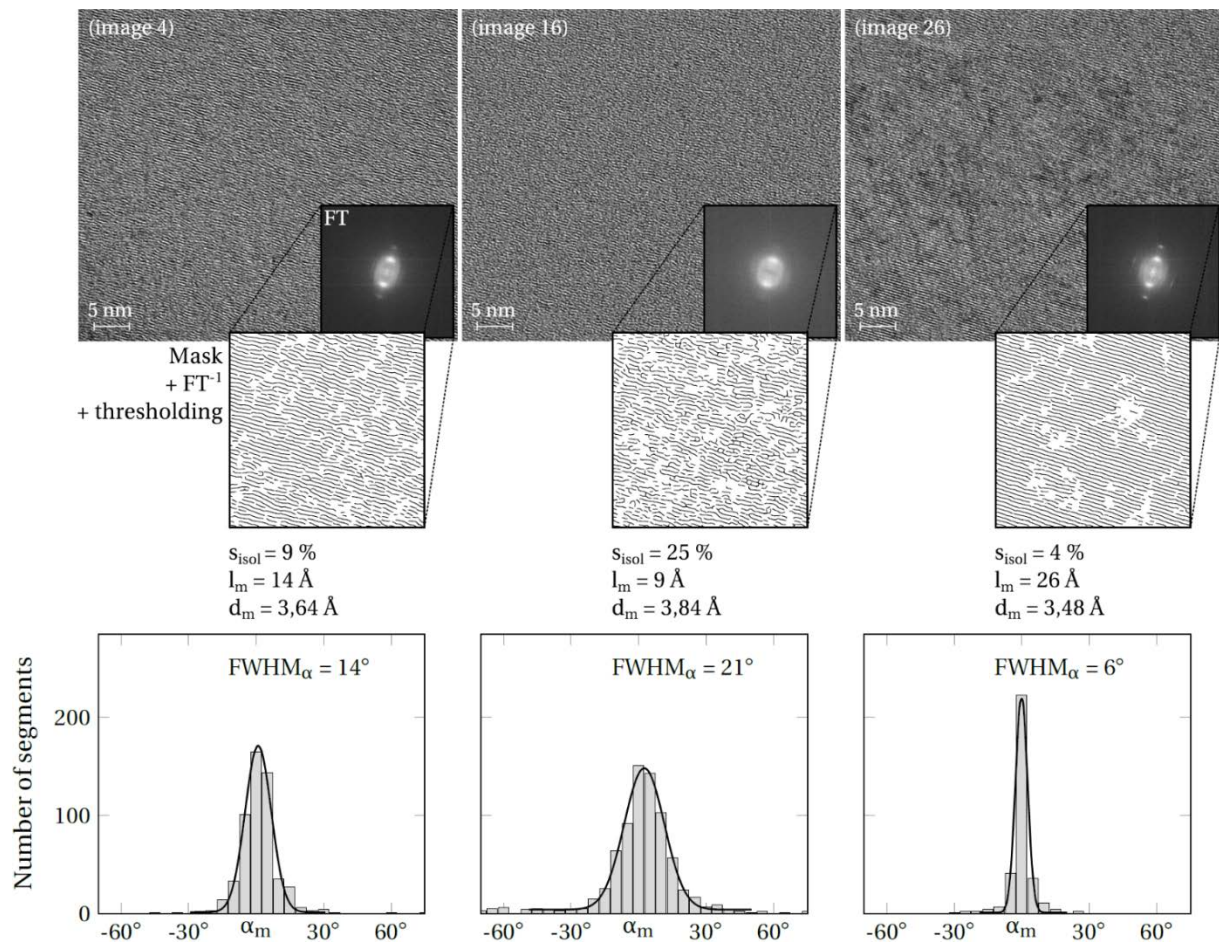**Figure 10:** *Scheme of the quantitative processing performed on the skeletonized frames with AnalysePlan programme*

The length of each individual fringe was measured and an average fringe length l_m, corresponding to a mean aromatic layer size, was obtained. The amount of single fringes s_{isol} (i.e. single layers) was also determined. To specify the presence of BSUs (i.e. stacked layers), sets of parallel layers were defined according to adjustable parameters such as a, the tolerance angle disorientation (here chosen as ±15°), and the maximum interfringe spacing d (here chosen as 0.6 nm). However, some layers do not form stacks. When an as defined BSU was detected, its interfringe spacing, height and length were measured. Then, the corresponding mean data were calculated for all the BSUs. As far as the nanostructure is concerned, the angle of each individual fringe was determined versus an orientation arbitrarily chosen as reference, and histograms of graphene layers relative orientations could be built. Finally, the following parameters have been assessed:

(i) s_{isol}, the average amount of isolated fringes (these layers are considered as non-stacked – d > 0.6 nm and/or a > 15° – and thus do not belong to any BSU),

(ii) l_m, the mean layer length,

(iii) FWHMa, the angular dispersion of the layers around a mean value α_m,

CAST
Report on ^{13}C behaviour under ion irradiation in HOPG
(model graphite) (D5.18)
EURATOM

(iv) d_m, the average interlayer distance within the BSU.

Thus, these parameters allow describing the structural and nanostructural states of the HOPG in the analyzed areas, thereby allowing estimating values for a lower range of the BSU's sizes. As a matter of fact, these values might be somehow underestimated with respect to the actual ones due to projective effects as shown by Da Costa et al. [Da Costa 2015].

As an illustration, an example of an image processing is given in Figure 11.


Figure 11: *Quantitative processing of 1024×1024 pixels areas extracted from TEM images recorded on three different structural zones. αm refers to the mean value of the plane inclination on each skeletonized frame, FWHM$_\alpha$ to the plane angular dispersion, s$_{isol}$ to the isolated planes proportion, l$_m$ to the mean length of the planes, and d$_m$ to the average inter-layer distance.*

2.3.2 HRTEM charaterization of virgin and implanted HOPG samples

In the following, the angular dispersion of the graphene planes and the inter-layer distances were chosen to evaluate and compare the structural states of the virgin and implanted HOPG samples.

Virgin HOPG samples

Two different HOPG samples were analyzed. Figure 12 presents the values of the inter-layer distances and the angular distribution measures for both. The values of the inter-layer distance are for both higher at the surface than at depth. This is probably due to the fact that we had to remove the first layers in order to obtain an uniform surface. Moreover, the different values of the angular distributions measured for both samples reflect the fact that their structural state is slightly different. However, in both cases, the angular distribution is smaller than 12°.
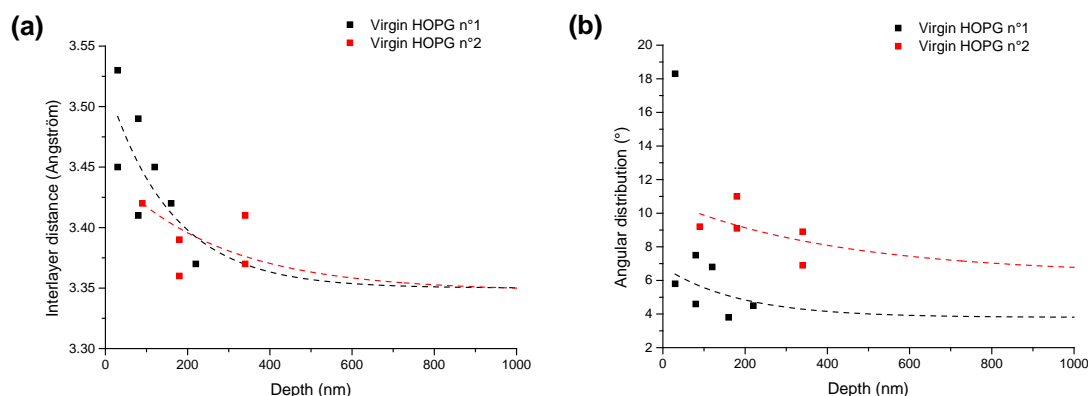
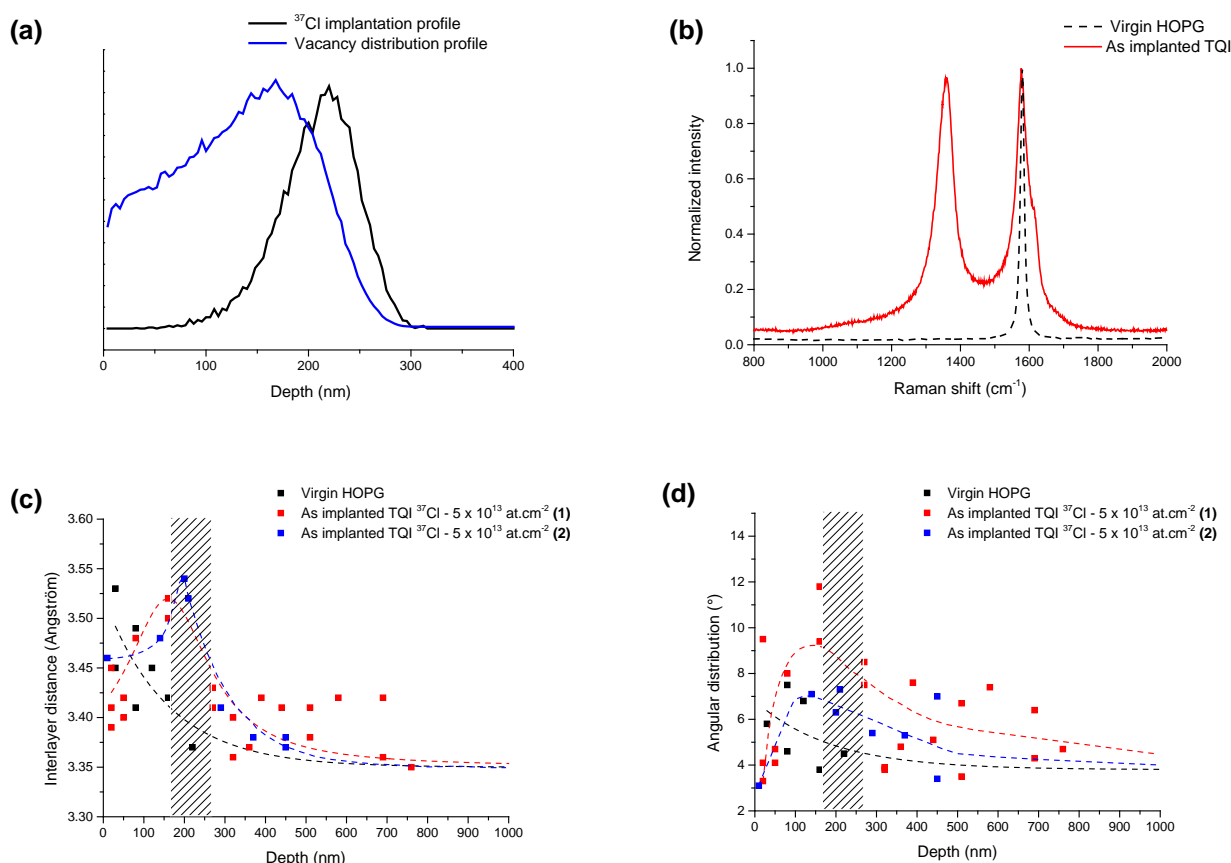*Figure 12: Inter-layer distance (a) and angular distribution (b) measured on virgin HOPG samples. The dotted lines allow guiding the eye.*

^{37}Cl implanted HOPG samples

Figure 13 represents the ^{37}Cl implantation profile and the vacancy distribution profile according to SRIM (a), the Raman spectra for the virgin HOPG sample and the ^{37}Cl as implanted HOPG sample (b), the inter-layer distance values for the virgin HOPG and two different ^{37}Cl as implanted HOPG samples (c), the angular distribution values for the virgin HOPG and two different ^{37}Cl as implanted HOPG (d).

Figure 13 a shows that the maximum ^{37}Cl concentration R_p is located at a depth of around 220 nm and that the maximum vacancy concentration R_d is located at shallower depth with a maximum at

around 170 nm. The Raman spectra of the as implanted sample on Figure 13 b display D_1 and D_2 defect bands. Figure 13 c and d show that the maximum destructuration coincides with the maximum vacancy concentration R_d.
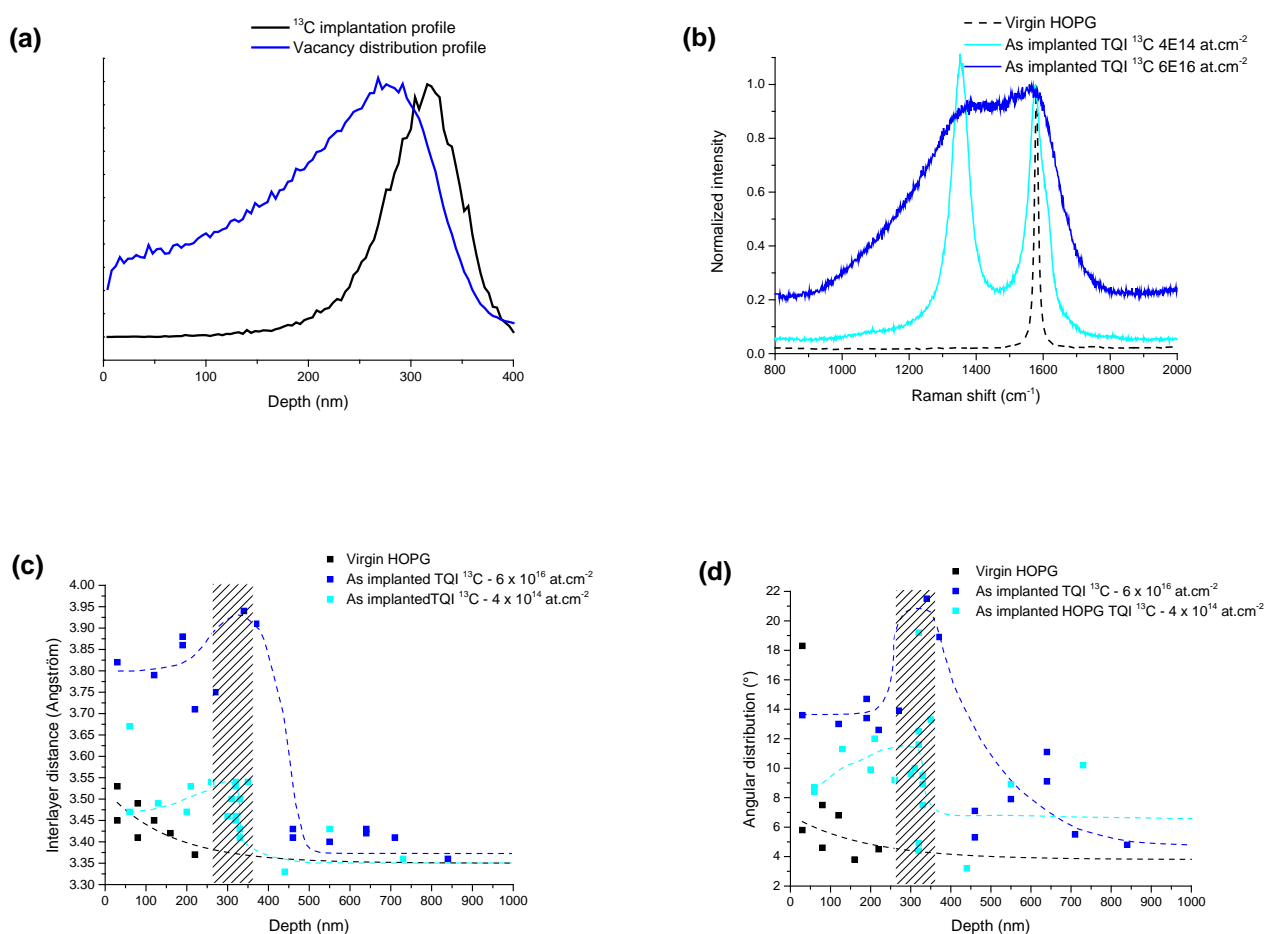

Figure 13: *Vacancy distribution profile and implantation profile for the ^{37}Cl as implanted TQI HOPG sample (a), Raman spectra for the virgin and the TQI samples (b), Inter-layer distance (c) and angular distribution (d) measured on virgin HOPG and TQI samples. The shaded zone covers the Rp value of the implanted and the dashed lines enable the trends in the evolution of these values as a function of depth to be seen more clearly.*

^{13}C implanted HOPG samples

Figure 14 represents the ^{13}C implantation profile and the vacancy distribution profile according to SRIM (a), the Raman spectra for the virgin HOPG sample and the ^{13}C as implanted HOPG sample (b), the inter-layer distance values for the virgin HOPG and the implanted HOPG samples at two different fluences 4 x 10^{14} at.cm^{-2} and 6 x 10^{16} at.cm^{-2} (c), the angular distribution values for the virgin HOPG and both implanted HOPG samples (d).

Figure 14 a shows that the maximum ^{13}C concentration R_p is located at a depth of around 300 nm and that the maximum vacancy concentration R_d is located at shallower depth with a maximum at around 275 nm. The Raman spectra of these as implanted sample on Figure 14 b show that the destructuration of the high fluence implanted sample is important (there is an overlapping of the defect and G bands) whereas on the low fluence implanted sample the defect and G bands are well seperated. Figure 13 c and d show that the maximum destructuration coincides with the maximum vacancy concentration R_d.

***Figure 14:** Vacancy distribution profile and implantation profile for the ^{13}C as implanted TQI HOPG sample (a), Raman spectra for the virgin and the TQI samples implanted at two fluences (b), Inter-layer distance (c) and angular distribution (d) measured on virgin HOPG and both TQI samples. The shaded zone covers the Rp value of the implanted and the dashed lines enable the trends in the evolution of these values as a function of depth to be seen more clearly.*

These HRTEM results show that for both implantations, the sample is disordered from the surface down to around 300 nm. Then, from this depth, the graphite structure is again well ordered because the values of the inter-layer distances are close to 3.35 Å and the value of the angular distribution is lower than 10°. The implantation effect is therefore clearly visible down to 300 nm. Moreover, it seems that the implantation fluence plays a major role. Indeed, the inter-layer distance measured on the high fluence implanted sample (6 x 10^{16} at.cm^{-2}) is far higher than that measured on the low fluence (4 x 10^{14} at.cm^{-2}) implanted one and reaches almost 4 Å at a depth of 340 nm. The value of the angular dispersion is also higher for the high fluence implanted sample compared to the low fluence implanted one. These results are supported by the Raman results, as quoted previously.